

## ABSTRACT

Title of Document: NOVEL INTERACTIONS OF LIQUID CRYSTALS WITH COATED NANOPARTICLES.

Jefferson W. Taylor, PhD, 2013

Directed By: Associate Professor, Luz J. Martínez-Miranda, Materials Science and Engineering

Functionalized nanoparticles have a wide range of applications in liquid crystal systems, including displays, photovoltaics, and drug delivery. We need to understand the interactions between the nanoparticles and the liquid crystal molecules in order to utilize them fully and safely. We investigate the short-range interaction of coated nanoparticles with a liquid crystal membrane or bulk sample through the use of atomic force microscopy (AFM) and X-ray scattering techniques. We identify the role the functionalization plays in the phase behavior of the liquid crystal both as a thin film and in bulk. Our research produced three results. We identify differing behavior in thin film samples of liquid crystal and coated nanoparticles dependent upon particle functionalization using AFM. Using X-ray scattering we measure the alignment and smectic layer formation in the presence of coated nanoparticles, even above the smectic-A to nematic transition temperature. We find evidence of a “halo” that forms around coated nanoparticles, particularly with longer coating molecules.

STUDY OF LIQUID CRYSTALS INTERACTING WITH COATED  
NANOPARTICLES.

By

Jefferson W. Taylor

Dissertation submitted to the Faculty of the Graduate School of the  
University of Maryland, College Park, in partial fulfillment  
of the requirements for the degree of  
Doctor of Philosophy  
2013

Advisory Committee:

Professor Luz J. Martínez-Miranda, Chair

Professor Robert M. Briber

Professor Sheryl H. Ehrman

Professor Lourdes G. Salamanca-Riba

Professor Mohamad Al-Sheikhly

© Copyright by  
Jefferson W. Taylor  
2013

## Acknowledgements

The author wishes to thank his graduate advisor, Professor Luz J. Martínez-Miranda of the University of Maryland, Dr. Lynn K. Kurihara of the Naval Research Laboratory for her collaboration, and the National Science Foundation for financial support.

# Table of Contents

Acknowledgements.....	ii
Table of Contents.....	iii
List of Figures.....	v
Chapter 1: Introduction.....	1
<u>Introduction to Liquid Crystals</u> .....	1
<u>Objective</u> .....	3
Chapter 2: Methodology.....	8
<u>Equipment</u> .....	8
AFM.....	8
Polarized optical microscopy.....	11
X-ray scattering.....	13
<u>Samples Used and Sample Preparation</u> .....	20
Chapter 3: Bilayer film studies with AFM.....	24
<u>Theory and background</u> .....	24
<u>Results</u> .....	31
MHDA.....	31
APTS.....	34
PEG.....	35
<u>Analysis</u> .....	38
Chapter 4: Bulk studies with X-ray scattering as a function of temperature.....	40
<u>Background</u> .....	40
<u>Results</u> .....	57
MHDA.....	57
PEG.....	78
<u>Comparing the MHDA and PEG data</u> .....	93
Chapter 5: Halo Phenomenon.....	100
<u>Observations</u> .....	100
Chapter 6: Relating AFM findings to X-ray findings.....	105
Chapter 7: Summary of Results.....	108

<u>AFM</u> .....	108
<u>Polarized Optical Microscopy</u> .....	108
<u>X-ray Scattering</u> .....	109
<u>Conclusion</u> .....	110
<u>Future Work</u> .....	111
 Bibliography .....	 114

## List of Figures

- i. Common liquid crystal phases.
- ii. 8CB molecule.
- iii. Phase transition temperatures of octylcyanobiphenyl (8CB).
- iv. POM micrograph of 8CB in the smectic phase.
- v. POM micrograph of 8CB in the nematic phase.
- vi. Schematic depicting top and side view of experimental setup. Detail shows bulk alignment to substrate with nanoparticle distortion.
- vii. X-ray scattering apparatus.
- viii. Sample stage with heating element and RTD.
- ix. APTS nanoparticle DLS experimental results on logarithmic scale.
- x. PEG nanoparticle DLS experimental results on logarithmic scale.
- xi. Chemical structures of functionalization compounds.
- xii. Interactions between lipid bilayer and a bare silica nanoparticle of varying size. (Roiter, et al.)
- xiii. AFM micrograph of MHDA-coated FeCo nanoparticles on glass substrate.
  
- xiv. Schematic depicting orientation of coating compounds on their respective nanoparticles.
- xv. Two 8CB molecules interdigitate to form a "rod" approximately 31.5 Å long with hydrophobic ends and a hydrophilic middle.
- xvi. Possible interactions between coated nanoparticle and an 8CB membrane. A) Nanoparticle covered by membrane. B) Nanoparticle coated with tangential molecules, disrupting membrane order. C) Nanoparticle forms hole in membrane.
- xvii. Liquid crystal deformations found in the smectic phase.
- xviii. AFM micrograph of an 8CB monolayer with dispersed MHDA-coated nanoparticles. Dark areas are bare substrate.
- xix. AFM micrograph of 8CB monolayer at edge of sample, displaying step edge phenomenon.
- xx. AFM micrograph of 8CB monolayer with dispersed MHDA-coated nanoparticles.
- xxi. AFM elevation data micrograph of MHDA-coated nanoparticles in an 8CB thin film. White circles show four nanoparticles present in this image.
  
- xxii. AFM phase data micrograph of MHDA-coated nanoparticles in an 8CB thin film. Red dotted circles show two exposed nanoparticles. Blue solid circles show two covered nanoparticles.
- xxiii. AFM elevation data micrograph of 8CB smectic layers. No nanoparticles distinguishable at this scale.
- xxiv. 3D micrograph constructed from AFM elevation data of APTS-coated nanoparticles in 8CB thin film.

- xxv. AFM micrograph of PEG-coated nanoparticles in an 8CB thin film.
- xxvi. PEG-coated nanoparticles covered by 8CB thin film
- xxvii. AFM micrograph elevation data of 8CB smectic layers with ZnO nanoparticles visible at edges of smectic layers.
- xxviii. AFM micrograph phase data that corresponds to elevation data in Figure 24. Material hardness change is visible at the edge of this smectic layer.
- xxix. Glass substrate has hydroxyl termination, which attracts the hydrophilic ends of interdigitated 8CB rods.
- xxx. Polarized optical micrograph of 8CB and APTS-coated nanoparticle mixture.
  
- xxxi. Raw data from X-ray scattering experiment at room temperature with a 30% MHDA nanoparticle sample.
- xxxii. Raw data from Figure 27 after background data is removed.
- xxxiii. Gaussian curve from the direct beam shown in red.
- xxxiv. Direct beam data removed; three Gaussian curves fit to remaining data.
- xxxv. Two 8CB molecules interdigitate to form a “rod” approximately 31.5 Å long with hydrophilic ends and hydrophobic middle.
- xxxvi. Geometry of calculating the tilt of molecules in smectic layers.
- xxxvii. Schematic depicting the different repetitive geometries that produce peaks in X-ray scattering data.
- xxxviii. Gaussian curves fit to data from annealed sample (background data removed).
- xxxix. Annealed sample raised to 30.17°C ( $\pm 0.056^\circ\text{C}$ ), still in smectic-A phase.
- xl. Annealed sample raised to 30.28°C ( $\pm 0.056^\circ\text{C}$ ), which is still in the smectic-A phase.
- xli. Annealed sample at 30.39°C ( $\pm 0.056^\circ\text{C}$ ), the SmA-N transition temperature.
  
- xl.ii. Annealed sample at 30.61°C ( $\pm 0.056^\circ\text{C}$ ) in the nematic phase.
- xl.iii. Rhombicuboctahedron faceted nanoparticle.
- xl.iv. Cubic faces in red, edge faces in blue, corner faces in green.
- xl.v. PEG-coated nanoparticle with 8CB rods forming "grains" aligned to facets. Lower energy edge grains highlighted. Horizontal cubic face grains preferentially disorder to lower the energy of the system.
- xl.vi. Temperature 26.67° C  $\pm 0.056^\circ\text{C}$ , smectic phase.
- xl.vii. Temperature 30.00° C  $\pm 0.056^\circ\text{C}$ , smectic phase.
- xl.viii. Temperature 30.33° C  $\pm 0.056^\circ\text{C}$ , Sm-N transition.
- il. Temperature 30.67° C  $\pm 0.056^\circ\text{C}$ , nematic phase.
- l. Temperature 31.44° C  $\pm 0.056^\circ\text{C}$ , nematic phase.
- li. Position of low q peak (Peak 1); Temperature  $\pm 0.056^\circ\text{C}$ .
- lii. Position of low q peak (Peak 2); Temperature  $\pm 0.056^\circ\text{C}$ .
- liii. Position of mid q peak (Peak 3); Temperature  $\pm 0.056^\circ\text{C}$ .
- liv. Position of high q peak (Peak 4); Temperature  $\pm 0.056^\circ\text{C}$ .
- lv. Summary of peak positions; Temperature  $\pm 0.056^\circ\text{C}$ .

- lvi. Correlation length of low q peak (Peak 1); Temperature  $\pm 0.056^{\circ}\text{C}$ .
- lvii. Correlation length of low q peak (Peak 2); Temperature  $\pm 0.056^{\circ}\text{C}$ .
- lviii. Correlation length of mid q peak (Peak 3); Temperature  $\pm 0.056^{\circ}\text{C}$ .
- lix. Correlation length of high q peak (Peak 4); Temperature  $\pm 0.056^{\circ}\text{C}$ .
- lx. Summary of correlation lengths; Temperature  $\pm 0.056^{\circ}\text{C}$ .
- lxi. Temperature  $26.67^{\circ}\text{C} \pm 0.056^{\circ}\text{C}$ ; smectic phase.
- lxii. Temperature  $30.56^{\circ}\text{C} \pm 0.056^{\circ}\text{C}$ ; smectic phase.
- lxiii. Temperature  $30.89^{\circ}\text{C} \pm 0.056^{\circ}\text{C}$ ; Sm-N transition.
- lxiv. Temperature  $31.11^{\circ}\text{C} \pm 0.056^{\circ}\text{C}$ , nematic phase.
- lxv. Temperature  $31.67^{\circ}\text{C} \pm 0.056^{\circ}\text{C}$ , nematic phase.
- lxvi. Position of low q peak; Temperature  $\pm 0.056^{\circ}\text{C}$ .
- lxvii. Position of mid q peak; Temperature  $\pm 0.056^{\circ}\text{C}$ .
- lxviii. Position of high q peak; Temperature  $\pm 0.056^{\circ}\text{C}$ .
- lxix. Summary of peak positions; Temperature  $\pm 0.056^{\circ}\text{C}$ .
- lxx. Correlation length of low q peak; Temperature  $\pm 0.056^{\circ}\text{C}$ .
- lxxi. Correlation length of mid q peak; Temperature  $\pm 0.056^{\circ}\text{C}$ .
- lxxii. Correlation length of high q peak; Temperature  $\pm 0.056^{\circ}\text{C}$ .
- lxxiii. Summary of correlation lengths; Temperature  $\pm 0.056^{\circ}\text{C}$ .
- lxxiv. Low q peak position comparison; Temperature  $\pm 0.056^{\circ}\text{C}$ .
- lxxv. Mid q peak position comparison; Temperature  $\pm 0.056^{\circ}\text{C}$ .
- lxxvi. High q peak position comparison; Temperature  $\pm 0.056^{\circ}\text{C}$ .
- lxxvii. Low q peak correlation length comparison; Temperature  $\pm 0.056^{\circ}\text{C}$ .
- lxxviii. Mid q peak correlation length comparison; Temperature  $\pm 0.056^{\circ}\text{C}$ .
- lxxix. High q peak correlation length comparison; Temperature  $\pm 0.056^{\circ}\text{C}$ .
- lxxx. PEG-coated nanoparticle displaying halo. 8CB covering the PEG halo causes the wavy noise seen here.
- lxxxi. AFM micrograph of PEG-coated nanoparticles on glass. Right image outlines boundary of a “halo” with radius of 110-135 nanometers.
- lxxxii. a) (Left) Side view of PEG-coated nanoparticle on glass substrate with 8CB monolayer covering PEG. b) (Right) Side view of PEG-coated nanoparticle in bulk 8CB. 8CB molecules form smectic layers near particle, but form disordered zones where the 8CB molecules would meet the bulk at 90 degree angles.
- lxxxiii. (Left) Side view of a nanoparticle in 8CB with an incident X-ray (red) whose trajectory is in-plane with the smectic layers of the bulk. (Right) Top view of nanoparticles with X-ray beam diffracting off smectic layers (blue).

# Chapter 1: Introduction

## Introduction to Liquid Crystals

Liquid crystals are an intermediate phase of matter, whose molecules exhibit more order than those found in the liquid phase, but less order than those of a crystalline phase.[2] Liquid crystalline materials exhibit anisotropic

properties that are frequently exploited in applications, such as photovoltaics [3] and displays[4-6]. Liquid crystal phases take many forms, which transform from one to another either

through change in temperature (thermotropic) or in concentration (lyotropic).[2] These occur due to several

different factors, mainly molecular shape, charge, and hydrophobicity/philocity.[2] The most common phases (see

Figure 1) are the nematic, identified by alignment of the long-axis of rod-shaped molecules (also known as the “director”), the smectic (of which the smectic-A is shown), with molecules

organized into layers, and the columnar, with disc or ring-shaped molecules stacking like coins.[2] More complex arrangements also occur with more exotic molecules,[7]

but are not seen in this study.

The molecule used in this study, octylcyanobiphenyl (hereafter referred to as 8CB) shown

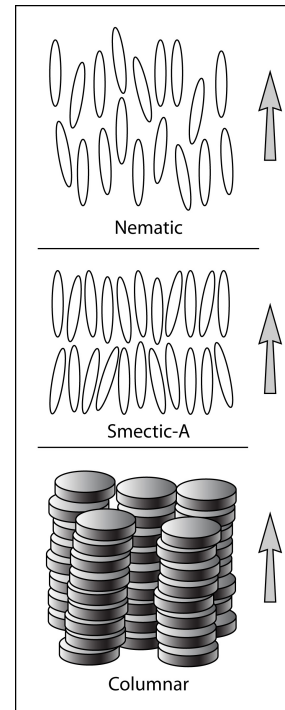


Figure 1: Common liquid crystal phases

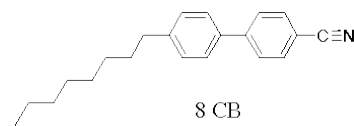


Figure 2: 8CB molecule

in Figure 2, is a calamitic (rod-shaped), thermotropic liquid crystal that exhibits the following phase transitions at different temperatures, shown in Figure 3 [8, 9].

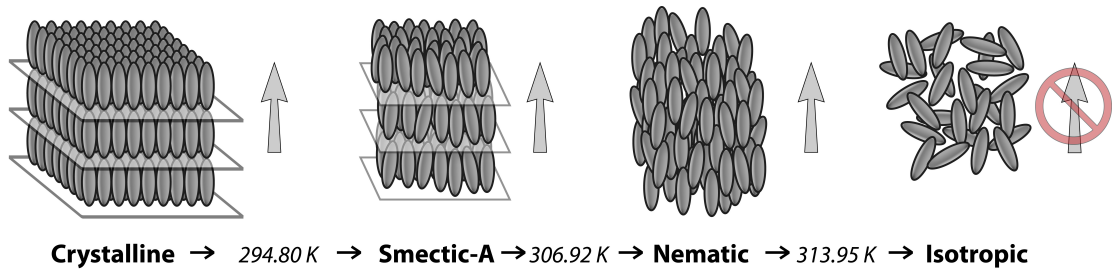


Figure 3: Phase transition temperatures of octylcyanobiphenyl (8CB).

This particular compound is a model system and has been very well studied. It also exhibits its phases near room temperature, which is advantageous for our experiments.

Liquid crystal systems display anisotropic properties due to the spontaneous alignment of their molecules. Elastic, electric, magnetic, and optical properties are all affected by liquid crystal anisotropy, and can therefore be manipulated by changing the liquid crystal phase or the molecular alignment.[2, 10] When combined with nanoparticles into a nanocomposite, these properties can frequently be more easily controlled.[5, 11-14]

Researchers have investigated preparation of substrates for the development of liquid crystal displays using surfactants for many years.[15] Liquid crystal alignment is heavily influenced by surface interactions, and surface treatments dictate those interactions. These treatments can impose electrostatic attraction or repulsion with the liquid crystal molecules. More simply, topographical changes can influence their alignment. A substrate that has been rubbed, creating microscopic grooves in the surface, will align the liquid crystal molecules in the direction of the rubbing.[16-19] In other words, the molecules will lay down parallel to the grooves when they might

otherwise orient normal to the surface. More recently, similar studies have been done for the development of nanotemplates [20-22] and organic solar cells.[23-26]

Alignment of liquid crystal molecules is also influenced by their interface with nanostructured materials. We proposed a study of liquid crystal alignment using nanoparticles with modified surface properties to show that the alignment can be manipulated or controlled by changing those interfacial properties.

### Objective

We propose to investigate the short-range interaction of coated nanoparticles with a liquid crystal membrane or bulk sample, based on what was said above, using AFM and X-ray scattering. This will give us information on the order or lack of it and how this can be used in applications. The interaction can help determine how the electrical, magnetic, or mechanical signals will propagate through the nanocomposite. Our research investigates the effect on the ordering of a liquid crystal thin film in close proximity to a magnetic nanoparticle that has been coated with a functionalization compound. These compounds, and their use with nanoparticles in liquid crystal systems, are of interest to industry for their ability to influence phase transition temperatures and alignment of liquid crystal molecules.[8] This research also has biological implications, as most biological membranes have liquid crystal phases.[27, 28] With the use of nanoparticles in consumer products growing in popularity[29], it is essential to fully understand their molecular interactions in order to utilize them in a safe and responsible manner.

Research of these hybrid systems will be valuable to those interested in using them for applications.[14] Previous studies have found that functionalization compounds can induce significant changes in the liquid crystal properties.[30, 31] They can shift the smectic-nematic transition temperature of the system by several degrees Centigrade and makes this transition closer to first-order.[8, 32-34] Depending on the application, the resulting hysteresis could be beneficial or a liability. In biological systems, the change in transition temperature could be very problematic for temperature-sensitive reactions.

Our bulk studies have shown that functionalized nanoparticles affect liquid crystal behavior in bulk,[8, 12] and in this study we used AFM to investigate if this is true for thin films as well. Due to the sizable influence of surface interaction on liquid crystal orientation[16, 35], the effect is detectable, but dependent on the functionalization compound in question. This study focuses on bi-molecular liquid crystal thin films because they are analogous structurally and behaviorally to the biological membranes found in cell walls throughout nature.[2, 27, 36] Using a thin-film substitute for these biological applications is common practice in research, and our previous focus on liquid crystal systems, which exhibit the same phases as biological cell membranes, makes them a suitable model system for work with the interaction of nanoparticles and these membranes.

Previous research by our group and others have found coated nanoparticles in a liquid crystal composite system will cause a shift in the transition temperatures of the liquid crystal phases.[8, 9] This shift is not universal. It is dependent on the orientation of liquid crystals in the vicinity of

the nanoparticles, which is heavily influenced by the nanoparticle functionalization. We will show evidence that this influence can result in “hole” formation in liquid crystal membranes, having safety and health implications when present in living systems.

Functionalized nanoparticles have become a very promising research area for many applications in both biology and industry. A nanoparticle’s functional coating is what enables cell receptor ligands to identify and accept them for drug delivery systems.[27, 37-39] Interaction with various proteins relies both on these compounds and the size of the nanoparticle being used.[28] Our previous research has shown that liquid crystal nanoparticle hybrid systems can improve the response to electric or magnetic stimulus, which is of interest in developing organic displays and in photovoltaic applications.[40, 41]

Nanoparticles are easily inhaled, ingested, or absorbed through the dermis,[11] and studies have shown that nano-scale structures, such as carbon nanotubes, have similar effects on the lungs as asbestos.[12, 42, 43] The concern with nanoparticles in particular is that disrupting biological membrane structure (via the mechanism investigated in this study) could have cytotoxic effects.[44, 45] Further research will be needed to fully validate these concerns, but the results of this study do support the hypothesis that nanoparticles interfere with molecular order in membranes.

We compare the results of this research to similar work done with phospholipids in close contact with uncovered silica nanoparticles,[1, 36] as well as bulk studies done with the same materials that are used here.[12] The results of this research show that the behavior of liquid crystals in contact with the

nanoparticles is dependent on the properties of the compound coating the particles.

We perform X-ray scattering experiments over a range of temperatures to track how the molecules rearrange in the presence of nanoparticles as the sample transitions from the smectic-A phase to the nematic phase. We can then compare the molecular structure of mixtures of liquid crystal with nanoparticles coated with different compounds to assess the impact of the functionalization compound on this interaction.

The behavior of a liquid crystal film can be described by the following energy formula[40]:

$$E = E_{\text{mech}} + E_{\text{magnetic}} + E_{\text{surface interaction}} + E_{\text{relative size}} \quad (1)$$

The film experiences a competition between the mechanical energy,  $E_{\text{mech}}$ , deforming the liquid crystal structure, and the surface interaction energy and relative size energy holding it together.  $E_{\text{surface interaction}}$  contains the parameter  $\varphi$ , [40, 46] which is the angle the liquid crystal molecule makes with the particle surface that we calculate from our X-ray scattering data. The X-ray experiments also give us information about the correlation length of the organized liquid crystal molecules and the faceting of the particles, which will be discussed later.  $E_{\text{relative size}}$  accounts for the fact that nanoparticles close to the size of the liquid crystal molecule will more heavily influence the liquid crystal ordering than ones that are significantly larger or smaller than the liquid crystals. We verify nanoparticle size and confirm membrane behavior using AFM.

We observe and discuss a formation we call the “halo phenomenon” during our AFM experiments. It was first seen in AFM scans of PEG-coated nanoparticles on glass

slides, and was also visible in mixtures containing 8CB liquid crystal as well. The behavior of the liquid crystal in the presence of these halos is rather interesting and will be investigated further. This formation gives us clues as to the behavior of PEG-coated nanoparticles in bulk 8CB as well.

This thesis is organized thus: Chapter 2 summarizes the different techniques used to characterize the nanocomposites; Chapter 3 presents the results of an AFM study on bilayers of liquid crystals in contact with the nanoparticles; Chapter 4 presents and analyzes the results of X-ray scattering studies on liquid crystals mixed with MHDA or with PEG terminated nanoparticles; Chapter 5 presents an AFM study of the halo structure observed mainly on the PEG terminated nanoparticles; Chapter 6 compares the results obtained with AFM and X-ray scattering; Chapter 7 summarizes the results and proposes some future work.

## Chapter 2: Methodology

### Equipment

We have utilized several characterization techniques, such as atomic force microscopy (AFM), polarized optical microscopy, medium angle X-ray scattering (XRS), and light scattering to conduct this research. A brief description of each method follows.

### AFM

AFM gives us a nanoscale view of the sample's surface in the form of elevation and phase data. The microscope works by vibrating a silicon cantilever at approximately 300 kHz (varies dependent on the natural frequency of that particular cantilever). At the end of this cantilever is a pyramidal needle oriented perpendicularly to the length of the cantilever. By vibrating this needle in close proximity to the surface of the sample (called "tapping mode"), the AFM is able to detect the changes in the phase and amplitude of the needle's oscillation, caused by Van der Waals attraction or other intermolecular forces from the sample surface.[47] The cantilever is only micrometers long, with the tip of the needle on the order of tens of nanometers wide. To monitor the cantilever's oscillation, a laser is reflected off its upper surface. Over a distance of a few centimeters, the reflected laser light oscillates enough to be easily measured by a CCD detector.[48] The needle is scanned across the sample area in the X and Y directions while Z, the elevation data, is recorded for each coordinate. When done correctly, the needle, which

is very fragile, never comes into contact with the sample. The phase of the cantilever oscillation will change in different ways depending on the sample's physical characteristics, like friction, adhesion, and viscoelasticity, so two areas of the scan that resulted in different phase data have unique composition.[49] With this information we can measure the diameter of a nanoparticle, thickness of the film or smectic layers, surface roughness, and detect changes in material.[47] In some cases it is possible to “see” whether a particle is covered by the liquid crystal film or if it has deformed the membrane.[50] AFM resolution is limited largely by the sharpness of the tip being used. We use silicon short-cantilever tips with a natural frequency of about 300 kHz, which give us sufficient resolution to distinguish protrusions above the liquid crystal film (caused by a nanoparticle whose diameter is larger than the length of the 8CB molecule), but not detect particles of the same size as or smaller than the thickness of the film. Roiter, et al. addressed this issue by attaching markers to these small particles, in situ, in the form of large insulin molecules.[1] The insulin was then detectable by the AFM tip, as it protruded from the surface of the phospholipid membrane. Unfortunately, our AFM is not capable of the same location repeatable scanning necessary for this technique. In addition, a main focus of this study is the influence the functionalization compounds have on the behavior of the film, which could be altered by the presence of insulin or other marker molecules. Therefore our data is confined to particles larger than 2.5 nm, the length of an 8CB molecule.

AFM tells us many useful things; however, this technique has drawbacks. A properly configured AFM can give very detailed information, but finding the appropriate configuration is often a matter of trial and error. The AFM used is a piece of equipment owned and maintained by the University of Maryland Nanocenter, but the fragile tips are

to be provided by the users. Tips can be customized for a variety of different applications, including magnetic tips, which detect magnetic fields in the sample (MFM). Individual requirements will vary based on technique and samples being studied.

The users must install their own AFM tip every time the microscope is used. The tip itself is a silicon chip approximately 2mm by 6mm with the cantilever protruding parallel to the long axis. It is moved with tweezers from the protective carrying case to the tip holder (a precarious task), where it is secured with a small clip. This process is where most AFM tips are damaged beyond repair, as it is quite easy to lose hold of the tip, and even a very small impact will cause the cantilever to break. The tip holder can then be mounted on the scanning head, which detaches from the base unit to facilitate tip installation. When the tip is installed, the laser must be aligned on the end of the cantilever, where the deflection will be greatest, resulting in the greatest sensitivity. This is done manually, using a series of alignment knobs, a computer readout giving the intensity of the reflected beam, and visual inspection of the laser light that is scattered by the micro-scale cantilever. This process takes quite a bit of practice to perfect, and doing it incorrectly will affect the quality of the scans produced.

One of the biggest drawbacks to using AFM is the active time commitment involved in getting clear, useful scans. Partly as a result of the installation and alignment procedure, a multitude of software parameters must be configured and tweaked for each session, sample, and even each scanned area. Since AFM is effectively a mechanical operation on the order of nanometers or micrometers, the process is very sensitive to vibration. Our AFM is vibration-isolated on an air table, but will still be affected by large disturbances or even loud noises.

Using AFM, we found evidence of both exposed and covered nanoparticles in 8CB thin film samples for each of our functionalization compounds. We studied films made using concentrations varying from 14% to 38% nanoparticles by weight. We expect to identify the size range at which a nanoparticle will be exposed, rather than covered by 8CB.

The computer records both the elevation of the scanned area and the change in phase of the vibrating needle. The phase is affected by the resistance imparted back on the needle by the sample surface; in other words, the sample hardness.[49] Soft materials do not alter the phase much at all, but hard materials can change the phase significantly. Therefore a change in composition from one area to another is visible as a dark area on a light background or vice versa.

Using the elevation data to locate particles having a larger diameter than the thickness of the liquid crystal film surrounding them, the corresponding phase data will reveal whether the jump in elevation was caused by a hard, bare particle, or a particle covered in a soft liquid crystal film. Examples are found in the AFM Results section.

### Polarized optical microscopy

Polarized optical microscopy (POM) allows us to quickly identify the phase of a liquid crystal system by visual cues alone. Combined with a temperature-controlled sample holder, we are able to find the approximate transition temperature of liquid crystal samples, limited by the ability of the temperature controller to hold the stage at a constant temperature. In practice, this variability is roughly  $\pm 0.056^\circ\text{C}$ . Cordoyiannis, et al. previously studied the dependence of nanoparticle concentration on the shift in transition temperature, using high-resolution adiabatic scanning calorimetry to calculate

the heat capacity of the sample.[8] The latent heat during the phase transition, though much smaller than would be measured in a more common solid-liquid phase transition, is easily detected and the transition temperatures accurately identified. We used this POM technique to ensure that our samples behaved in accordance to the findings of Cordoyiannis, et al. Identifying the transition temperature for each concentration ensured that we performed the X-ray studies in the correct temperature range.

The Polarized Optical Microscope allows us to examine films on a substantially larger scale than AFM, while still gathering data about the phases of our samples. Figure 4 shows an 8CB film in the smectic phase, with characteristic quadrupole disclinations.[51]

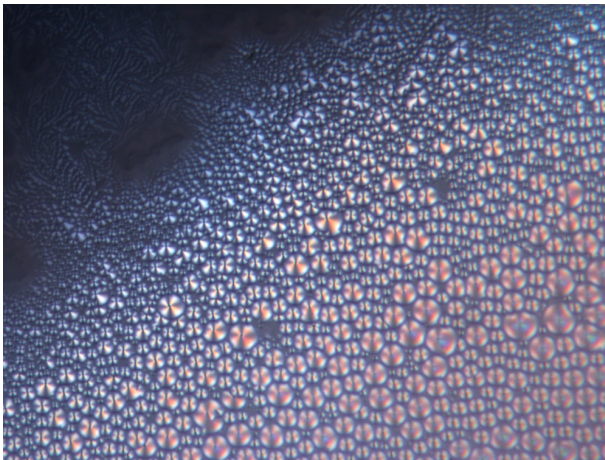


Figure 4: POM micrograph of 8CB in the smectic phase.

The circular disclinations get smaller where the film becomes thinner at its edge. Using a temperature controller we are able to find both the smectic-nematic and the nematic-isotropic phase change temperatures. As the temperature is raised, the image in Figure 4 (taken at  $33.6^{\circ}\text{C} \pm 0.056^{\circ}\text{C}$ ) changes to that in Figure 5 (taken at  $34.0^{\circ}\text{C} \pm 0.056^{\circ}\text{C}$ ).

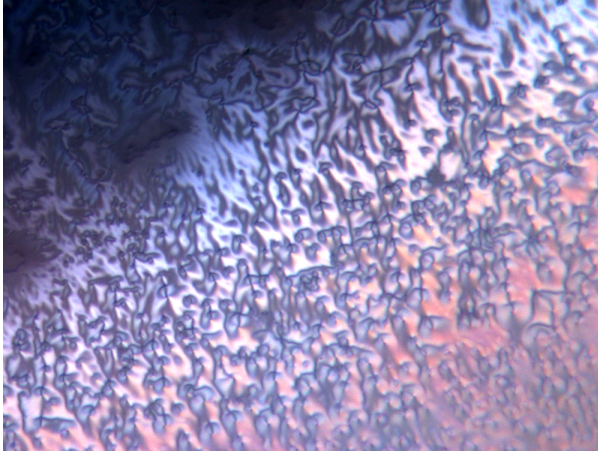


Figure 5: POM micrograph of 8CB in the nematic phase.

When the temperature controller is set to the actual transition temperature for the mixture being studied, the disclinations will quickly shift back and forth between those seen in Figures 4 and 5, as the controller cycles power to the heating element on and off to try to maintain a constant temperature, but the actual temperature is a sinusoidal wave of  $\pm 0.056^\circ\text{C}$  around the set temperature. This rapid heating and cooling is easily visible at the transition temperature, and this is how we identified the transition temperature in bulk for each mixture of 8CB and nanoparticles.[52]

### X-ray scattering

X-ray scattering was performed using a Rigaku rotating anode with a Cu source, providing X-rays with a wavelength of  $\lambda=1.54\text{\AA}$ . A bent graphite monochromator gives scans a resolution of  $\Delta q=0.012q_0(\text{\AA}^{-1})$ . A four circle Huber diffractometer, using the configuration in Figure 6, controls sample and detector positions. Our X-ray scattering experiments use a planar scanning geometry. Most scattering experiments involve moving the detector in an arc perpendicular to the substrate, which is appropriate when the variation in density (layering) that you wish to measure is coplanar with the substrate. This ensures that the incident X-rays encounter the sample at the angle ( $\theta$ ) necessary for

Bragg diffraction to occur. However for our experiments, we need to ensure that Bragg diffraction does *not* occur with the bulk liquid crystalline material, which is aligned with the molecules perpendicular to the substrate. We are not investigating the bulk material in this study, we are focusing on the liquid crystals that are realigned by the coated nanoparticles. By setting our incident beam and the detector path to be coplanar with the substrate, we prevent Bragg diffraction from occurring in the bulk liquid crystal.

Figure 6 shows the geometry used.

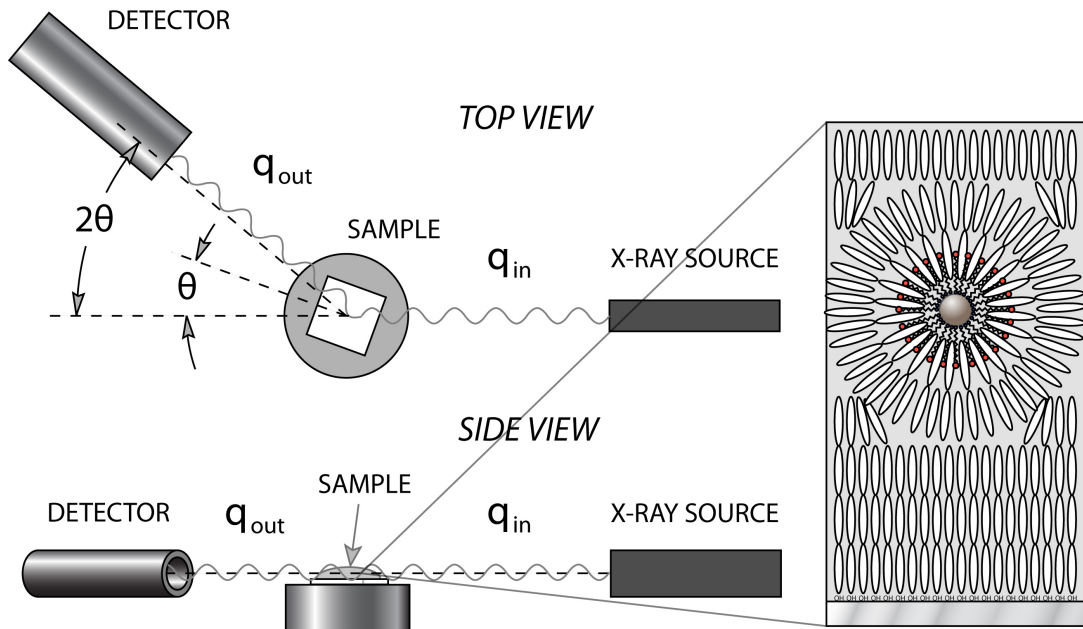


Figure 6: Schematic depicting top and side view of experimental setup. Detail shows bulk alignment to substrate with nanoparticle distortion.

The motor-controlled goniometer scanned from  $2\theta=1.5-15^\circ$ , or  $q=0.106-1.065 \text{ \AA}^{-1}$  where we expected to find the peaks which are the result of scattering from 8CB. Scans were performed above and below the smectic-nematic transition temperature found for each concentration using the polarized optical microscope.

Although the Huber diffractometer has four axes of rotation, the incident X-ray beam and the detector path are coplanar with the sample substrate, so we only need to measure  $\theta$ , the angle of sample rotation, and  $2\theta$ , the angle between the detector path and the direct X-ray beam. In programming each scan into the motor controller, we specify the start and finish angles of both  $\theta$  and  $2\theta$ , how many steps to divide the scan into, and the dwell time at each step. Disordered samples like liquid crystals will have much lower signals than crystalline ones, especially at higher  $2\theta$  angles. For this reason, we set a dwell time of 20 seconds per step to ensure enough information is collected.

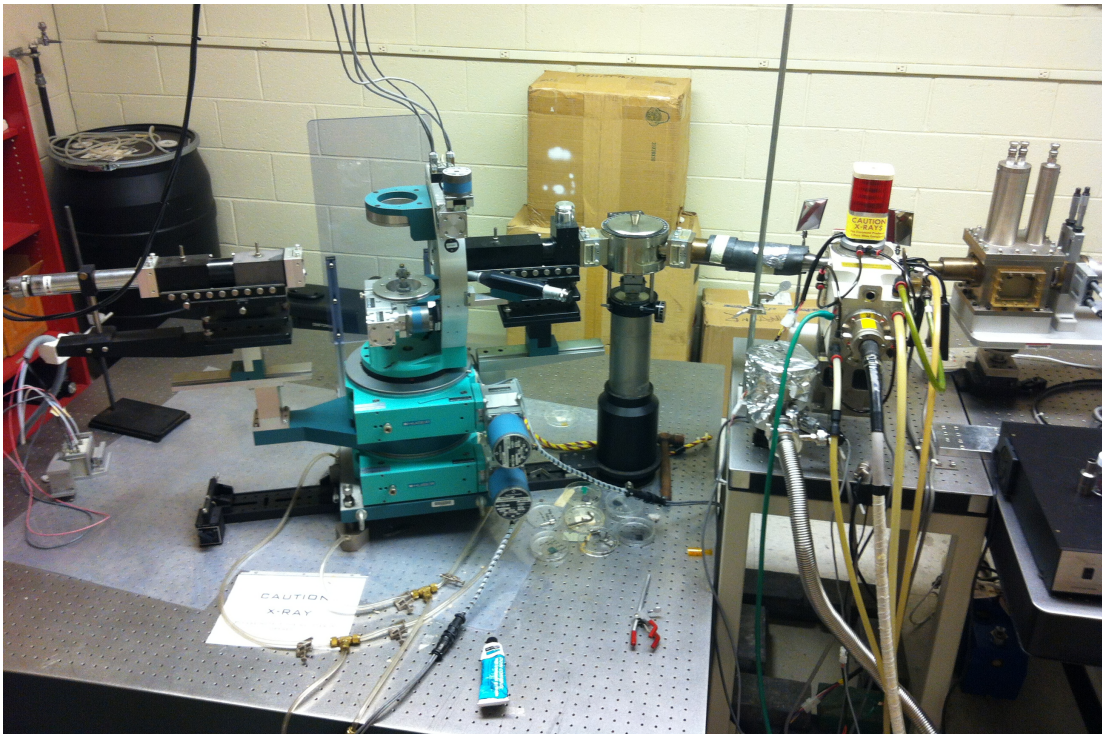


Figure 7: X-ray scattering apparatus.

We used a sample holder (seen in Figure 8) consisting of an aluminum plate (for its high thermal conductance) offset from a stainless steel base (for its poor thermal conductance), which mounts to our goniometer to obtain the temperature-based X-ray

data. The sample holder was designed and machined for our group by University of Maryland Assistant Research Scientist, Stephen Henderson.

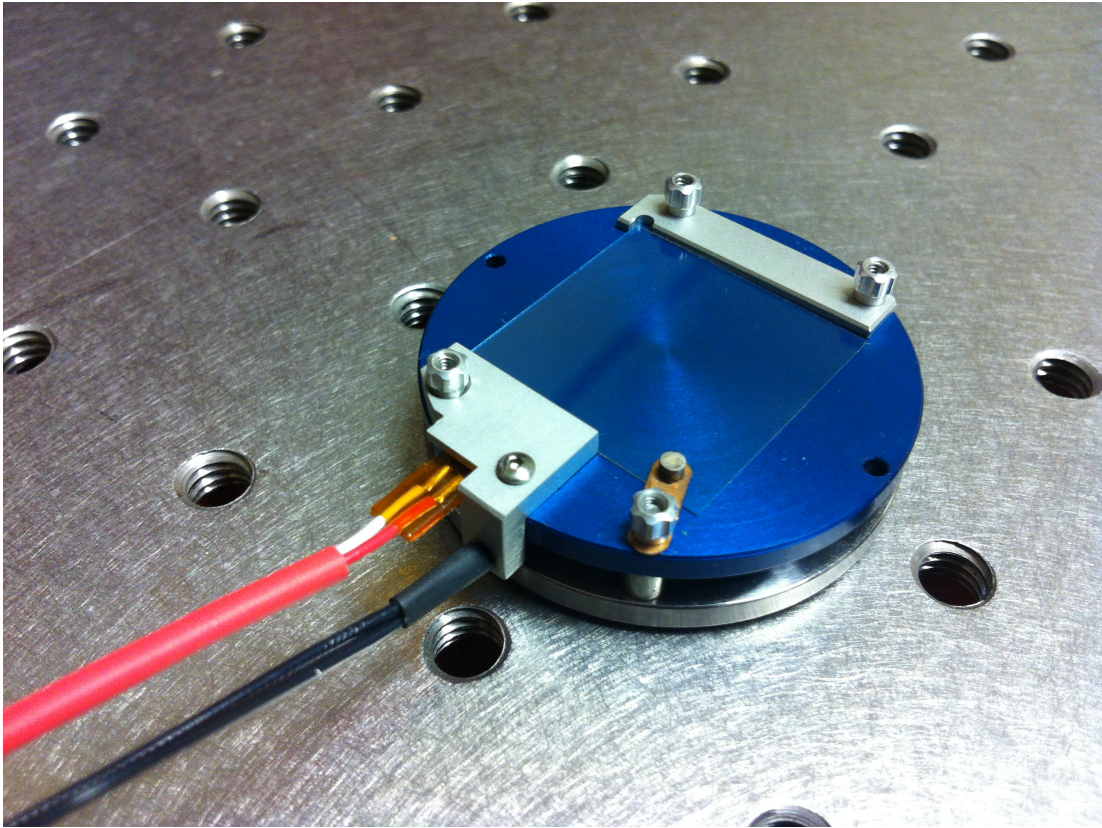


Figure 8: Sample stage with heating element and RTD.

On the underside of the aluminum plate, we have attached a kapton adhesive heating element, wired to a solid-state relay. On the top of the aluminum stage is an adhesive platinum-based RTD (resistive temperature device) sensor connected to our Fuji Electric temperature controller. The temperature controller auto tunes its PID parameters to trigger the relay, sending current through the heating element, to heat and maintain the stage's set temperature.

The long scan times needed for these experiments meant that the relay controlling the heating element would be cycled hundreds of thousands of times in a

matter of weeks, so we used a solid-state relay to ensure reliable operation. The temperature controller alone does not output enough power to activate the solid-state relay's input lines. A simple relay driver was designed and built from discrete off-the-shelf parts, which would amplify the signal from the temperature controller with power from a 9-volt battery. This is simply to provide enough power to activate the relay. A common 24-volt, "wall-wart" switching regulator powers the heating element. Initially we had concern that the 9-volt battery would need to be frequently replaced, however the driver drew so little current that a single battery performed uninterrupted for months (and millions of cycles). The temperature controller has a green indicator light that illuminates when it is outputting the signal to provide power to the heating element (in our case, that signal is going to the relay driver). However our relay driver circuit includes its own red LED indicator, which glows to confirm that power is indeed traveling through the heating element.

Our temperature controlled sample holder has the exact same vertical dimension as the sample stage that it replaces on our goniometer, so no adjustment is necessary to ensure alignment. A calibrated telescope is available to ensure that our relatively thin samples of liquid crystal mixtures are indeed in the beam line. When looking through the telescope, overlaid crosshairs indicate the center of the beam path. The column on which the sample holder sits can be adjusted vertically while looking through the telescope to move the sample into the crosshairs. The X-ray experiment samples are thick enough that their thickness is clearly visible in profile through the telescope, and the sample holder height must be adjusted so the crosshairs line up with the center of the sample's thickness.

When the desired temperature is reached, a scan is run from  $2\theta=1.5^\circ$  to  $15^\circ$ , obtaining data every  $0.02^\circ$  for 20 seconds per step. When the scan is complete, the goniometer is returned to  $2\theta=1.5^\circ$ , the temperature is adjusted and stabilized, and a scan is run with the same parameters at the new temperature without disturbing the sample. When scans at all desired temperatures are collected, we replace the sample with an identical, clean glass slide in order to collect the background scattering data. Because the signal of the photons scattered from the liquid crystal sample is so small, it is essential to remove the background data from each of the scans in the analysis phase to find the diffraction data that came from our sample and not from the substrate or sample holder.

We can plot the data from the 8CB diffracted x-rays, after subtracting from the results the background scatter data (found by scanning a blank substrate) and a Gaussian curve resulting from the direct beam from the x-ray source. We fit Gaussian curves to the data, which are appropriate for fairly short-range ordered systems like liquid crystals.[12] The center of each peak (using diffraction angle  $2\theta$  as the independent variable) allows us to find the separation distance of the ordered layers that caused them using Bragg's Law. The amplitude of these peaks is determined by how well ordered the sample is, which is always quite small for quasi-ordered materials like liquid crystals. A well ordered sample provides more layers from which the x-rays will diffract, cumulatively forming an intense peak. The full width at half maximum (FWHM) of the peak can indicate how uniformly ordered the molecules are. A narrow peak occurs when all layers are close to the same separation distance. If the layer separation is distributed through a range of values, which can happen through strain on the crystal or other forces which distort the lattice, then each layer will diffract at slightly different angles, resulting in a broader peak in the data.[53]

## Dynamic light scattering

Dynamic light scattering was used upon receipt of our FeCo nanoparticles from our collaborator, Lynn Kurihara, to characterize the particles and verify their synthesized diameter. These experiments were done using a Zeta Nanosizer DLS.

Figures 9 and 10 show the results of two such DLS experiments on a logarithmic scale, indicating that the APTS coated particles have an average size of  $4.13\text{nm} \pm 0.68\text{nm}$  diameter ( $\sigma=0.75\text{nm}$ ) for small particles and  $\pm 80\text{nm}$  diameter for clustered particles, and the PEG coated particles have an average of  $3.73\text{nm} \pm 0.68\text{nm}$  diameter ( $\sigma=0.79\text{nm}$ ).

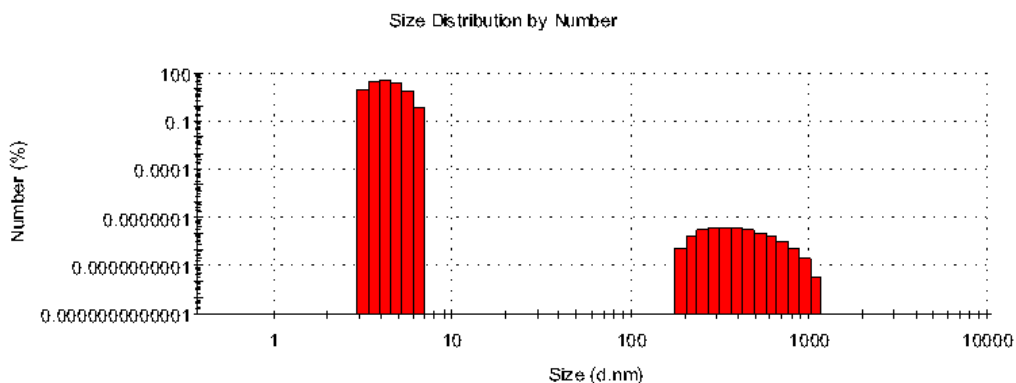


Figure 9: APTS nanoparticle DLS experimental results on logarithmic scale.

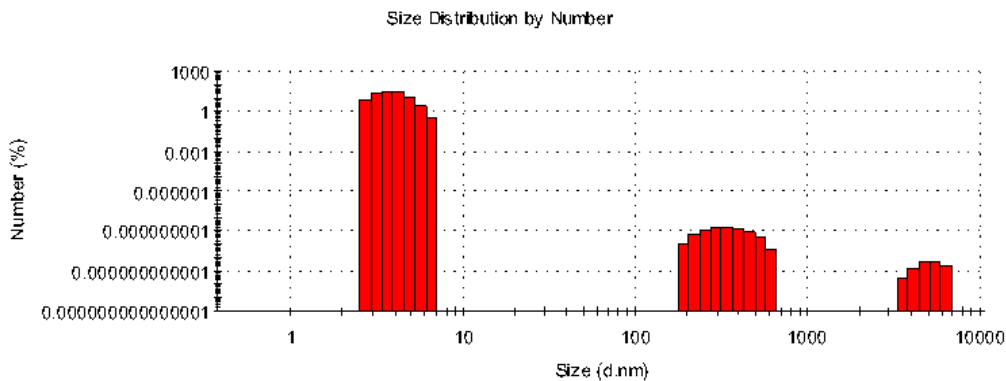


Figure 10: PEG nanoparticle DLS experimental results on logarithmic scale.

The very small number of much larger particles (200-1000nm diameter) can be separated from the sample using a magnet, but we found this to be unnecessary, as we were able to produce uniform samples without doing so.

### Samples Used and Sample Preparation

The liquid crystal we used, octylcyanobiphenyl (8CB), is a model system whose properties have been very well studied. These rod-like liquid crystals are very stable and proved reliable in our previous studies.[11, 12, 40, 54, 55] 8CB exhibits two liquid crystal phases: smectic-A at room temperature with a transition to nematic at 306.92° K.[56] Studies done by Cordoyannis, et al. identified a drop in the smectic-A to nematic transition temperature when functionalized nanoparticles are added to the 8CB. Aminopropyl triethoxy silane (APTS) coated nanoparticles cause the transition temperature to drop to 306.22° K, while mercapto hexadecanoic acid (MHDA) causes it to drop to 303.78° K.[8] We believe the interaction between these functionalized

nanoparticles and the liquid crystal molecules lowers the intermolecular attractive energy between liquid crystal molecules, thereby lowering the amount of energy needed to disorder the film or bulk sample.

We studied nanoparticles coated with several different functionalization compounds: mercapto hexadecanoic acid (MHDA, used in research to stabilize biological

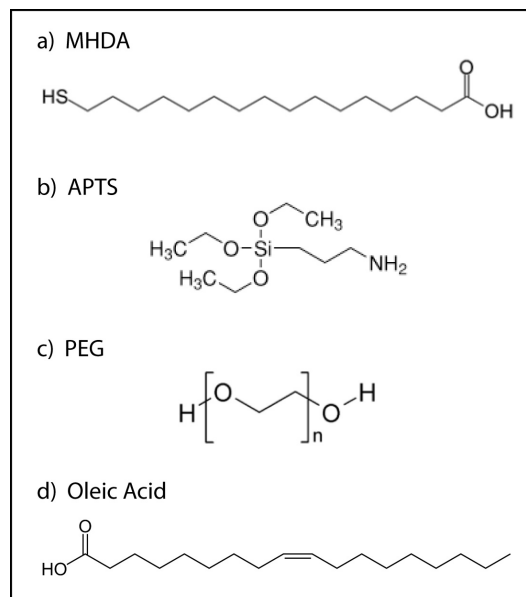


Figure 11: Chemical structure of functionalization compounds.

interactions [38]), aminopropyl triethoxy silane (APTS, commonly used for labeling molecules [57]), and high molecular weight polyethylene glycol (PEG 3000), see Figure 11. We chose each of these compounds for their wide use in biological applications,[38] and for their unique interactions with our hybrid systems. Our previous research has shown that APTS, MHDA, and PEG-covered particles affect liquid crystal ordering both with and without a magnetic field,[12, 55] but in opposite ways.

We also have access to and ZnO particles coated in oleic acid, in the same size range as our FeCo particles. Our group synthesized these particles for a related project on photovoltaics using nanoparticles to align liquid crystals.[54] [58] Including them in this study will both provide us with a non-functionalized control nanoparticle, an ionic material that differs from the metallic FeCo particle, and valuable behavior data for both projects.

The FeCo nanoparticles were synthesized in a polyol process before being coated with their functionalization compound.[59-61] The functionalization compound is dissolved in ethanol at a ratio of 1mg/1ml. This solution is then added to the suspension of bare nanoparticles and mixed for 30 minutes.

We tried a number of different deposition techniques to prepare our samples. We explored using both silicon and glass substrates and found that glass slides typically formed the best films due to glass's natural hydroxyl termination,[62] which attracts the 8CB's cyano group because they are both hydrophilic, while the 8CB's carbohydrate chain is hydrophobic. Silicon substrates were used in early experiments, but since they are not naturally hydroxyl terminated[63], preparing them would involve exposure to an oxygen plasma or treatment with piranha solution (a mixture of concentrated sulfuric acid and hydrogen peroxide), which is highly corrosive.[64] Both of these processes add

unnecessary complication that can be avoided simply by using glass instead. The glass slides are cleaned using acetone and ethanol, but the surface is not rubbed clean, as this would create grooves in the substrate that would affect the orientation of 8CB molecules.[16, 17] The substrate is then heated to 50°C, above the isotropic temperature for 8CB, prior to deposition.

We receive the functionalized nanoparticles suspended in ethanol, so when making samples, the nanoparticles must be isolated by evaporating the ethanol and weighed. We then add 8CB to the isolated nanoparticles to achieve the desired concentration for the sample being made. When making thin films, the sample is then diluted with ethanol to aid in mixing. To homogenize the mixture, we sonicate the sample for five hours at 50°C. For X-ray scattering, the sample must be thick enough to intersect the x-ray beam, so the mixture remains undiluted but is also sonicated at 50°C for five hours.

When sonication is complete, a small amount of the mixture can be transferred to the substrate. For thin film samples, the mixture is deposited onto a heated glass slide, at which point the ethanol quickly evaporates, and the sample is allowed to cool to room temperature. In the nematic phase, the 8CB molecules are pointing (on average) in the same direction, but are mostly disordered. When entering the smectic phase the molecules aggregate side-by-side into layers, oriented almost normal to the layer planes.[2] If the functionalized nanoparticles are present when this happens, the nanoparticle will inhibit this ordering over a short distance. When the transition into the smectic-A phase is complete, the sample can be studied. In the isotropic phase, the mixture flows quite easily, creating areas at the edges of the sample that form into

monolayers and bilayers when the smectic phase is established. These are our target areas of research for AFM studies.

Spin coating is a well-known method of producing thin films from solution. However our attempts at utilizing this method were disappointing. The liquid crystal flows well in the isotropic phase (on a heated substrate), but its thick consistency in the smectic phase causes it to bead on the surface at room temperature. Our spin-coating equipment lacks temperature control, so samples spun in the smectic phase at room temperature resulted in very well dispersed microscopic beads of 8CB that refuse to wet the surface (even after annealing). If we were able to spin the substrate while the liquid crystal was isotropic (around 50°C) the material would wet the surface nicely and spread evenly across the glass.[65] Attempting to accomplish this using hot air guns and incandescent light bulbs (as improvised heating elements) resulted in inconsistent and uneven coverage at best.

## Chapter 3: Bilayer film studies with AFM

### Theory and background

There have been many studies of particles and liquid crystals, mostly focused on the nematic (disordered) phase. Our research group has previously studied bulk mixtures of the liquid crystal octylcyanobiphenyl (8CB) and functionalized FeCo nanoparticles. These studies were able to show that compounds such as aminopropyl triethoxy silane (APTS), which tend to align the liquid crystal molecules almost tangential to the surface of the nanoparticle, will locally disorder the liquid crystal.[50] 8CB ordinarily has a smectic phase at room temperature, but when nanoparticles with these compounds are present, the liquid crystal experiences a smectic-nematic transition in proximity to the nanoparticle.[12] In contrast, mercapto hexadecanoic acid (MHDA), a compound that aligns the liquid crystal almost normal to the surface of the nanoparticle, will assist in aligning the liquid crystal (rather than disordering it) in the vicinity of the nanoparticle. Here, no phase transition takes place. We have explained this behavior as a competition between the mechanical and the ordering energies, magnetic and nanoparticle size:[12, 40]

$$E = E_{\text{mech}} + E_{\text{magnetic}} + E_{\text{surface interaction}} + E_{\text{relative size}}, \quad (1)$$

Further analysis of this formula can be found in the Results section.

In 2009, Roiter et al. found that bare silica nanoparticles will interact with a phospholipid bilayer differently depending on the size of the nanoparticle. The group reported that nanoparticles between 1.2 and 22 nm will disrupt the ordering of the phospholipids and open a hole in the bilayer around the particle. Particles larger than 22

nm or smaller than 1.2 nm were entirely covered by the membrane, unless the large particle featured a protrusion within the specified size range (Figure 12).[1]

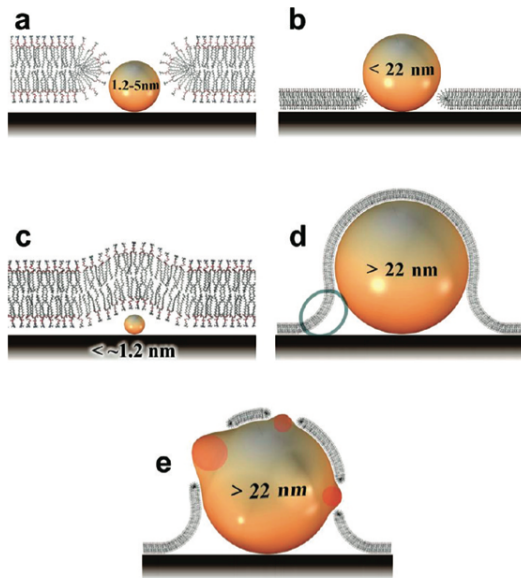


Figure 12: Interactions between lipid bilayer and a bare silica nanoparticle of varying size. (Roiter, et al.)[1]

In such a case, the majority of the particle would be covered, but the protrusion would remain exposed. Roiter et al. developed a model attributing this phenomenon primarily to the mechanical properties of the phospholipid. If the energy lost due to bending the membrane costs too much energy, the membrane forms a defect around the offending obstacle in the form of a hole.[1]

Roiter, et al., modeled the thin film system as a sheet of beads and harmonic springs, stretched over the bare silica nanoparticles they were studying. The intermolecular attraction of the membrane's molecules and its surface tension held it together. The radius of curvature required to cover the nanoparticle determined whether or not the springs would be stretched too far, breaking the bonds and rupturing the membrane.

Roiter later found that an energy model, taking into account experimentally measured mechanical properties of the film and energy from distortions, was more

accurate in describing a membrane's behavior. Our own energy model makes use of these same principles in addition to other energy factors as well.

While a simple model worked well for Roiter's work with bare silica nanoparticles, our nanoparticles have additional factors that are the main focus of this study. We are primarily investigating how a functional coating on the nanoparticles affects the hole-forming behavior. Surface interactions are very influential on the nano scale, thus the interaction between the functional molecules and 8CB will heavily affect the ordering of the membrane.

The functional molecules do not chemically react with the 8CB molecules. Any interaction between the two materials occurs electrostatically and is physical in nature. Neither material changes its chemical structure, nor do they bond in any way.[21] The functional molecules effectively change the shape of the nanoparticle surface to dictate how the 8CB molecules will orient at the interface.

MHDA molecules orient normal to the surface of the nanoparticles, which allows 8CB rods to fit between them, aligning the hydrocarbon chains of the 8CB tails with the hydrocarbon chain in the middle of the MHDA molecule, and also aligning the carboxylic group of the MHDA with the aromatic rings in the center of an 8CB rod. The two molecules do not react or bond with each other. The alignment that occurs creates a structure on which further smectic layers of 8CB may develop.

APTS molecules, in contrast, lay flat against the surface of the molecule. 8CB rods at the interface with this functionalization will lay almost tangential to the surface of the nanoparticle. Smectic layers can still form from this orientation, but the layers would form with their director tangential to the surface of the nanoparticle, rather than normal to it, as is the case with MHDA-coated particles.

PEG is an interesting case. It attaches to the nanoparticle in much the same way as MHDA, but it is a much longer molecule. At molecular weight of 3000 daltons, the length of the PEG molecule is about 268.1Å at full extension (or about 8.5 8CB rod lengths), compared to just 10.5Å for MHDA. This means that close to the nanoparticle, the PEG will have the same orienting effect as the MHDA, but the PEG molecule will reach out into the bulk 8CB smectic layers and will have a stabilizing effect on the 8CB rods closest to the nanoparticle.

The  $\text{Fe}_{48}\text{Co}_{52}$  nanoparticles used in this study were synthesized to theoretically be 2 nm in diameter and coated in their respective compounds by our collaborator, Lynn K. Kurihara, at the Naval Research Laboratory. We determine the real diameter by light scattering, as seen in Figures 9 and 10. Due to their magnetization, Van der Waals attraction, and electrostatic forces, a portion of the nanoparticles agglomerate over time into larger quasi-particles of varying size, as seen in Figure 13. The nanoparticles underwent a thorough washing procedure: magnetically separate, decant off supernatant, re-suspend, and repeat five times. Then the particles are magnetically separated again and washed in a turbulent flow. The process was monitored by magnetization/XRD and TEM results. These particles did not show any degradation in VSM, and the TEM images showed minimal presence of unwanted precipitates. The particles were characterized for magnetic properties, and an X-ray powder diffraction experiment was performed to confirm the formation of  $\text{Fe}_{48}\text{Co}_{52}$  [Lynn K. Kurihara, personal communication].

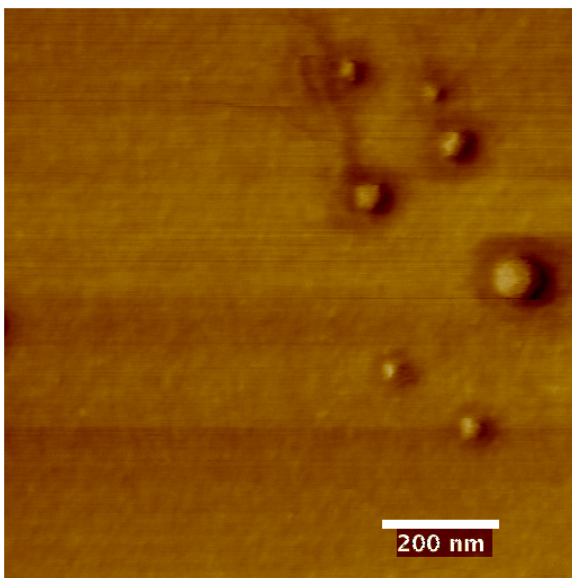


Figure 13: AFM micrograph of MHDA-coated FeCo nanoparticles on glass substrate.

These larger particles can be broken back into smaller agglomerated particles through sonication, which is utilized in this study to ensure the particle size distribution is within the target range. As seen in Figure 9, dynamic light scattering showed the majority of particles in the 2 nm diameter range. Our X-ray scattering experiments confirm the majority of the nanoparticles are not agglomerated.

Each MHDA molecule is attached to the nanoparticle by the thiol group, leaving the hydrophilic carboxyl group at the other end of the molecule to extend out into the aqueous medium (Figure 14). This orientation, normal to the attached surface, attracts the charged cyano group at the “head” of the 8CB molecule, and repels the hydrophobic carbon chain “tail”, as seen in Figure 15-a. While the MHDA molecule is covalently bonded by the thiol group to the nanoparticle, the interaction with the 8CB molecules is purely physical.

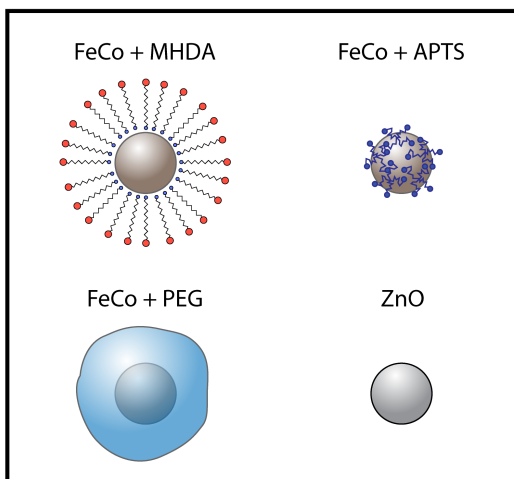


Figure 14: Schematic depicting orientation of coating compounds on their respective nanoparticles.

APTS molecules attach to the nanoparticle surface by the amine group, and the hydrophobic branches lay flat against the nanoparticle when in an aqueous medium (Figure 14). This effectively makes the nanoparticle surface hydrophobic. Because 8CB molecules will interdigitate with their biphenyl rings side-by-side, (Figure 15) a rod-shaped bi-molecule is formed with hydrophobic ends and a hydrophilic middle. The 8CB molecules will lay almost tangential to the surface of the APTS-coated particle (Figure 16-b). These two different liquid crystal-nanoparticle interactions are the primary factor that affects how these nanocomposite systems behave.

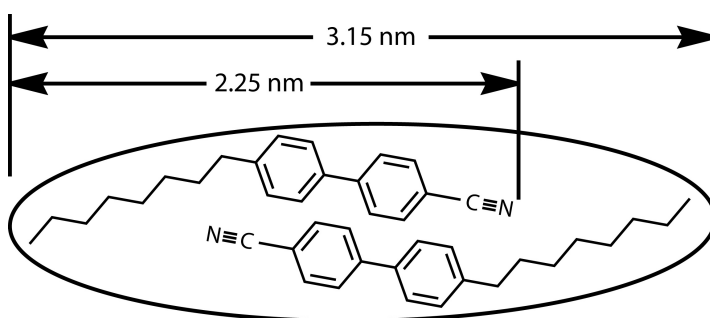


Figure 15: Two 8CB molecules interdigitate to form a "rod" approximately 31.5 Å long with hydrophobic ends and a hydrophilic middle.

The energy of the system changes when the coating compounds cause the liquid crystal molecules to reorder upon exposing liquid crystal thin films to functionalized nanoparticles. The coated nanoparticle distorts the smectic layers of the liquid crystal system, forcing the 8CB molecules to either form layers around the particle, and/or form

defects in its vicinity.[66] The “bump” that is formed by an unbroken liquid crystal membrane covering a nanoparticle increases the surface area of the system. The bend, twist, or splay of the 8CB membrane induced by the nanoparticles (see Figure 17) and the change in surface interactions due to increased surface area add to the energy of the system depending on which interactions take place.[12, 67, 68]

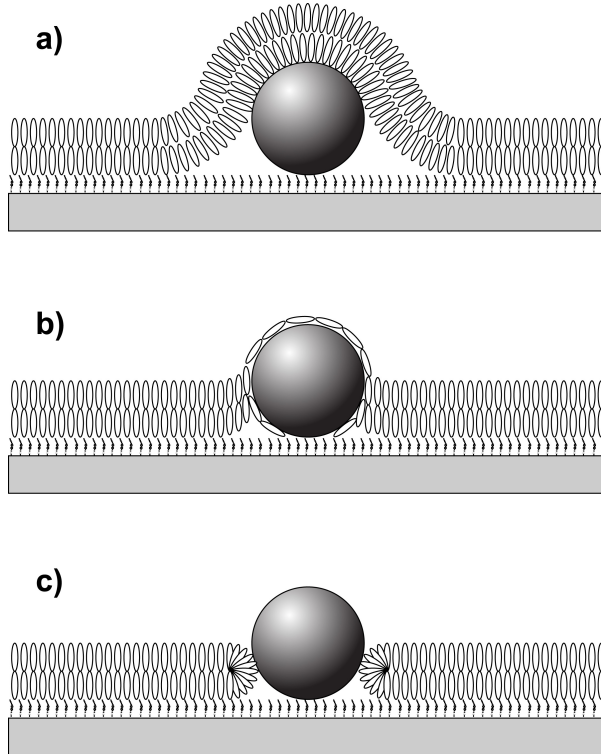


Figure 16: Possible interactions between coated nanoparticle and an 8CB membrane. a) Nanoparticle covered by membrane. b) Nanoparticle coated with tangential molecules, disrupting membrane order. c) Nanoparticle forms hole in membrane. Note: nanoparticle in schematic is approximately 12nm in diameter.

In the case of Figure 16-a, the energy is increased due to the bend imposed on the membrane, as well as by the increased surface energy. Because a system of lowest energy is desired, a hole forms when the bend/twist energy exceeds the increased surface energy (as shown in Figure 16-c). In the case of Figure 16-b, less energy is added due to the introduction of splay in the liquid crystal structure.[69] Splay is the dominant mechanical energy for this interaction, which is what we expect to find with the APTS particles.[12] See Figure 17 for the disclinations found in liquid crystals.

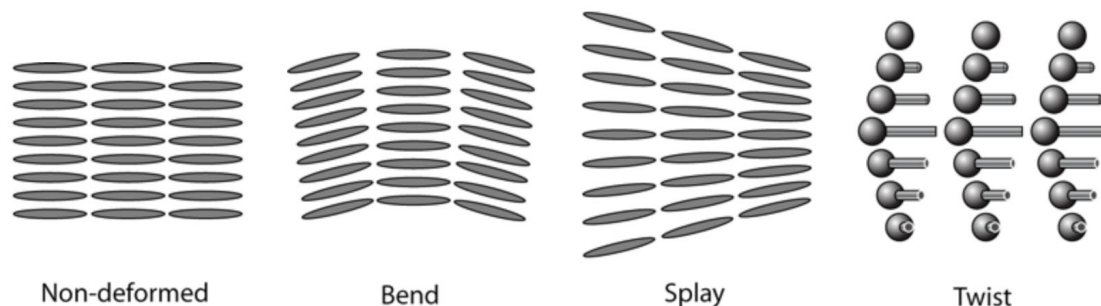


Figure 17: Liquid crystal deformations found in the smectic phase.

## Results

### MHDA

Films consisting of 30% weight of nanoparticles in 8CB were prepared as described in Chapter 2, and deposited on glass wafers heated to 50° C, above the clearing point of 8CB. The film and substrate cooled to room temperature, establishing the smectic layers. When the films were observed under AFM, the smectic layers are easily distinguished. Dispersed nanoparticles can be seen randomly distributed throughout the samples.

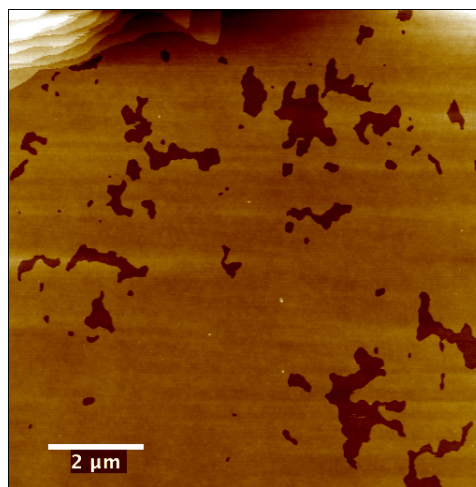


Figure 18: AFM micrograph of an 8CB monolayer with dispersed MHDA-coated nanoparticles. Dark areas are bare substrate.

Figure 18 is an AFM scan showing an 8CB thin film with interspersed MHDA-coated nanoparticles. The dark areas are bare glass substrate, and smectic layers of a thicker portion of the sample are visible in the upper left corner. The even elevation across this image suggests this is a single smectic layer. This can be confirmed through comparing elevation data of the film and the bare

substrate, a difference of  $\sim 3\text{nm}$  (Figure 19). A single 8CB molecule is approx.  $2.25\text{nm}$  long, while the interdigitated bimolecule is about  $3.15\text{nm}$  long.

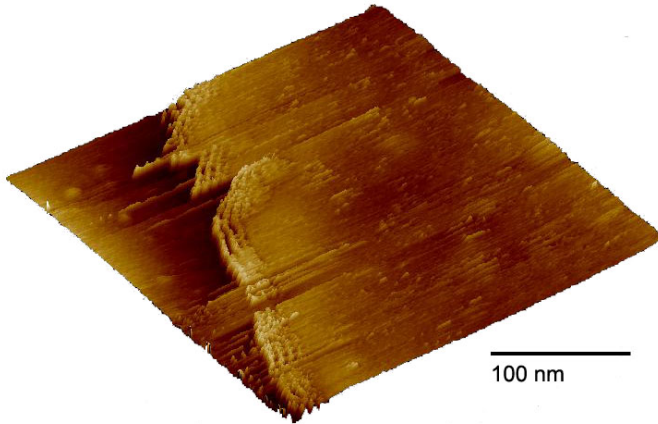


Figure 19: AFM micrograph of 8CB monolayer at edge of sample, displaying step edge phenomenon.

Figure 20 is a closer view of Figure 18 (about  $2\ \mu\text{m}$  square), showing the randomly dispersed nanoparticle clusters of various sizes.

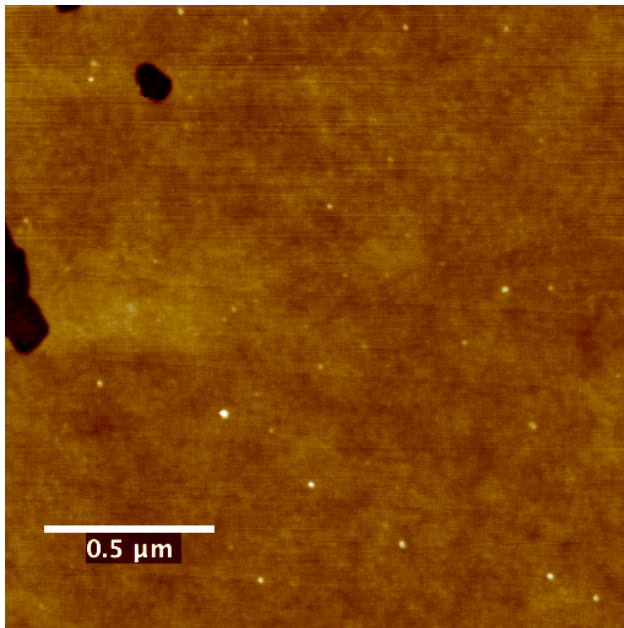


Figure 20: AFM micrograph of 8CB monolayer with dispersed MHDA-coated nanoparticles.

We are unable to determine whether a nanoparticle is covered or exposed at this scale. Figures 21 and 22 are the elevation and phase data (respectively) from a small  $400\text{nm}$  square area of the film.

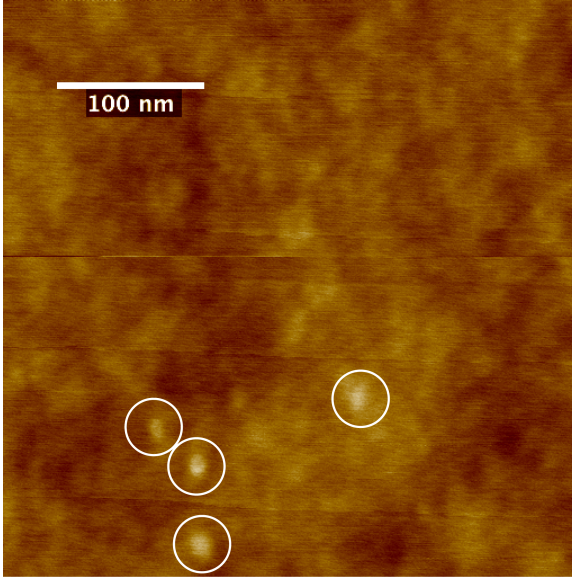


Figure 21: AFM elevation data micrograph of MHDA-coated nanoparticles in an 8CB thin film. White circles show four nanoparticles present in this image.

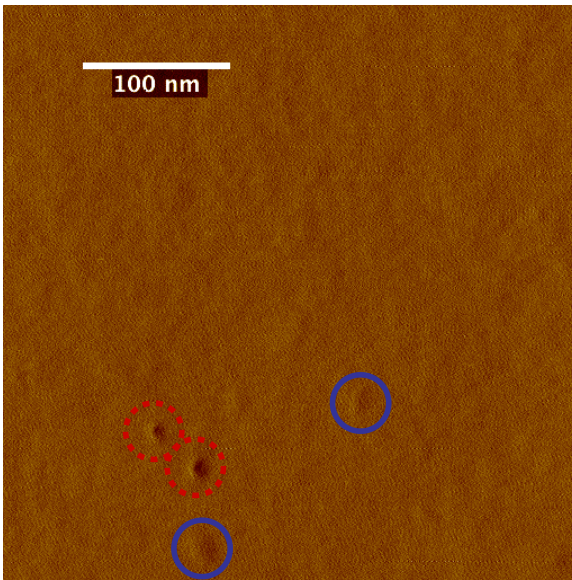


Figure 22: AFM phase data micrograph of MHDA-coated nanoparticles in an 8CB thin film. Red dotted circles show two exposed nanoparticles. Blue solid circles show two covered nanoparticles.

With larger particles, it is often possible to tell whether a nanoparticle is covered with liquid crystal with the elevation data alone. If the elevation data is ambiguous, if confirmation is needed, or when the AFM's resolution prevents clear determination of whether a particle is covered or exposed, the elevation image (Figure 21) must be compared to the phase image (Figure 22) to distinguish hard FeCo particles from soft 8CB liquid crystals. Low contrast of the phase image indicates continuation of the

membrane (a covered particle, solid blue circle), whereas high contrast indicates a change in material (exposed particle, dotted red circle).

Four small nanoparticle clusters (circled in white) are clearly visible in the elevation data (Figure 21) with approximately the same brightness (height). The phase data (Figure 22) shows two of the nanoparticles in dark contrast from the surrounding liquid crystal, indicating that these nanoparticles are exposed. The other two nanoparticles, however, are nearly the same color as their surroundings, telling us that they are covered by liquid crystal film. This type of image allows us to determine the size dependence of which particles form holes in liquid crystal films.

#### APTS

Figure 23 is a film of 8CB with APTS-coated nanoparticles. The smectic structure is clearly visible in this thicker area of the film, but at this scale the nanoparticles are too small to discern.

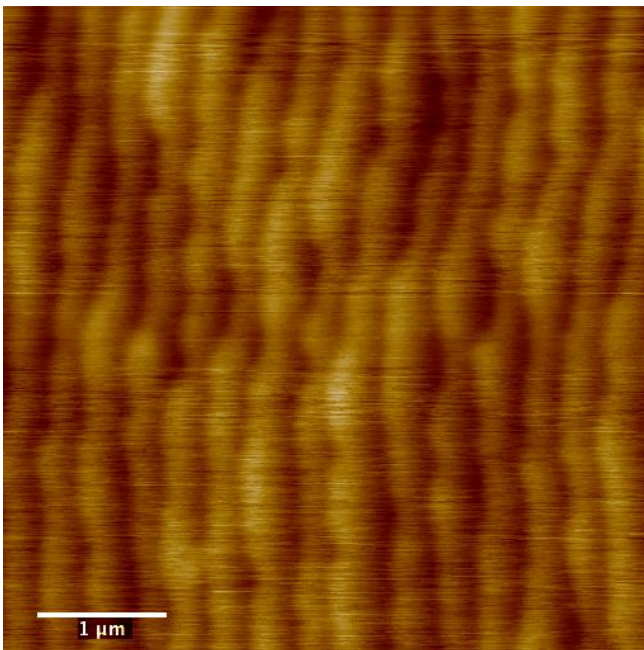


Figure 23: AFM elevation data micrograph of 8CB smectic layers. No nanoparticles distinguishable at this scale.

Figure 24 shows a much closer view of a thin portion of the same sample with partially embedded APTS-coated nanoparticles visible in the film.

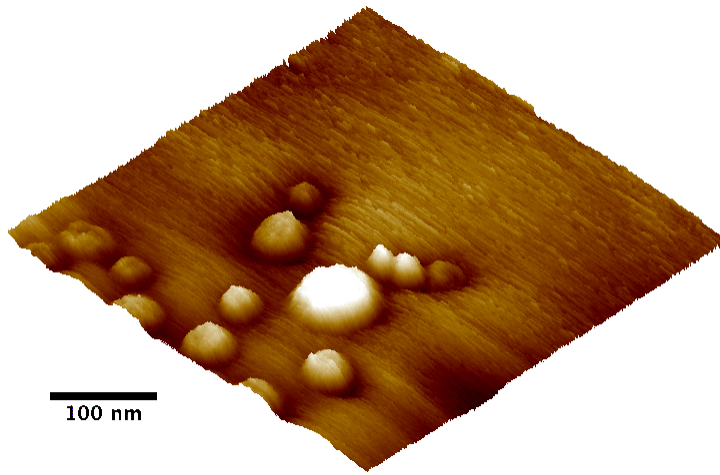


Figure 24: 3D micrograph constructed from AFM elevation data of APTS-coated nanoparticles in 8CB thin film.

These particles are large enough that we can clearly see in the elevation data that they are not covered in a continuous film, but have formed holes in the liquid crystal. The particles visible here range in size from 25 to 65 nm in diameter. This is far outside the range of 1.2-22 nm given by Roiter, et al.[1] It is unusual that these particles were found in such close proximity to each other. It is possible that due to the larger size of these particles, the system lowers the energy needed to form holes around the particles by combining two distortions (holes) into a single figure-8, or clustering many particles to surround them with a single, oddly-shaped hole.[51, 70, 71]

## PEG

AFM scans of films containing PEG coated nanoparticles (Figure 25) show particles covered with liquid crystal membrane over a large range of sizes (48nm to 143nm diameter).

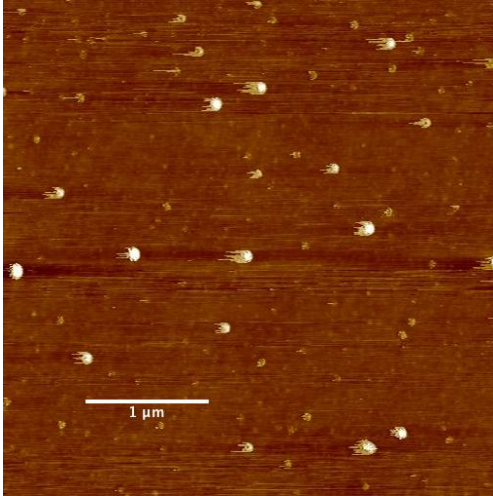


Figure 25: AFM micrograph of PEG-coated nanoparticles in an 8CB thin film.

PEG is a relatively large, hydrophilic molecule and is soluble in water, so it extends a significant distance from the surface of the nanoparticle. The various size ranges of functionalized particles and their interaction with the membrane is summarized in Table I.

Figure 26 is a large nanoparticle cluster, coated in PEG, clearly covered with liquid crystal film. The dark areas beside the particle are artifacts of the AFM scan.

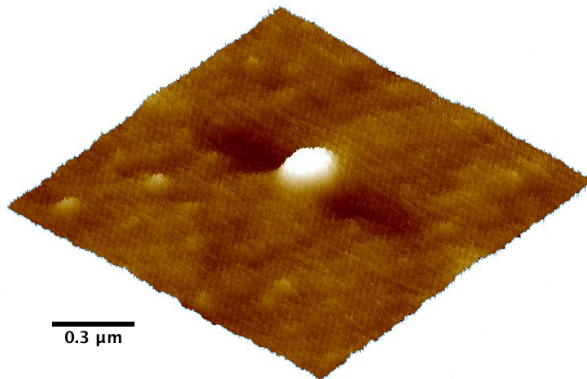


Figure 26: PEG-coated nanoparticles covered by 8CB thin film.

The large particle here is 143 nm in diameter, while the smaller particles also visible in this image are around 48 nm. All particles shown here appear to be covered by the film.

## ZnO

Figure 27 shows smectic layers of 8CB mixed with ZnO, and the phase data (Figure 28) suggests that the nanoparticles are either pushed to the edges of the smectic layer during the transition from the nematic phase or accumulate there by some other mechanism, probably by forming dipoles or quadrupoles in the liquid crystal molecules. If they are not functionalized they maximize phase separation. [72]

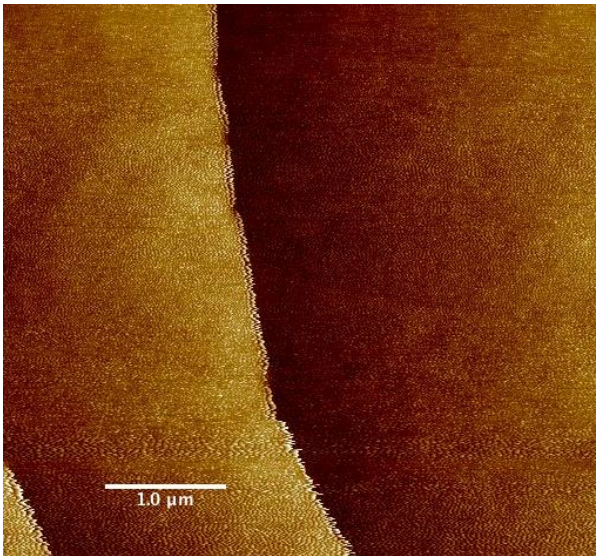


Figure 27: AFM micrograph elevation data of 8CB smectic layers with ZnO nanoparticles visible at edges of smectic layers.

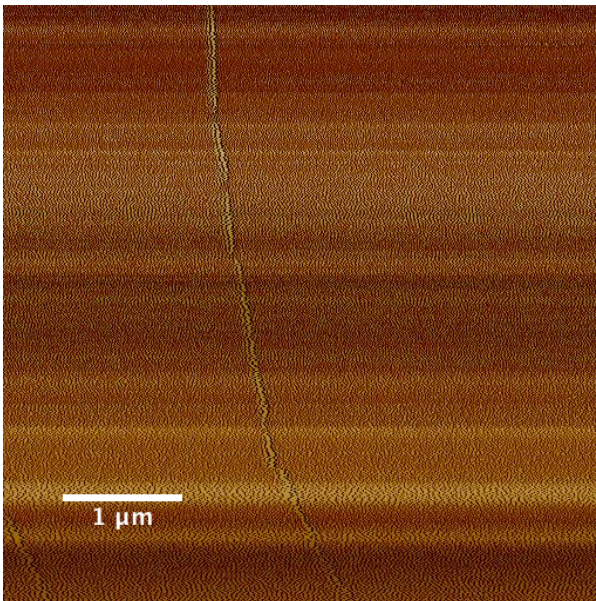


Figure 28: AFM micrograph phase data that corresponds to elevation data in Figure 24. Material hardness change is visible at the edge of this smectic layer.

## Analysis

Finding nanoparticles amongst the films of 8CB has proven to be the greatest hindrance to collecting data. The size ranges of the particles we have been able to identify as either covered or exposed are summarized in Table I.

Table I: Functionalized Nanoparticle Interaction				
	Silica particles (Roiter et al)	MHDA	APTS	PEG
Covered	< 1.2 nm			
Uncovered	1.2 - 22 nm	7 – 10 nm	23 – 66 nm	
Covered	> 22 nm	> 12 nm		> 48 nm

We have found covered MHDA nanoparticles inside the uncovered size range stated by Roiter, and we have found uncovered APTS nanoparticles outside the uncovered size range. This suggests that the functionalization compound influences hole-forming behavior.

It is our theory that the component  $E_{\text{mech}}$  in equation 1 increases when the liquid crystal molecules of the film must bend, twist, or splay (see Figure 17) to cover the nanoparticle. Splaying is a low-energy distortion, while bending is a high-energy distortion due to the rod-like shape of the 8CB molecule.[12] The film has an increase in surface area when distorting to cover a nanoparticle, thus increasing the energy due to the component  $E_{\text{surface interaction}}$ . Therefore, if the energy gain due to mechanical distortion is greater than the energy gained from the increased surface area, the liquid crystal chooses the lower energy option of organizing around the particle, forming a hole. Since bending the organized liquid crystal film requires more energy than splaying the molecules, an interaction requiring bending would be more likely to form a hole than one in which splay is the dominant distortion. With MHDA's tendency to align the

nanoparticles perpendicular to its surface (see Figure 14), Figure 16-a is the most likely interaction, which involves bending. From this we can predict that a nanoparticle covered with MHDA would be more likely to form a hole in the liquid crystal film than one in which splaying was the required distortion, such as APTS (see Figures 14 and 16-b).

We found that coating a nanoparticle will change the size range at which a hole forms in a liquid crystal membrane. The membrane enveloped MHDA-coated nanoparticles when the nanoparticle size exceeded 12 nm in diameter, compared to the 22 nm diameter found by Roiter, et al. APTS-coated nanoparticles, on the other hand, were uncovered as large as 66 nm in diameter. We were unable to find PEG coated nanoparticles that were uncovered, suggesting that hole formation may not occur at all with this functionalization. These results are in the same order of magnitude as the findings of Roiter, et al., but they clearly demonstrate the ability of nanoparticle functionalization to affect the behavior of the membrane. In a biological application, a nanoparticle may penetrate a membrane if coated in MHDA or APTS as long as the nanoparticle is within the known “uncovered” size range. If penetration is to be avoided, a coating of PEG may prevent membrane perforation.

## **Chapter 4: Bulk studies with X-ray scattering as a function of temperature**

### Background

Our AFM experiments provided us with a topographical view of liquid crystal membrane interactions with coated nanoparticles with a very narrow focus (whatever was visible in the scanning area of a few square micrometers). To obtain a more comprehensive view of the interaction in a bulk sample, rather than a thin film, we utilized X-ray scattering with a unique experimental geometry as previously discussed. This technique allows us to measure the average orientation of the liquid crystal molecules, the correlation length of ordered molecules, and identify areas of smectic ordering present in a nematic bulk[53].

Our X-ray scattering experiments were performed on samples containing 30% weight concentration of FeCo nanoparticles coated with MHDA or PEG in 8CB liquid crystal. The goal of these scans was to assess the behavior of the liquid crystal starting at room temperature, 26.7° C (299.8° K) and raising the temperature of the sample above the smectic-nematic transition temperature, which varies depending on the functionalization compound used on the nanoparticles.[8] Our group has previously studied similar samples using X-ray scattering;[11, 12, 40, 55] however, those experiments studied the effect of a magnetic field on the alignment of the liquid crystals, rather than varying the temperature of the sample.

8CB liquid crystals exhibit a smectic-A phase, which is characterized by molecules that arrange in layers and orient normal to the smectic layers.[2] When deposited on a hydrophilic substrate, such as glass or a similar surface with hydroxyl termination, the liquid crystal “rods” maintain this orientation (see Figure 29).[73] Given the geometry of our experimental setup, incident X-rays are coplanar with the smectic layers that are parallel to the substrate, and thus will not diffract off of these layers.[53, 74] Therefore the only layers that will cause constructive interference are those that are distorted by presence of nanoparticles (refer to Figure 12).

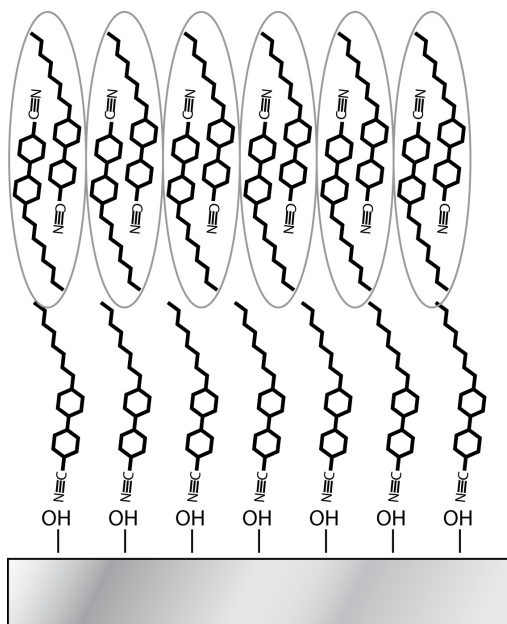


Figure 29: Glass substrate has hydroxyl termination, which attracts the hydrophilic ends of 8CB molecules, leaving the hydrophobic tail exposed to interdigitated 8CB rods.

Our X-ray scattering experiments are done in a planar geometry. This geometry is described in Chapter 2 and illustrated in Figure 6. If the bulk liquid crystal is in the homeotropic alignment, the only signal detected in this geometry is that caused by the nanoparticle. This is why our signal is quite small, but only contains the information from the interaction we are studying.

Consider a sample of homeotropically aligned 8CB to further support our assertion that our data is not the result of scattering within the bulk. The physical

influence of the nanoparticles on a liquid crystal system can be pronounced. In Figure 30, we see a mixture of 8CB and APTS-coated nanoparticles as viewed through a polarized optical microscope. The homeotropically aligned 8CB appears black under the polarized light. Both the nanoparticles and the defects or dislocations surrounding APTS nanoparticles have clearly attained a level of ordering in the bulk 8CB.[12, 40]

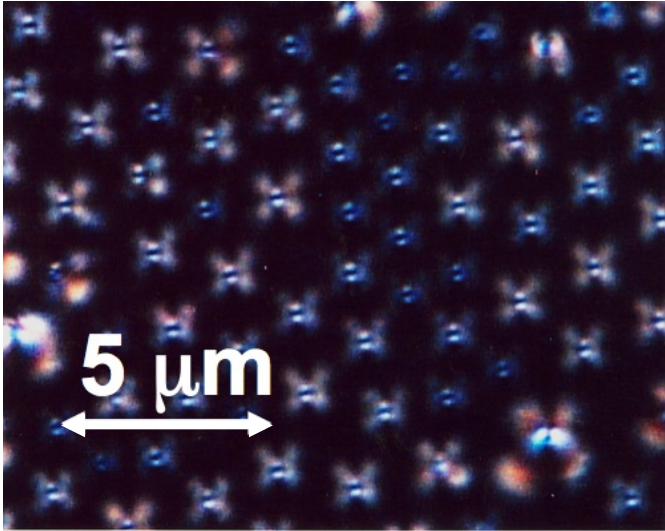


Figure 30: Polarized optical micrograph of 8CB and APTS-coated nanoparticle mixture.

8CB is a model system and has been very well studied. The literature tells us that homeotropically aligned 8CB gives a very disordered X-ray scattering signal with a high  $q$ -value center. Our data range spans approximately  $q=0.1-1.2$ , but the signal for homeotropic 8CB is centered approximately at  $q=1.7-2.0$ . Our PEG experiments actually picked up this signal, as it is so disordered it spread into the upper range of our data. Knowing that it was not the signal we were studying, this disordered signal was removed prior to fitting our final Gaussian curves.

We began with room temperature scans to identify what peaks are present in analyzing the very large amount of data we obtained. We are primarily concerned with the center position and the full width half maximum (FWHM) of each peak, as these let us calculate the  $d$ -spacing and correlation length, respectively. With this data you can

calculate the average tilt angle of the molecules responsible for this peak, as well as how well ordered those molecules are.[75] Tall, narrow peaks have a small FWHM, so they have a large correlation length and are better ordered than shorter, broader peaks.

Our first set of data used a sample containing MHDA-coated nanoparticles. Our first scan was conducted at room temperature, well into the smectic range for this sample. The sample was deposited on a glass slide straight from the sample vial, so the act of depositing the viscous 8CB disordered it to some degree. We scanned this sample as-is to obtain a baseline to see what effect annealing would impart on the data. This, and all future scans were performed with the X-ray power set to 50kV and 100mA. Knowing the size of our liquid crystal molecule and its general orientation in the smectic phase, we can use Bragg's law to predict that the scattered signal will occur between the  $2\theta$  angles of  $1^\circ$  and  $15^\circ$ . The raw data, as shown in Figure 31, does not reveal much in its current form.

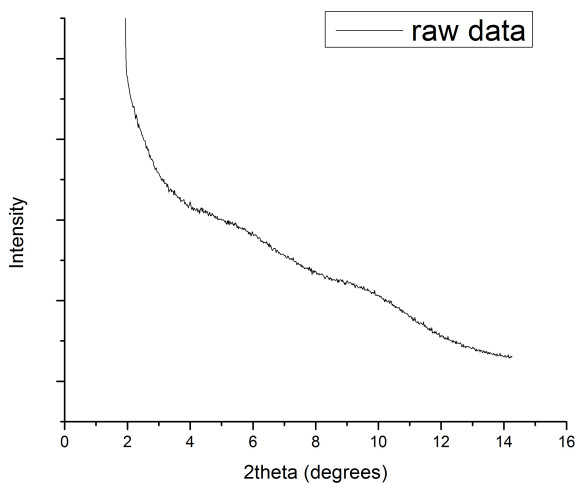


Figure 31: raw data from X-ray scattering experiment at room temperature with a 30% MHDA nanoparticle sample.

Before running this experiment, we scanned an identical glass slide with no sample deposited in order to obtain the scattering data from the substrate, sample holder, and anything else the X-ray photons interact with other than the sample we are studying. We

can then subtract that data from our raw results, and a more revealing curve is created, as seen in Figure 32.

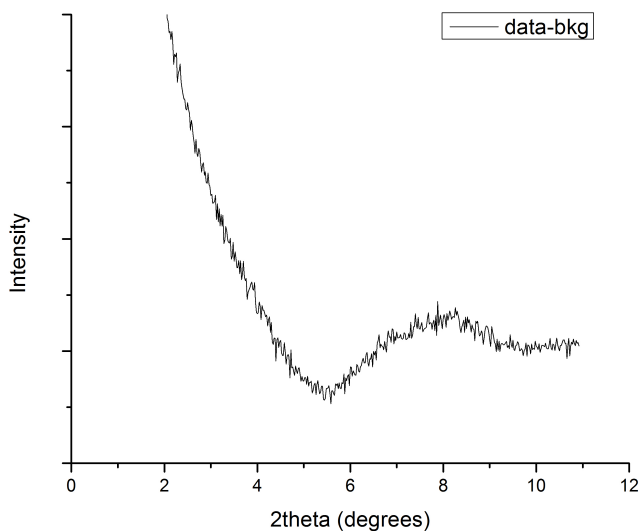


Figure 32: raw data from Figure 31 after background data is removed.

This curve still contains some data from the direct beam. This number decreases along a Gaussian curve as  $2\theta$  increases. To remove the data from this direct beam, we mask out the area where we expect to find our significant data, leaving a small amount of data at low and high angle values with which we can fit a Gaussian curve, as shown in Figure 33. Sometimes it is necessary to remove a second Gaussian curve that results from the side-by-side close packing of the molecules within a smectic layer. This signal is greatly disordered and centered well above our scanning range, but the peak is so broad that it contributes a signal to the high  $q$  end of our data. This is essentially a secondary sample background that sometimes (but not always) contributes enough signal to be visible in the data.

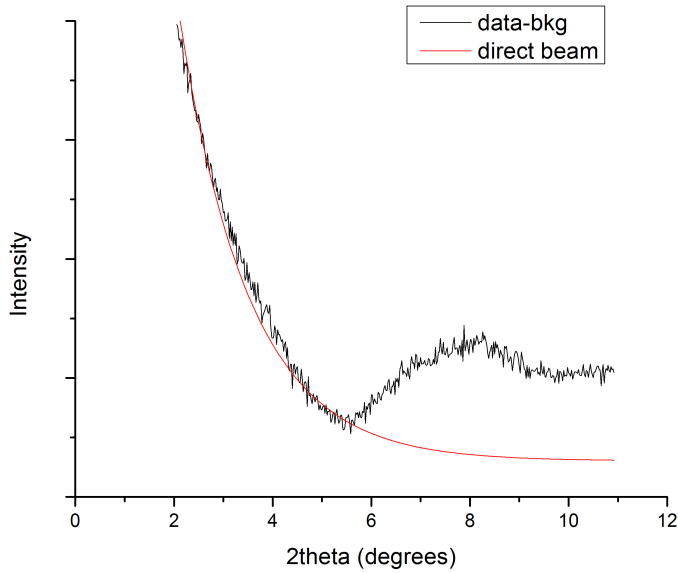


Figure 33: Gaussian curve from the direct beam shown in red.

Subtracting this Gaussian then leaves us with photons scattering directly off our sample. This remaining curve is a combination of several peaks that are quite wide compared to the narrow, sharp peaks found in scans of crystalline samples. This is typical of liquid crystal materials, which have significantly less order than fully crystalline materials, and thus, the repeating spacing that causes the diffraction will vary across the sample.[11, 12, 40, 53] In Figure 34 we see the Gaussian curves that fit this data.

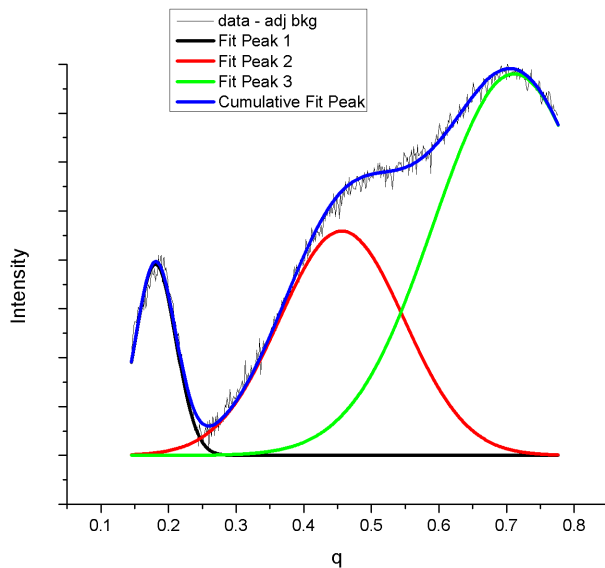


Figure 34: Direct beam data removed; three Gaussian curves fit to remaining data.

These samples are primarily disordered; comprised of small, short-range crystals. With so few crystalline layers, the Taylor series that would model this crystal can be approximated instead as a Gaussian.[76] That is why we fit Gaussian curves whenever we are measuring smectic layers.[74] If we were investigating the nematic structure a Lorentzian would be more appropriate because the nematic is modeled by a decaying exponential. A decaying exponential is characteristic of an amorphous, non-ordered sample, which describes the nematic phase well. The Fourier transform of this decaying exponential is a Lorentzian, so the Gaussian would not be appropriate for nematic ordering.

The fact that our data more closely fits a Gaussian curve, even above the smectic-nematic transition temperature, confirms that we are obtaining data from the liquid crystal molecules disordered by the nanoparticles, forming smectic layers amongst the nematic bulk.[77] However the weak signals and broad peaks tell us that this smectic ordering is short range and irregularly spaced.[78]

Despite the fact that the data obtained from these samples is relatively broad and disordered, we are able to fit the data using only three or four Gaussian curves. We fit the data using as few curves as is possible in order to accurately represent the structures that were responsible for causing them. Using too few curves would result in unacceptably high error, while using too many would dilute the usefulness of the data. While it is possible to fit nearly any data set if you use enough curves, analyzing those curves and tracking trends would be impractical and very difficult.

The peaks centered around  $q=0.2$ ,  $0.45$ , and  $0.7 \text{ \AA}^{-1}$  correspond to spacing of  $31.42 \text{ \AA}$ ,  $14.96 \text{ \AA}$ , and  $8.97 \text{ \AA}$  respectively.[53] A single 8CB molecule is approximately

22.5 Å long, but a pair of 8CB molecules interdigitates to form a “rod” that is about 31.5 Å long [40] (see Figure 35).

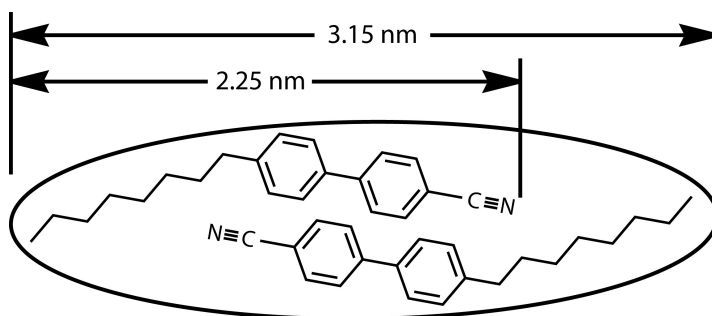


Figure 35: Two 8CB molecules interdigitate to form a “rod” approximately 31.5 Å long with hydrophobic ends and a hydrophilic middle.

This tells us that nearly perpendicular smectic layers are causing the  $q=0.2 \text{ \AA}^{-1}$  peak, so we can calculate that the molecules are leaning at  $4.1^\circ$  from normal by using Formula 2:

$$\cos \varphi = d/L \quad (2)$$

where  $d$  is the  $d$ -spacing calculated from the  $q$ -value, and  $L$  is the length of the interdigitated 8CB “rod”; see Figure 36 for the geometry, and Figure 37 for the repetitive spacing that causes this peak (marked “A”). The other two peaks are caused by 8CB smectic layers that aligned with faces of the faceted nanoparticles that were neither perpendicular, nor parallel to the substrate (Figure 37, marked “B”). See page 54 for more details of the faceting.

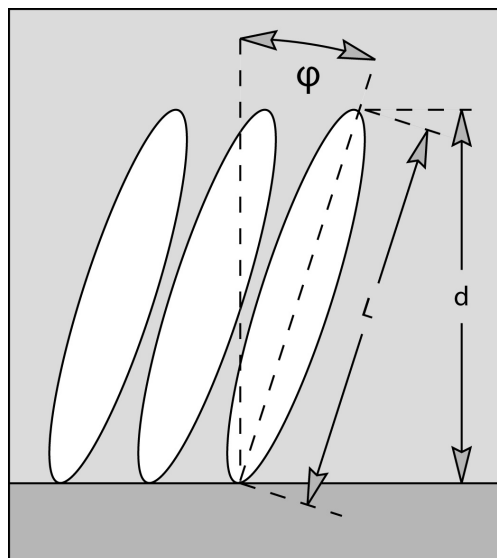


Figure 36: geometry of calculating the tilt of molecules in smectic layers.

The width of each peak gives us an idea of how far the order corresponding to each peak extends throughout the sample. Narrow peaks indicate greater order. The height of the peaks is indicative of the overall ordering as well, but this is mainly a relative assessment, since this depends on the power of the X-ray source, as well as how accurately the beam is aligned. Within a series of scans where the sample, beam, and

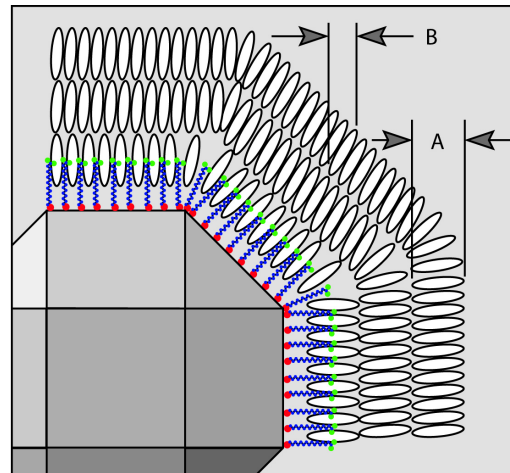


Figure 37: cartoon depicting the different repetitive geometries that produce peaks in X-ray scattering data.

alignment are unchanged, peak heights can be compared qualitatively, but if any of those factors are changed, comparing peak intensity would be speculative at best.

Without removing the sample from the stage, we annealed this sample by raising the temperature to 50°C, which is above the “clearing point” and well into the isotropic phase of 8CB. We lowered the set temperature back to room temperature and allowed the sample to slowly cool on its own, a rate of approximately 1°C per minute. When the temperature stabilized, a second scan was run with the same parameters as the pre-annealing data. After removing the background, as before, we are left with the curves found in Figure 38.

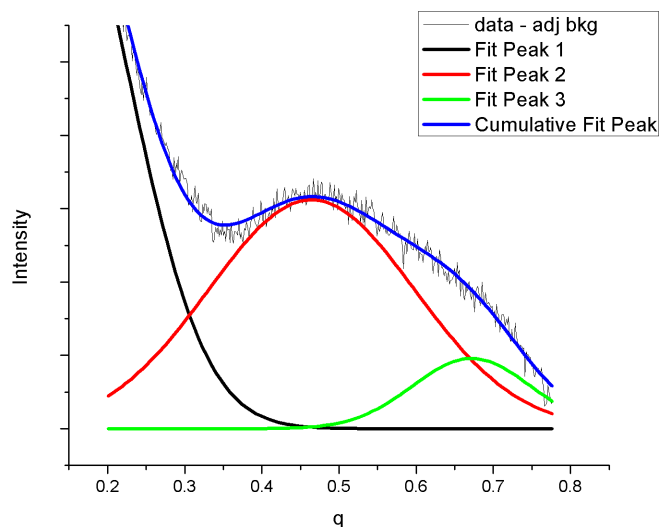


Figure 38: Gaussian curves fit to data from annealed sample (background data removed).

Note that the large peak around  $q=0.7 \text{ \AA}^{-1}$  in Figure 31 nearly disappears after annealing, while the small, neatly ordered peak around  $q=0.2 \text{ \AA}^{-1}$  in Figure 35 grew greatly. Both peaks seem to have shifted to the left slightly as well. The central peak at  $q=0.45 \text{ \AA}^{-1}$  seems only to have broadened. The dramatic growth of the  $q=0.2 \text{ \AA}^{-1}$  peak post-annealing is evidence that depositing the sample disturbs the nanoparticles, and annealing allows the particles to realign and form smectic layers in an orientation needed for Bragg diffraction. The peak center shifting to lower  $q$  values indicates that the d-spacing of the smectic layers is larger than pre-annealing, so the molecules have decreased their tilt angle to closer to normal with respect to the layer planes.

Only those layers that are perpendicular to the substrate will cause the constructive interference that is detected in the experiment due to the orientation of the X-rays. The smectic layers of 8CB naturally align parallel to the substrate, but they also align tangential to the surface of some coated nanoparticles and normal to the surface of others. In three dimensions, some of the smectic layers surrounding these nanoparticles will be properly oriented to diffract X-rays. The X-rays that are scattered by the in-plane

8CB molecules will amount to a very broad, very shallow signal that does not contribute significantly to the data we collect.

Figure 39 shows the data with all background information removed when the annealed sample temperature is raised to  $30.17^{\circ}\text{C}$  ( $\pm 0.056^{\circ}\text{C}$ ), still in the smectic-A phase and below the nematic transition temperature of  $30.39^{\circ}\text{C}$  ( $\pm 0.056^{\circ}\text{C}$ ; as found by PO microscopy for this sample).

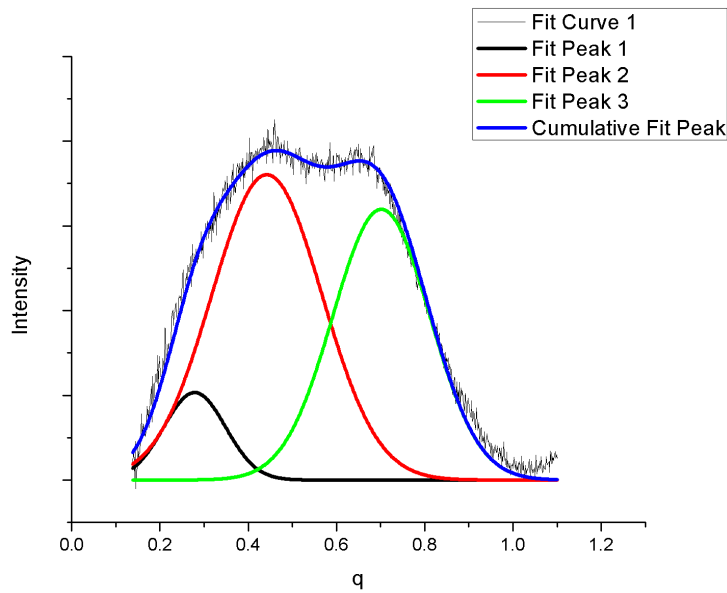


Figure 39: annealed sample raised to  $30.17^{\circ}\text{C}$  ( $\pm 0.056^{\circ}\text{C}$ ), still in the smectic-A phase.

Here, the peaks around  $q=0.4 \text{ \AA}^{-1}$  and  $q=0.7 \text{ \AA}^{-1}$  are dominant, while the  $q=0.2 \text{ \AA}^{-1}$  peak is considerably smaller than in the annealed room temperature data. This suggests that there is less order amongst smectic layers as the sample approaches the transition temperature, and the lateral ordering is increasing.

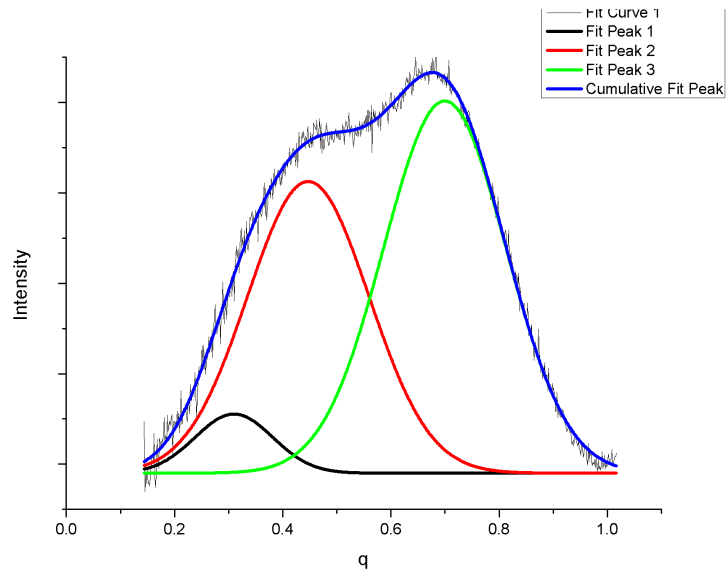


Figure 40: annealed sample raised to 30.28°C ( $\pm 0.056^\circ\text{C}$ ), which is still in the smectic-A phase.

Figure 40 shows the amplitude of the peak around  $q=0.7 \text{ \AA}^{-1}$  increasing as the temperature is increased to  $30.28^\circ\text{C}$  ( $\pm 0.056^\circ\text{C}$ ), which is still in the smectic-A phase, just below the transition temperature of  $30.39^\circ\text{C}$  as found by PO microscopy (see Table II).

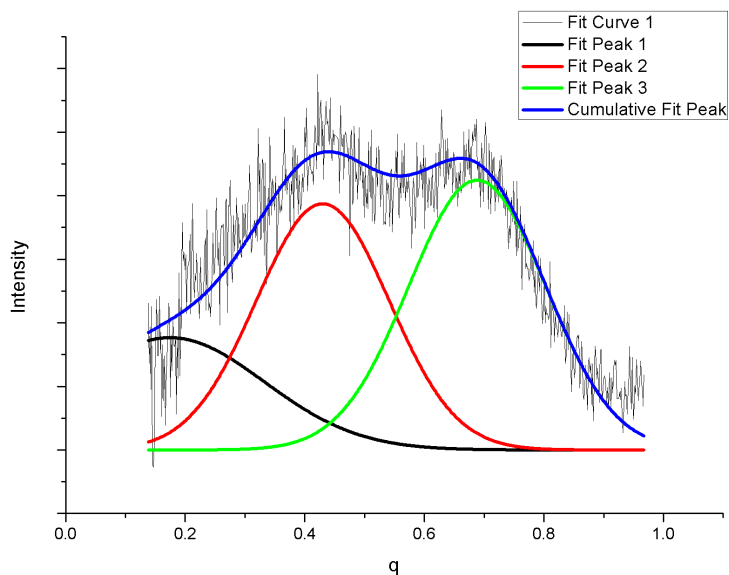


Figure 41: annealed sample at 30.39°C ( $\pm 0.056^\circ\text{C}$ ), the SmA-N transition temperature.

Figure 41 shows both the peaks around  $q=0.4 \text{ \AA}^{-1}$  and  $q=0.7 \text{ \AA}^{-1}$  dropping once the sample reaches  $30.39^\circ\text{C}$  ( $\pm 0.056^\circ\text{C}$ ), the SmA-N transition temperature as determined via PO microscopy. The intensity of the signal drops as we reach the transition temperature. Disorder in the sample due to molecules shifting from smectic layers to the less ordered nematic results in less constructive interference.

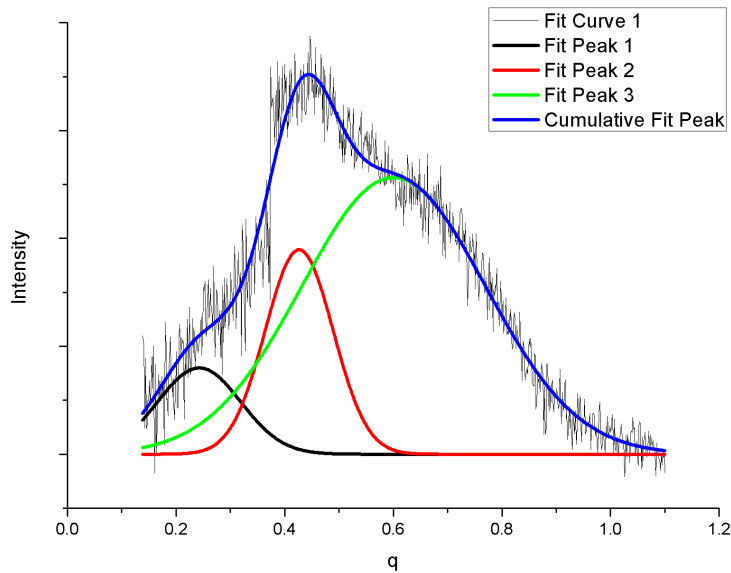


Figure 42: annealed sample at 30.61°C ( $\pm 0.056^\circ\text{C}$ ) in the nematic phase.

Figure 42 shows the result of a scan at  $30.61^\circ\text{C}$  ( $\pm 0.056^\circ\text{C}$ ); the curves fit to this data show a (relatively) tightly packed  $q=0.4 \text{ \AA}^{-1}$  peak, but a very broad peak that has shifted further left to  $q=0.6 \text{ \AA}^{-1}$  as we passed the transition point into the nematic phase. The sudden jump at  $q=0.4 \text{ \AA}^{-1}$  is peculiar, and should be compared to more detailed MDHA results in the next section. The peak around  $q=0.6 \text{ \AA}^{-1}$  has broadened, so the correlation length is much shorter in the nematic phase. This makes sense given that the only smectic layers still present will be those very close to the nanoparticles.

Despite the fact that the data obtained from these samples is relatively broad and disordered, we are able to fit the data using only three or four Gaussian curves. We fit the data using as few curves as is possible in order to accurately represent the structures that were responsible for causing them. Using too few curves would result in unacceptably high error, while using too many would dilute the effectiveness of the data. While it is possible to fit nearly any data set if you use enough curves, analyzing those curves and tracking trends would be unphysical.

The FeCo nanoparticles were synthesized using a polyol process whereby metal precursor salts are dissolved in glycol, heated to its boiling point (roughly 200°C). The mixture was heated to the reflux point, so it was boiling at constant volume, for two hours. The compounds go through complicated intermediate phases, and then combine to form FeCo.[79, 80] At the times and temperatures used, this process produces nanoparticles 2nm in diameter. The nanoparticles experience minimal oxidation unless exposed to temperatures exceeding 350° C.[81]

Our FeCo nanoparticles have a body centered cubic (BCC) crystalline structure[82, 83] that gives the nanostructures a rhombicuboctahedron shape. The rhombicuboctahedron can be imagined as a cube that has had all twelve edges cut away at 45° angles, and its eight corners cut away to make equilateral triangular faces (see Figure 43).

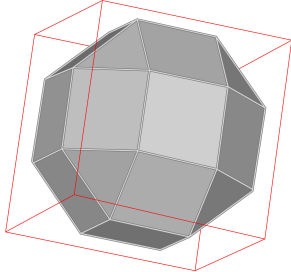


Figure 43: Rhombicuboctahedron faceted nanoparticle.

We will refer to the remaining portions of the original cube (found in the (100), (010), and (001) planes, shown in red in Figure 44) as the “cubic faces”, the faces formed by cutting away the edges (found in the (110),  $(1\bar{1}0)$ , (101),  $(10\bar{1})$ ,  $(0\bar{1}\bar{1})$ , and (011) planes, shown in blue in Figure 44) as the “edge faces”, and the triangular faces (found in the (111),  $(11\bar{1})$ ,  $(1\bar{1}1)$ , and  $(\bar{1}11)$  planes, shown in green in Figure 44) as the “corner faces”.[83]

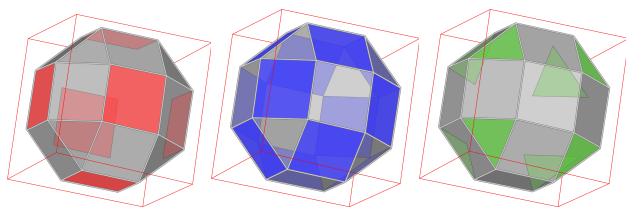


Figure 44: Cubic faces in red, edge faces in blue, corner faces in green.

The interior angles formed between the cubic faces (red) and the edge faces (blue) measures  $135^\circ$ , between the edge faces (blue) and the corner faces (green) measures  $145.7^\circ$ , and between the cubic faces (red) and the corner faces (green) measures  $114.1^\circ$ . In the case of MHDA and PEG, the molecules protrude out from the surface, normal to their facet.

We believe the faceted surfaces of the nanoparticles provide a structure on which smectic layers form in the vicinity of the functionalized nanoparticle. The layers may form parallel to the nearest facet, at angles to neighboring smectic regions with a defect in between. The liquid crystals will still possess a tilt angle within their smectic layer, but not necessarily the same tilt angle from one “grain” to another. The term “grain” is much better suited to crystalline materials than soft liquid crystals, but it is used here to refer to the short-range ordered section of the liquid crystal system. While the tilt angle will change according to temperature fluctuations, those changes occur in lock step. In other words, the difference in the tilt angles (from one grain to another) stays the same independent of temperature. This difference is possibly due to the faceted structure of the nanoparticles.

We believe 8CB molecules in the presence of these faceted nanoparticles may align with each face according to the properties of the functionalization compound. MHDA has been found to orient the 8CB molecules normal to the surface of the nanoparticle. With the 8CB molecules aligning to the faces, the smectic layers they form will meet at the same angles of the faces listed above. These angular differences are large

enough that they will form disclinations or defects where the different layers meet. This means that the smectic layers aligning with a cubic face will meet the layers of an edge face at a  $135^\circ$  angle. The disclinations seen in smectic layers (bend, twist, and splay, see Figure 18) determine how these layers distort to meet the surrounding bulk ordered liquid crystals.[68]

Our X-ray scattering data has quantized peaks centered on specific q-values, indicating preferred tilt angles, which we believe is a consequence of the faceted structure of the nanoparticles. If our nanoparticles were perfectly round, the scattering data would consist of one extremely broad peak, covering all tilt angles from  $0^\circ$  to  $90^\circ$ . The fact that we do see these quantized peaks also means these samples have minimal agglomeration of nanoparticles.[84] Misshapen or agglomerated particles would provide additional tilt angle data that would obscure the peaks we do see in our scattering results. The particles are not perfect, and neither is the liquid crystal ordering that takes place in their vicinity, so the data is consistent with a mostly disordered material. In addition, we see this structure because the nanoparticles and the dislocations or defects they form align (see Figure 30).

We expect the tilt angle of the 8CB with respect to its smectic layers (and by extension, the facet to which it is aligned) to be consistent from one facet to the next. The lock-step movement of the peak centers in our MHDA experiment supports this theory. We can determine the tilt angle from the different faces by calculating the angles of the molecules with respect to the substrate, then subtracting the angle of the facet with respect to the substrate.

We need to find the transition from smectic phase to nematic to determine the behavior as the transition is reached. The transition temperature is dependent upon the

functionalization of the nanoparticles, and these points were determined for each of our mixtures using polarized optical microscopy. The transition temperatures are shown in Table II below.

Table II: Sm-N transition temperatures of X-ray sample.			
Content	100% 8CB	30% MHDA N.P.	30% PEG N.P.
Transition Temp.	33.77° C	30.63° C	30.89° C

## Results

### MHDA

Having completed our preliminary X-ray scattering experiment, we prepared a more extensive investigation of MHDA-coated nanoparticles in 8CB. We deposited a new sample with the same nanoparticle concentration to study over a greater range of temperatures and with greater detail. After annealing the sample, as was done with the preliminary experiment, we scanned the sample starting at room temperature of 26.67°C ( $\pm 0.056^\circ\text{C}$ ) using the same X-ray power (50kV and 100mA) over the angles  $2\theta = 1-17^\circ$ . We ran scans on the sample, raising the temperature in increments of 0.25°C ( $\pm 0.056^\circ\text{C}$ ) up to 29.44°C ( $\pm 0.056^\circ\text{C}$ ), then increments of 0.1°C up to 31.56°C ( $\pm 0.056^\circ\text{C}$ ), well above the transition temperature of 30.39°C, as found by PO microscopy.

The first operation uses the  $q$  value to find the d-spacing of the smectic layers, which is then used to calculate the angle the molecule forms with the substrate. For the layers perpendicular to the substrate, this is also the tilt angle. If the peak resulted from

layers at an angle to the substrate, from aligning with the edge or corner facets, the angle of the facets must be taken into account.

In our MHDA experiments, at 30° C the lowest  $q$  value peak is centered around  $q=0.2 \text{ \AA}^{-1}$ , which gives us a d-spacing of 31.4 Å, so we know these molecules form a 4.7° angle with the substrate. This angle is small enough that we can assume it is the tilt angle of the molecules aligning with the facets that are perpendicular to the substrate.

The next peak is centered around  $q=0.4 \text{ \AA}^{-1}$  from a d-spacing of 15.7 Å. In this case, the molecules are aligned to a facet that is at an angle with the substrate (either a corner facet or an edge facet), so the d-spacing is not the smectic layer spacing, but is the X-component [85] (the beam direction) of the smectic layer spacing. Assuming these molecules are aligned with the edge faces, the 15.7 Å measurement tells us these molecules form a 60.1° angle with the substrate, but the tilt angle with respect to the nanoparticle facet is  $60.1^\circ - 45^\circ = 15.1^\circ$ .

The 10.4° difference between the tilt angle of the cubic facet 8CB molecules and the edge facet 8CB molecules is most likely due to the interaction with the bulk 8CB smectic layers. By increasing the tilt angle on the edge facet 8CB molecules, the system lessens the severity of the defects where the angled smectic layers meet the bulk smectic layers, resulting in a lower energy system. Also lessening the energy of this system is the fact that the primary distortion for that interface is splay, a low-energy distortion.

The next peak of the MHDA experiment is centered around  $q=0.65$  with a d-spacing of 9.6 Å. These molecules form a 72.2° angle with the substrate. The final peak, centered around  $q=0.9$  gives a d-spacing of 7.0 Å. These molecules have a 77.2° angle with the substrate. These two measurements are close enough that we expect the molecules aligning with the corner faces of the nanoparticle cause them both. We would

expect the angle formed between a corner face 8CB molecule and the substrate would be  $65.9^\circ$ , so it appears that these molecules are also influenced by the surrounding bulk. The fact that we see two independent peaks suggests that some corner faces have a tilt angle of  $6.3^\circ$ , while others have a tilt angle of  $11.3^\circ$ . This could be due to the fact that the molecules of neighboring “grains” are oriented at slightly different angles. In an effort to minimize the interfacial energy (the defects), these corner molecules may tilt more or less depending on the tilt angle of the molecules in the neighboring “grain”.

It is important to mention that while the MHDA experiment resulted in four peaks for most temperatures, the data from the PEG experiment was easily fit with only three. The low  $q$  peak around  $q=0.2$  is not present in the PEG data. We attributed the low- $q$  peak in the MHDA experiment to the 8CB molecules aligning with the cubic faces of the nanoparticles. This configuration requires high-energy defects caused by bend and twist distortions as those aligned smectic layers interface with the bulk smectic layers. The smectic layers aligned with corner faces and the upper and lower edge faces, on the other hand, would only require a splay distortion to blend into surrounding smectic layers. Splay is a low energy distortion, thus these layers would be preferential to the high-energy bend and twist layers.

With the short, stiff MHDA molecules coating a nanoparticle, the

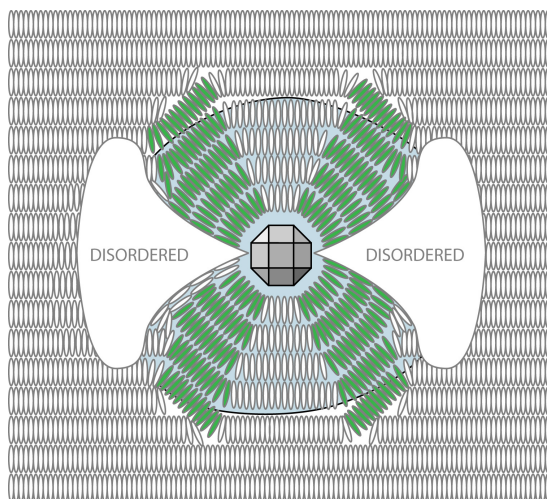


Figure 45: PEG-coated nanoparticle with 8CB rods forming “grains” aligned to facets. Lower energy edge grains highlighted. Horizontal cubic face grains preferentially disorder to lower the energy of the system.

nearest 8CB molecules would be held rigidly in place, creating a structure where the cubic face smectic layers can form. PEG is a long, flexible molecule that extends a great distance from the surface of the nanoparticle. This would allow minimizing the size of the high energy cubic face “grains”, enlarging the lower energy edge and corner “grains”. By aiding in the distortion of the aligned smectic layers, the PEG molecules make the high-energy cubic face alignment unnecessary, leading to areas of disordered 8CB (see Figure 45). This is why we do not see a low  $q$  peak in our PEG data.

Starting at near room temperature of  $26.67^{\circ}\text{C}$  ( $\pm 0.056^{\circ}\text{C}$ ), we obtained the scan data found in Figure 46. This was a newly mixed sample and did not come from the same batch. Consequently, these curves are quite different from those in the preliminary experiment at this same temperature with the same functionalization compound. The peak near  $q=0.65\text{\AA}^{-1}$  is dominant, though quite broad. We have a clear peak around  $q=0.4\text{\AA}^{-1}$  describing the plane-to-plane order, and a subtle peak near  $q=1.0\text{\AA}^{-1}$  that was not present in the previous scans. That position corresponds to a layer spacing of  $d=6.28\text{\AA}$ , which is roughly the width of an 8CB “rod”.

We raised the temperature of the sample stage, taking scans at regular increments. For the sake of brevity, this data will be summarized later. As the temperature is raised from ambient room temperature in the Smectic-A phase, the peak previously around  $q=0.4\text{\AA}^{-1}$  shifts down to around to  $q=0.25\text{\AA}^{-1}$  for several degrees C, then at about  $29.5^{\circ}\text{C}$  peaks are present both at  $q=0.2\text{\AA}^{-1}$  and  $q=0.4\text{\AA}^{-1}$  (see Figure 47 at  $30.00^{\circ}\text{C}$ ). Since these peaks correspond to plane spacing of  $31.4\text{\AA}$  and  $15.7\text{\AA}$ , this could mean there are two separate smectic structures occurring. The first (with spacing of  $31.4\text{\AA}$ ) would have liquid crystal rods standing almost normal to the smectic planes, and parallel to the substrate. The second ( $15.7\text{\AA}$  spacing) would have liquid crystal rods lying

60.1° from the vertical. The  $q=0.7\text{\AA}^{-1}$  peak is still prominent, but slightly narrower. The  $q=1.0\text{\AA}^{-1}$  peak is now taller and more significant.

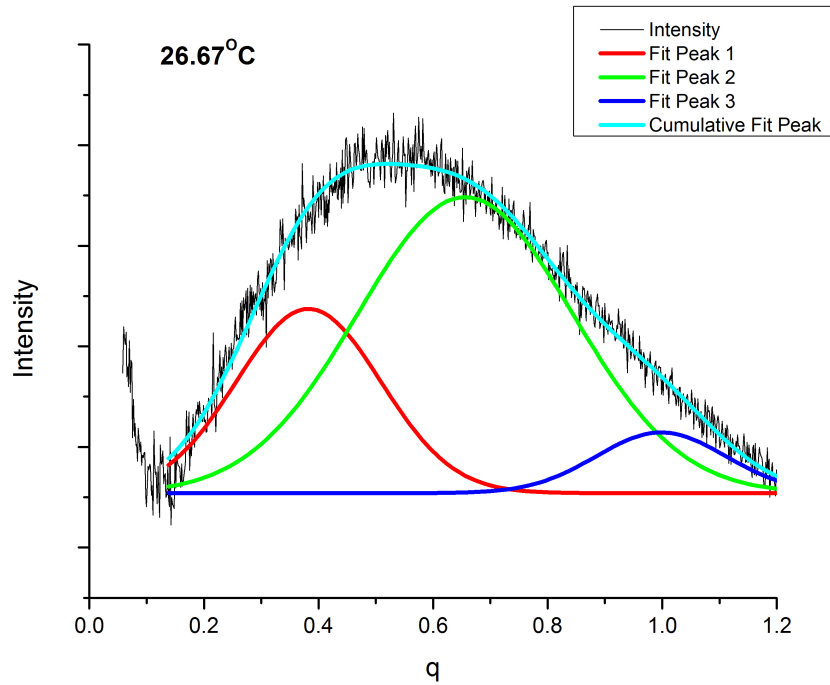


Figure 46: Temperature 26.67° C  $\pm$ 0.056°C, smectic phase.

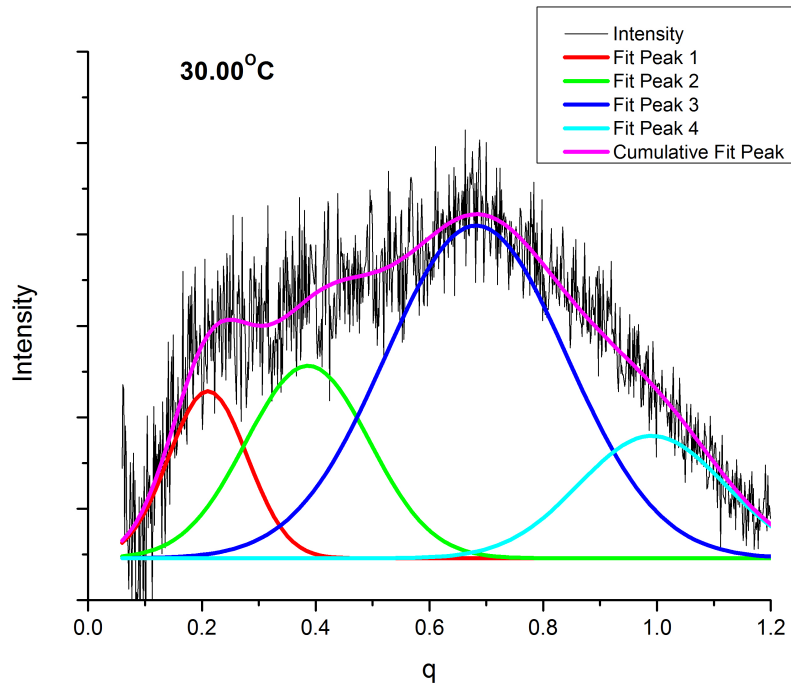


Figure 47: Temperature 30.00° C  $\pm$ 0.056°C, smectic phase.

We see that the  $q=0.7\text{\AA}^{-1}$  peak shrinks and shifts to slightly lower  $q$ -value, and the  $q=0.2\text{\AA}^{-1}$  peak grows taller than the  $q=0.4\text{\AA}^{-1}$  peak when we reach the Sm-N transition temperature (see Figure 48). The high  $q$  peak has shifted slightly to the left and broadened a bit as evidence of disordering during transition. The decrease of the  $q=0.7\text{\AA}^{-1}$  peak's intensity suggests that during transition, the rearranging of molecules from smectic layers to a nematic structure happens chaotically, with much less consistency in the molecule-to-molecule spacing.

When we surpass the transition temperature and continue into the nematic (as seen in Figure 49), the peak near  $q=0.2\text{\AA}^{-1}$  has shifted up to nearly  $q=0.3\text{\AA}^{-1}$  and continues to grow more intense, becoming the dominant peak of this curve, while the peak near  $q=0.7\text{\AA}^{-1}$  narrows further. The growth of the  $q=0.3\text{\AA}^{-1}$  peak is interesting, as it indicates that we have greater smectic layer formation (in proximity to the nanoparticles) when in the nematic phase than we did in the smectic phase. This supports the assertion that liquid crystals are free to reorient within limits and/or that the nanoparticles rotate as the temperature changes.[86]

The smectic layers around the nanoparticles, and the liquid crystal molecules uninfluenced by the presence of the nanoparticles meet these layers at odd angles, forming a disclination (see Chapter 5). When the phase of the bulk changes from smectic to nematic, the order of those smectic layers dissolves into simple directional order. The molecules are more freely able to align with the smectic layers surrounding the nanoparticles when there is less order in the surrounding nematic bulk.

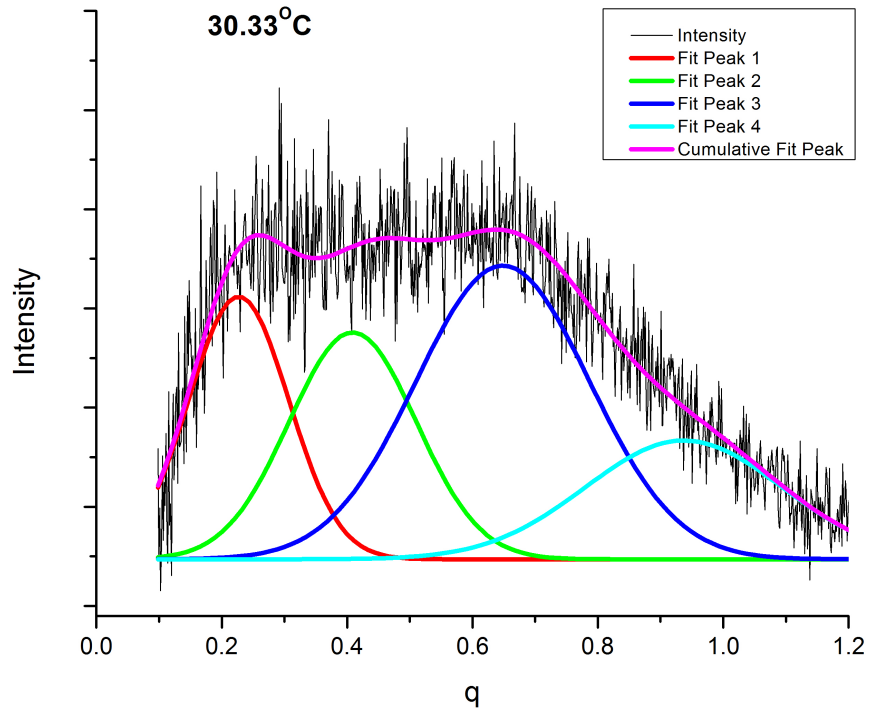


Figure 48: Temperature 30.33° C  $\pm$ 0.056°C, Sm-N transition.

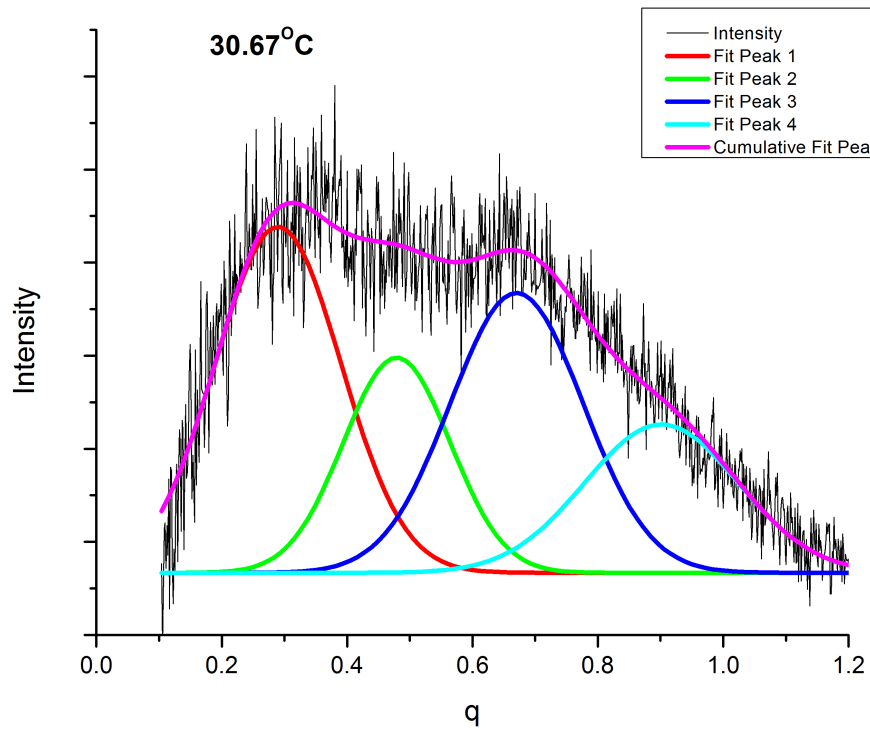


Figure 49: Temperature 30.67° C  $\pm$ 0.056°C, nematic phase.

Further into the nematic, this effect lessens, as shown in Figure 50, but there is still a substantial amount of smectic layer ordering present, giving us the peaks at  $q=0.25\text{\AA}^{-1}$  and  $q=0.45\text{\AA}^{-1}$ . The three main peaks have evened out to being almost equal, while the smaller peak near  $q=0.9\text{\AA}^{-1}$  appears nearly unchanged since the transition.

The data in Figure 50 is considerably different from that found in our preliminary experiments at similar temperatures. It seems that the peculiar jump in intensity seen in Figure 42 was an anomaly that was not repeated. In fact, none of the peaks in Figure 42 resemble those from Figure 50. Disagreements between preliminary data and this more detailed experiment are attributed to using different samples (of the same compounds). Errors that occurred during experiments were always recorded and scans repeated if necessary.

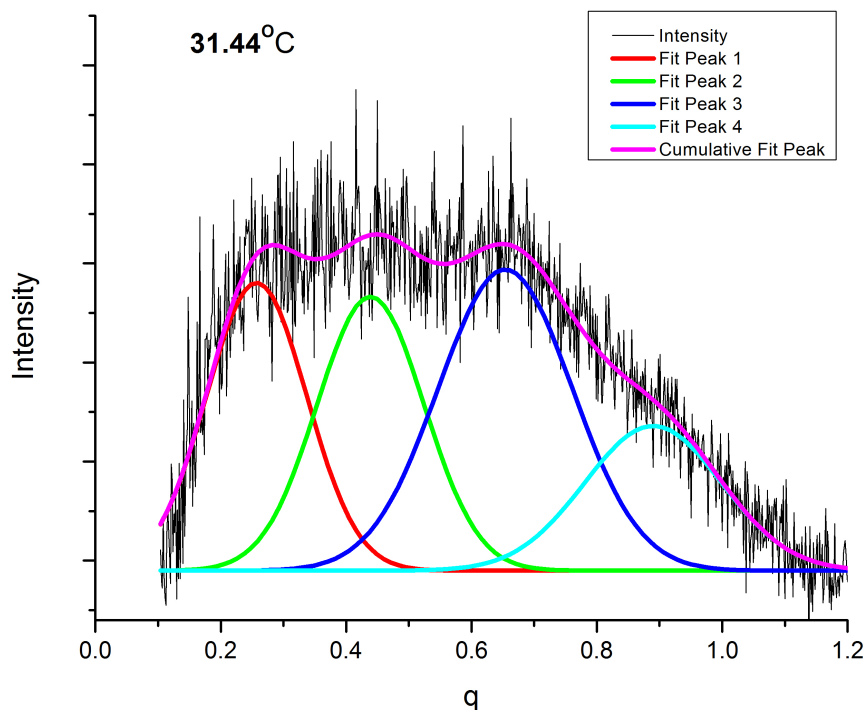


Figure 50: Temperature  $31.44^\circ\text{C} \pm 0.056^\circ\text{C}$ , nematic phase.

Figure 51 shows a summary of the movement of the low  $q$  peak that appeared halfway through the experiment around 29.7°C. With a low  $q$  of 0.18Å<sup>-1</sup> and a high of 0.29Å<sup>-1</sup>, this layer spacing ranges from  $d=34.9\text{Å}$  to 21.7Å, with the largest jump at the transition temperature (indicated by the blue line), going from  $d=31.1\text{Å}$  at 30.56°C to  $d=21.7\text{Å}$  at 30.67°C. After an initially stable climb in  $q$  position, the values change more drastically around the transition temperature and into the nematic phase.

The other low  $q$  peak (labeled “Peak 2” in the legend of Figures 50 and 51), whose varying  $q$  values are seen in Figure 52, was present throughout the experiment starting at room temperature. The movement of this peak is quite dramatic, beginning around  $q=0.38\text{Å}^{-1}$ , dropping as low as  $q=0.22\text{Å}^{-1}$ , and rising as high as  $q=0.48\text{Å}^{-1}$  in the nematic phase. This translates to  $d$ -spacings of 16.53Å at room temperature, a minimum of 13.09Å at the transition temperature, and a maximum of 28.56Å at several points between 27.5°C and 29.6°C. So the molecules forming this smectic layer were tilted anywhere from 24.95° from vertical (at the maximum layer separation) to 65.44° from vertical (at the minimum layer separation).

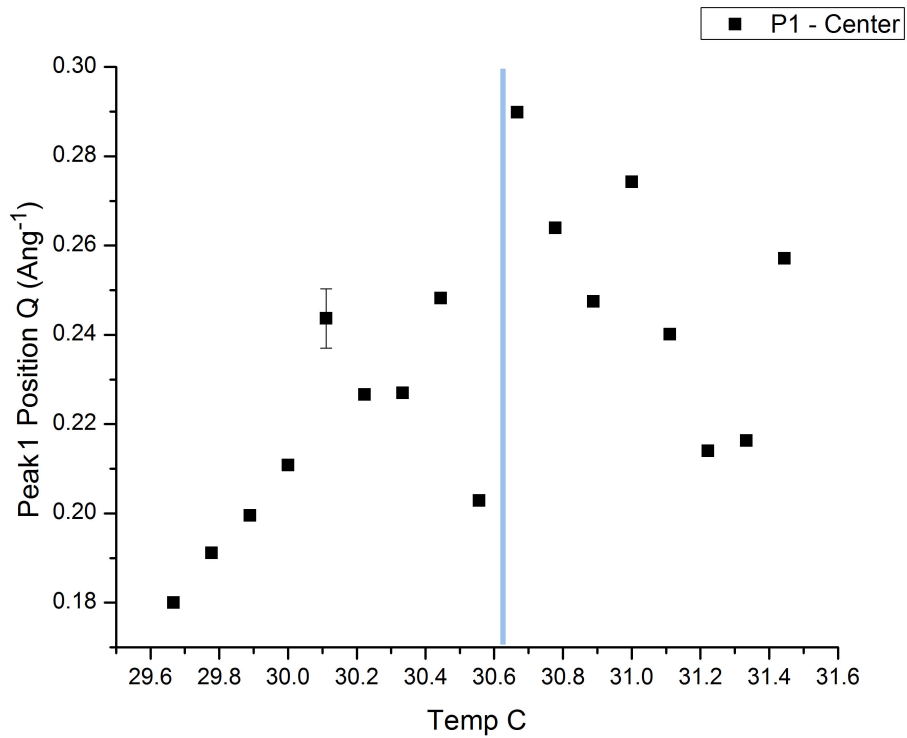


Figure 51a: Position of low q peak (Peak 1); Temperature  $\pm 0.056^{\circ}\text{C}$ ; error shown applies to all data points.

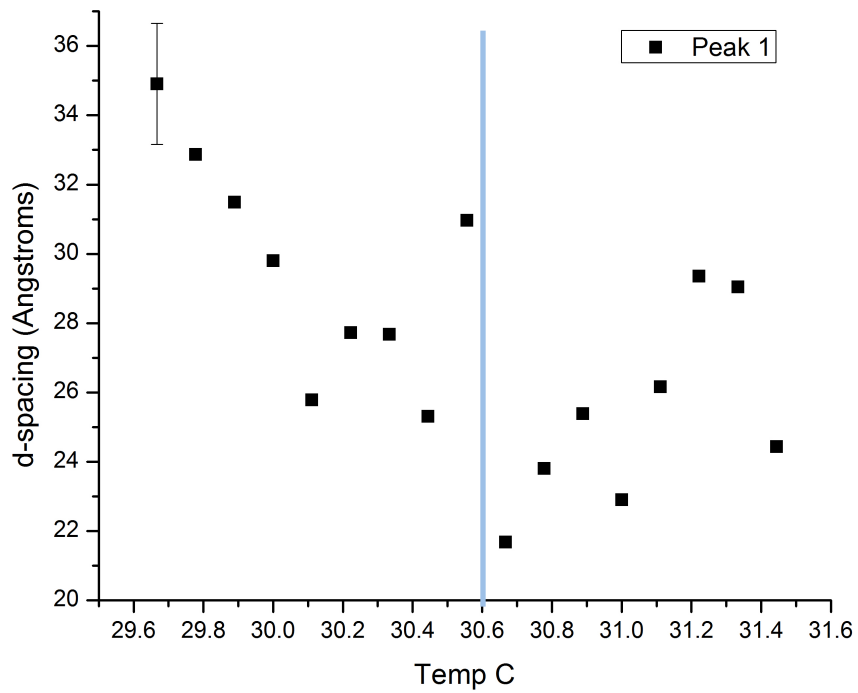


Figure 51b: d-spacing of low q peak (Peak 1) vs. Temperature; Temperature  $\pm 0.056^{\circ}\text{C}$ ; error shown applies to all data points.

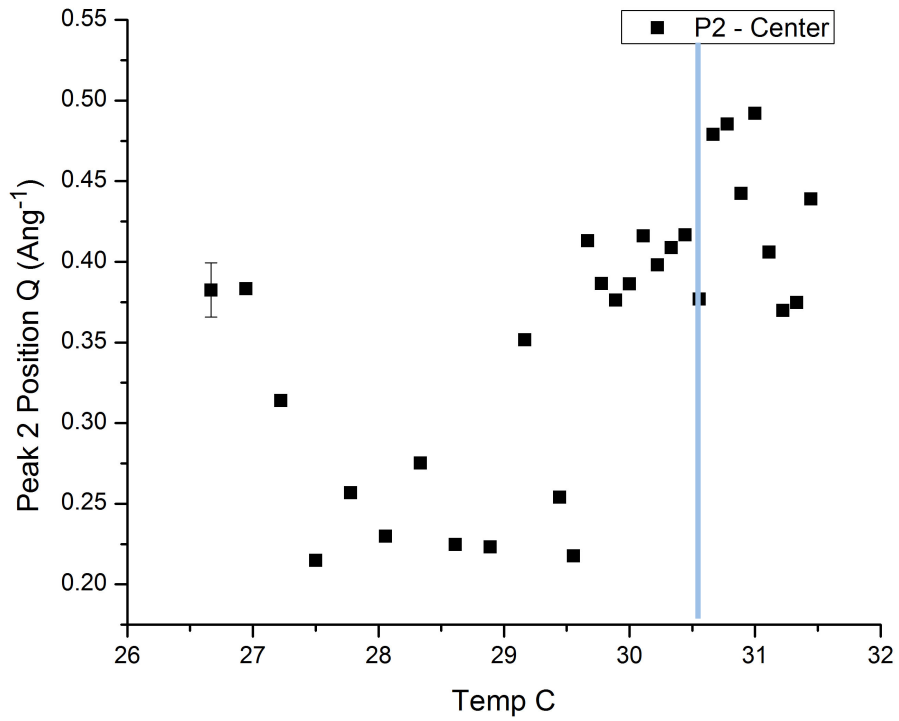


Figure 52a: Position of low q peak (Peak 2); Temperature  $\pm 0.056^\circ\text{C}$ ; error shown applies to all data points.

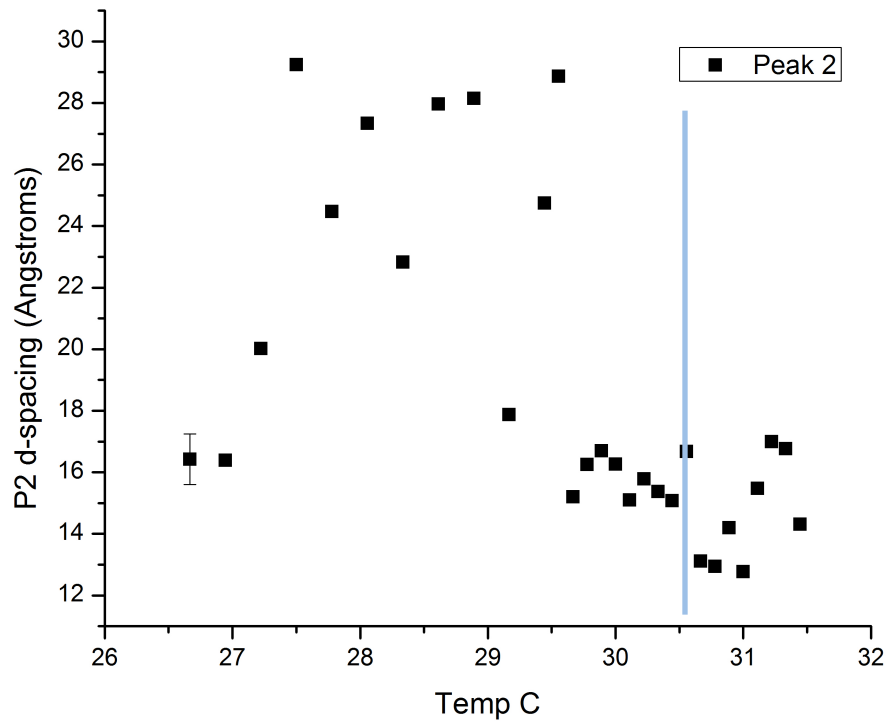


Figure 52b: d-spacing of low q peak (Peak 2) vs. Temperature; Temperature  $\pm 0.056^\circ\text{C}$ ; error shown applies to all data points.

The summary of the  $q$  values of peak 3 (see Figure 53) shows us that this peak moves quite a bit between room temperature and the transition temperature, dropping significantly for more than  $1^\circ\text{C}$  before returning to its original position when approaching the nematic phase. This peak is more stable once the sample is nematic.

The high  $q$  peak drops (movement summary seen in Figure 54) between room temperature and the transition point before rising again for the nematic as with the other peaks. The high  $q$  peak translated to d-spacing in this data has a maximum of  $7.95\text{\AA}$  and a minimum of  $6.16\text{\AA}$ .

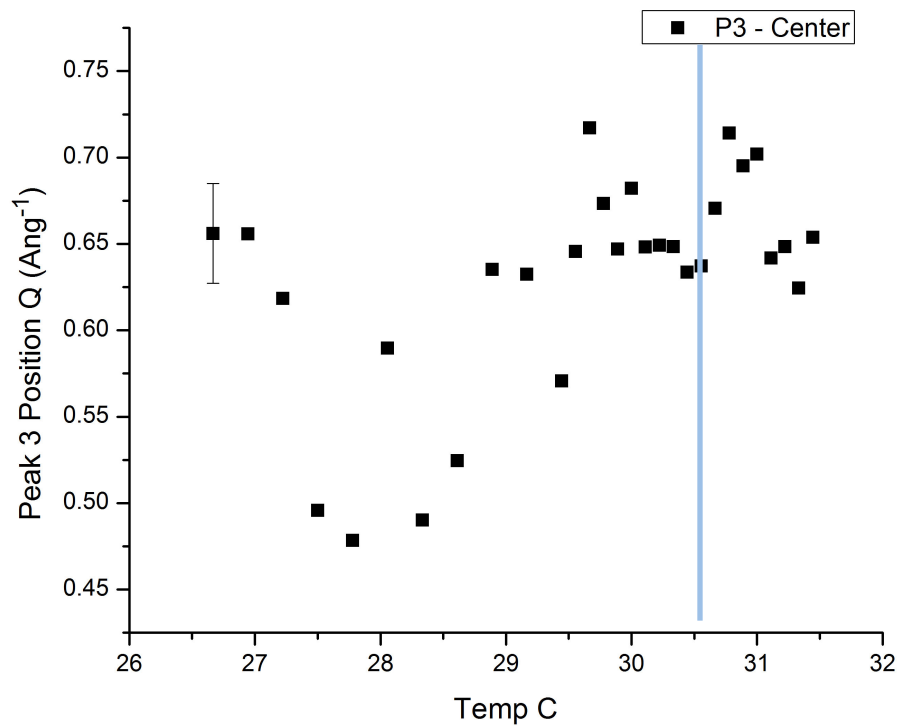


Figure 53a: Position of mid q peak (Peak 3); Temperature  $\pm 0.056^\circ\text{C}$ ; error shown applies to all data points.

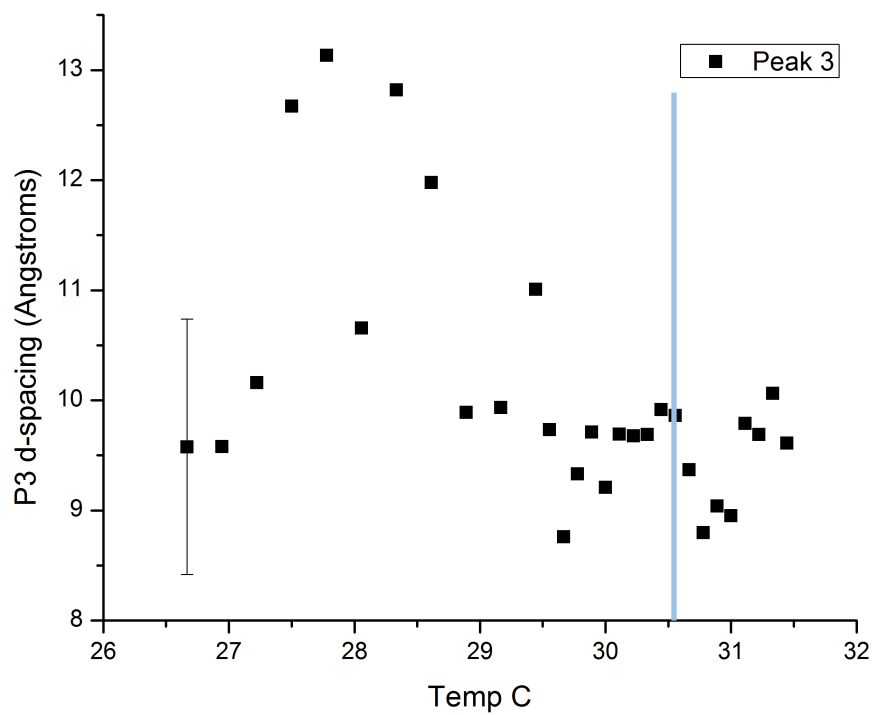


Figure 53b: d-spacing of mid q peak (Peak 3) vs. Temperature; Temperature  $\pm 0.056^\circ\text{C}$ ; error shown applies to all data points.

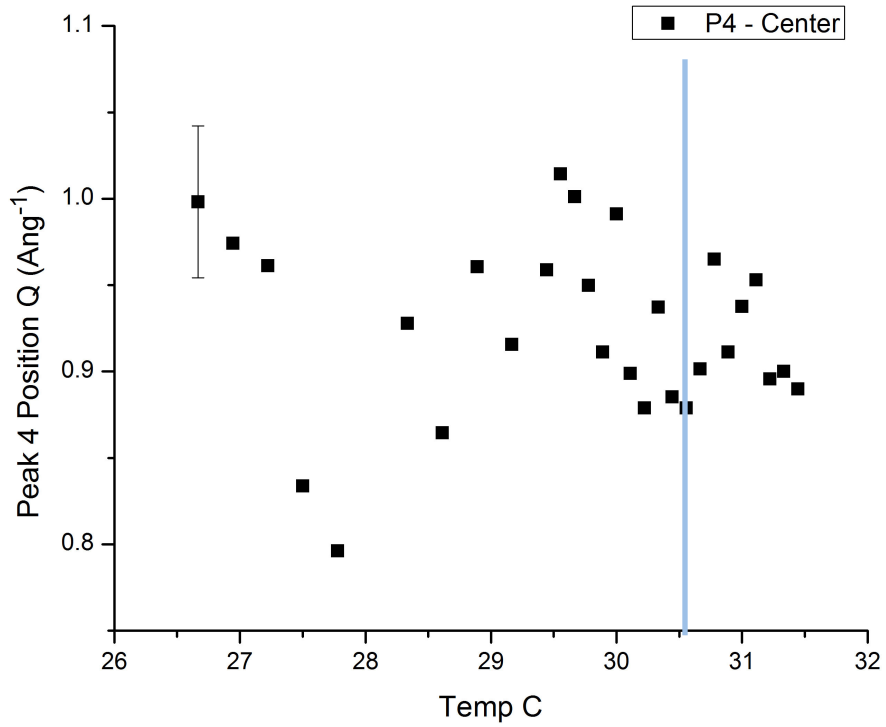


Figure 54a: Position of high q peak (Peak 4); Temperature  $\pm 0.056^\circ\text{C}$ ; error shown applies to all data points.

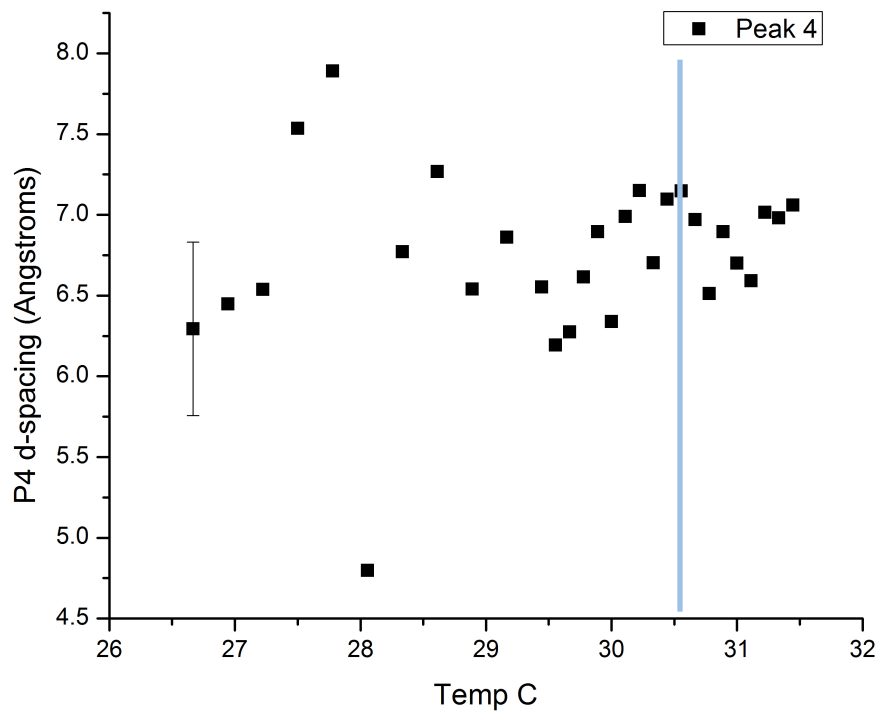


Figure 54b: d-spacing of high q peak (Peak 4) vs. Temperature; Temperature  $\pm 0.056^\circ\text{C}$ ; error shown applies to all data points.

Figure 55 shows the movement of each peak as the temperature rises. There is a noticeable and consistent shift in the peak positions between 27°C and 29°C. While the change is more subtle, there is a small jump or drop in each peak at the smectic-nematic transition temperature of 30.63°C (as found by Cordoyiannis, et al.).[8]

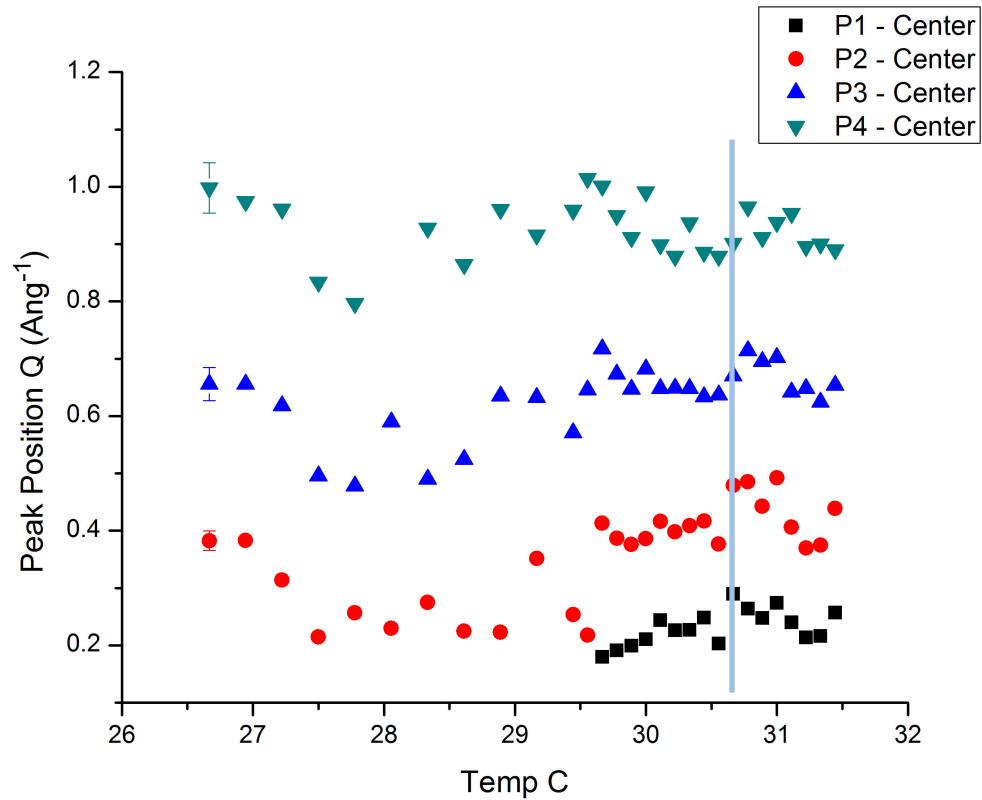


Figure 55a: Summary of peak positions; Temperature  $\pm 0.056^\circ\text{C}$ ; error shown applies to all data points of their respective set.

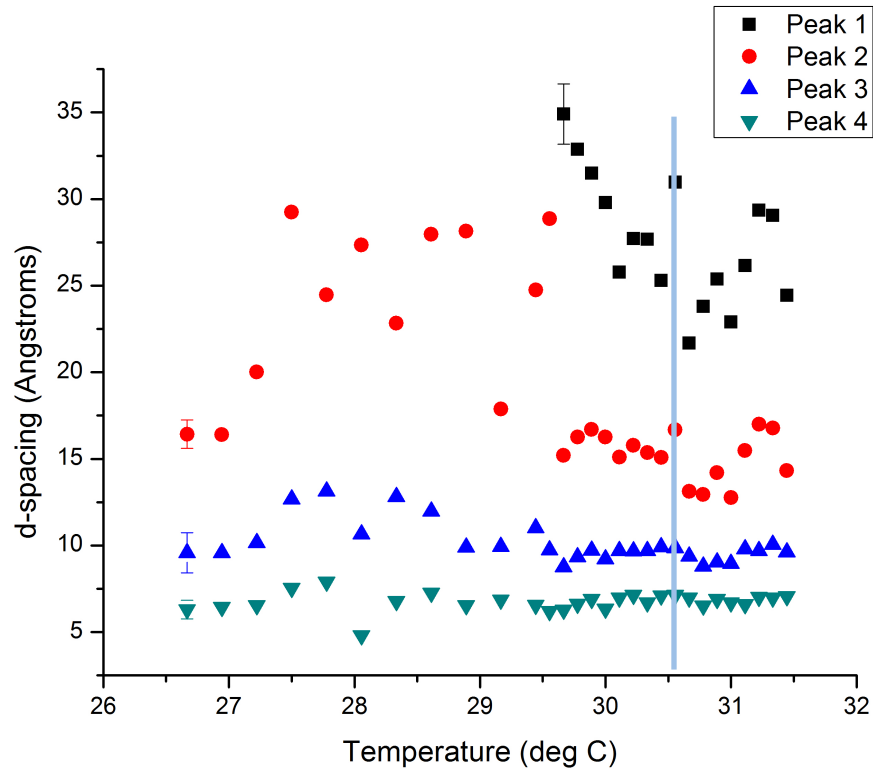


Figure 55b: Summary of MHDA average d-spacings; Temperature  $\pm 0.056^\circ\text{C}$ ; error shown applies to all data points of their respective set.

It is helpful to study the correlation length of these peaks as a way of quantifying the order in the system. The correlation length is found by the equation:

$$\xi = 2\pi / \Delta q \quad (3)$$

where  $\Delta q$  is the full width half maximum of the peak. The correlation length tells us the distance over which the orientational order is consistent.[2] This gives us a way to measure the range of the reorganizational influence the nanoparticle has on the surrounding liquid crystal molecules.

Figure 56 summarizes the correlation length of peak 1 (the low  $q$  value peak that appeared halfway through the experiment) at different temperatures. For this peak, we see a dramatic drop in correlation length at the transition temperature, but the length increases as the temperature continues to rise. We see substantial variation in the

correlation length throughout the experiment, but this variation is much greater in the nematic phase than in the smectic.

The most interesting part of Figure 57, showing the correlation length of peak 2 (the low  $q$  peak describing smectic layer spacing) throughout the experiment, is the extreme jump from the data set's minimum length of  $10\text{\AA}$  to its maximum of about  $47\text{\AA}$  that occurs between  $27.2^\circ\text{C}$  and  $27.4^\circ\text{C}$  ( $\pm 0.056^\circ\text{C}$ ),  $3.2^\circ\text{C}$  below the Sm-N transition temperature. This fluctuation was so extreme, given the rest of the data points were between  $17$  and  $32\text{\AA}$ , it may be an anomaly that would not be present in repeated scans. However, this is the same temperature where the center positions of peaks 2, 3, and 4 all moved to lower  $q$  values. Since the temperature of  $27.4^\circ\text{C}$  ( $\pm 0.056^\circ\text{C}$ ) where this jump occurred is not any known transition temperature, it may be indicative of an as yet unclassified phase transformation in the vicinity of the nanoparticles (as described by the correlation length), or possibly a pre-transitional change.

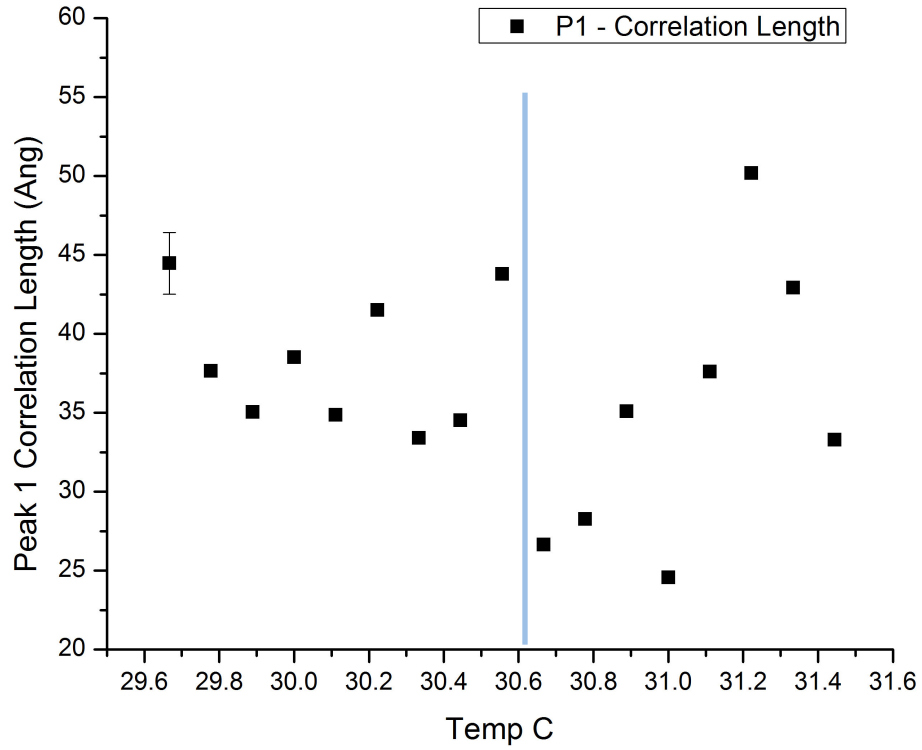


Figure 56: Correlation length of low q peak (Peak 1); Temperature  $\pm 0.056^\circ\text{C}$ ; error shown applies to all data points.

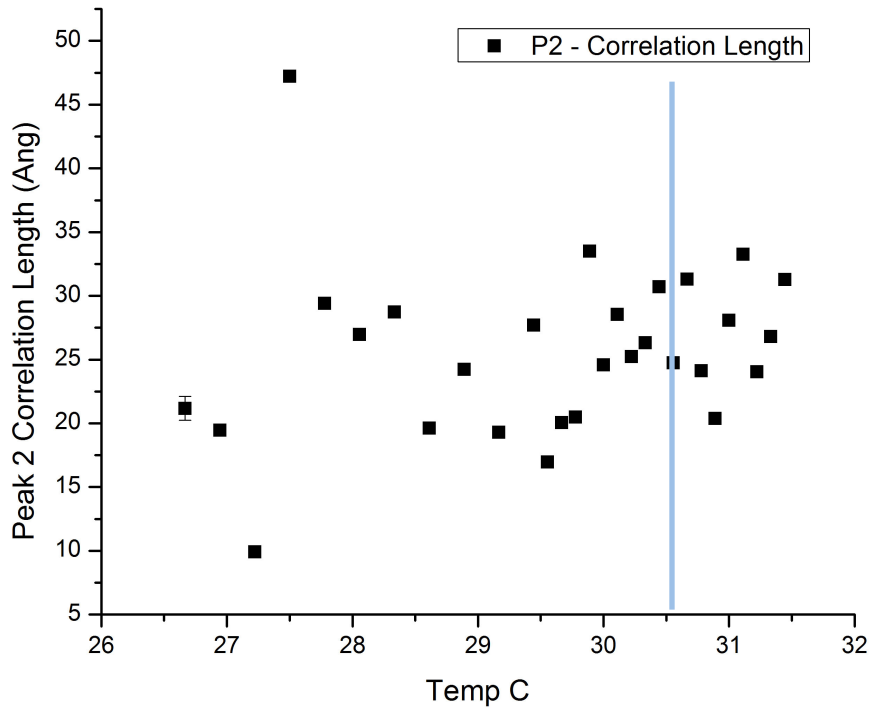


Figure 57: Correlation length of low q peak (Peak 2); Temperature  $\pm 0.056^\circ\text{C}$ ; error shown applies to all data points.

Figure 58 shows the correlation length evolution for the mid-q peak around  $q=0.7\text{\AA}^{-1}$ . The correlation length fluctuates from about  $13\text{\AA}$  up to  $26.5\text{\AA}$ , though these extremes are much less radical than we saw for peak 2. Generally the correlation length is higher and more stable in the nematic phase, above the transition temperature. This tells us that the lateral molecule-to-molecule order in the smectic phase is less stable, and perhaps less dependent on temperature than other influencing factors like interfacial interaction. Again we see the most drastic changes around  $27.5^\circ\text{C}$ , further supporting our suspicions.

Figure 59, displaying the correlation length progression of peak 4 (around  $q=0.9\text{\AA}^{-1}$ ), has a clear drop in correlation length between  $27.8^\circ\text{C}$  and  $28.8^\circ\text{C}$ , but shows little deviation from its upward trajectory across the bulk transition temperature. This would suggest that this spacing, referring to the lateral space between molecules, underwent more of a transition at  $27.8^\circ\text{C}$  than at the bulk transition point of  $30.63^\circ\text{C}$ . [8]

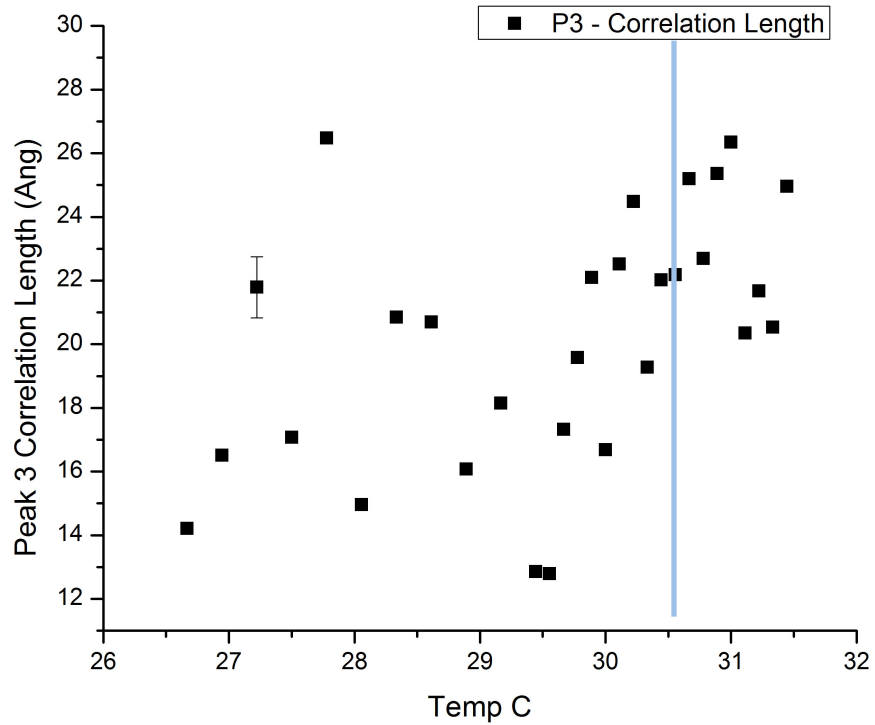


Figure 58: Correlation length of mid q peak (Peak 3); Temperature  $\pm 0.056^\circ\text{C}$ ; error shown applies to all data points.

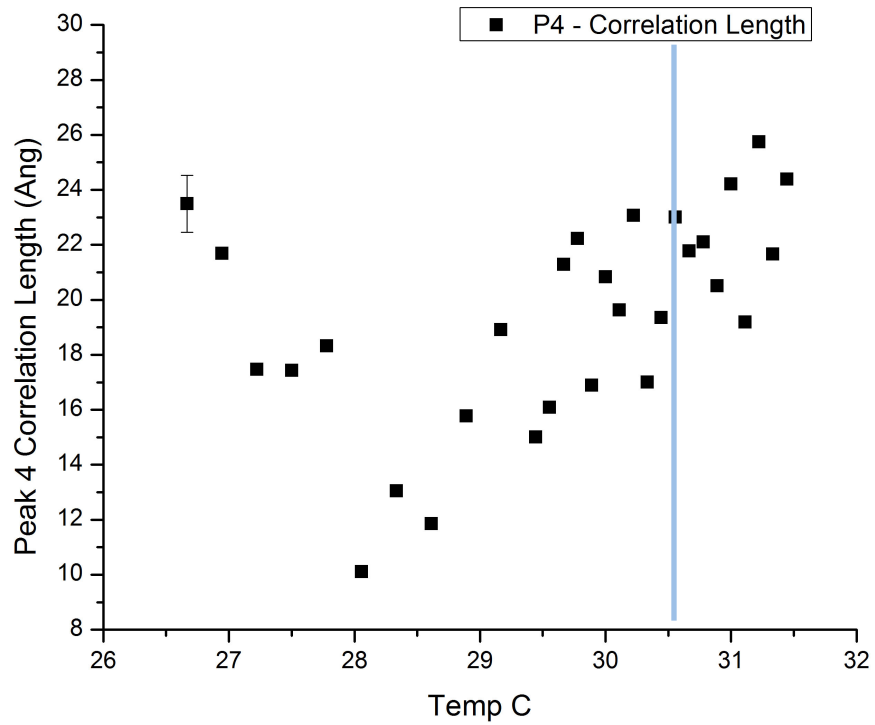


Figure 59: Correlation length of high q peak (Peak 4); Temperature  $\pm 0.056^\circ\text{C}$ ; error shown applies to all data points.

Figure 60 shows the correlation lengths of all the peaks studied as the temperature is raised. It demonstrates that peak 2 (smectic layer spacing,  $q=0.4\text{\AA}^{-1}$ ) had the most wildly fluctuating data, and peak 1 (smectic layer spacing of near-normal molecules,  $q=0.2\text{\AA}^{-1}$ ) had the highest average correlation length. All or most of the peaks appear to be under the effects of the functionalization compound.

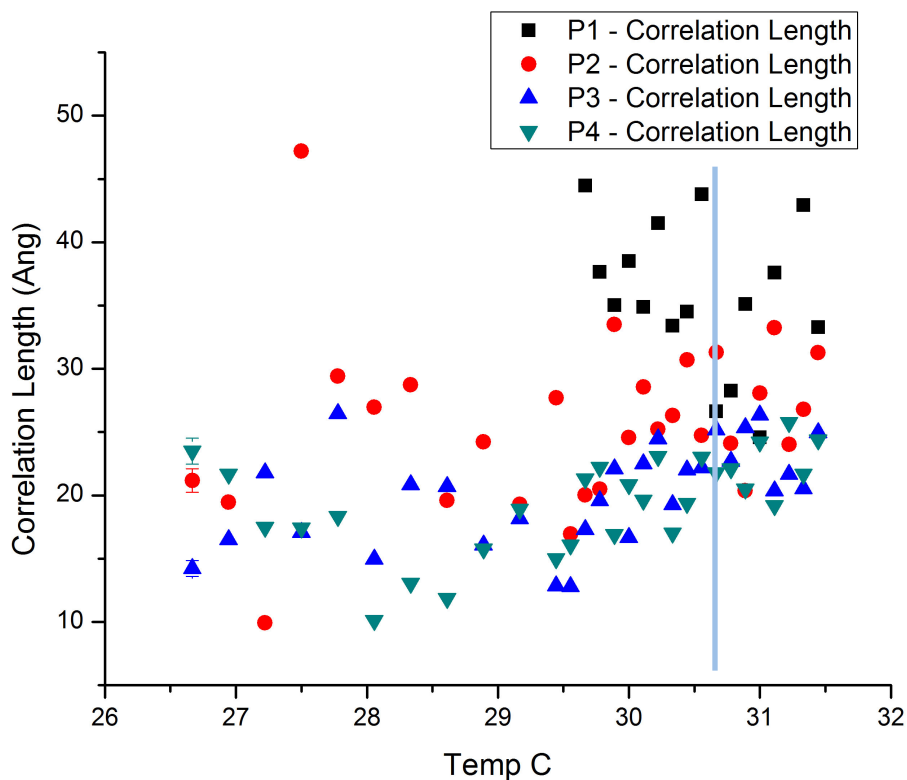


Figure 60: Summary of correlation lengths; Temperature  $\pm 0.056^\circ\text{C}$ ; error shown applies to all data points.

## PEG

We measured a second set of samples using a different functionalization compound, which we can compare to our completed MHDA composite experiment. We produced a sample with the same 30% by weight concentration of nanoparticles as in the first dataset, but replaced the MHDA nanoparticles with PEG-coated nanoparticles. We then ran the same set of scans at the same temperatures and parameters.

The room temperature curve for the PEG particles, seen in Figure 61, is markedly different from the MHDA curve at the same temperature. This plot shows a very distinct  $q=0.7\text{\AA}^{-1}$  peak that is relatively narrow compared to that which appeared in the MHDA data.

Nearing the Sm-N transition temperature, in Figure 62 we see a slight decrease in the intensity of the  $q=0.7\text{\AA}^{-1}$  peak, but no other changes. This is surprising, given the constant fluctuating of the peak locations and intensities in the MHDA data. Another difference to note is the lack of a fourth peak in this data.

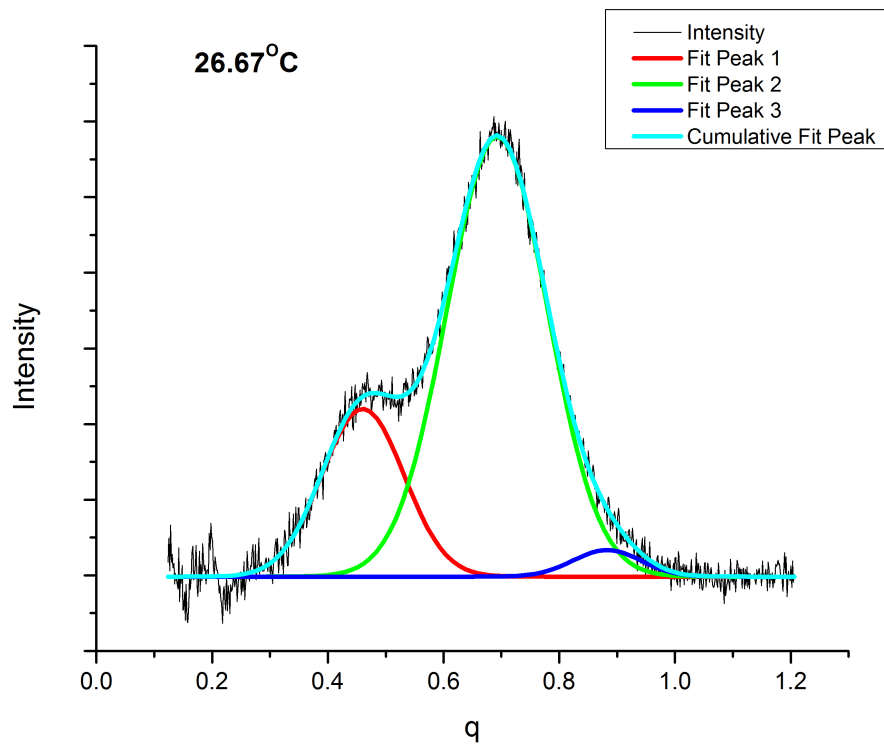


Figure 61: Temperature 26.67°C ±0.056°C; smectic phase.

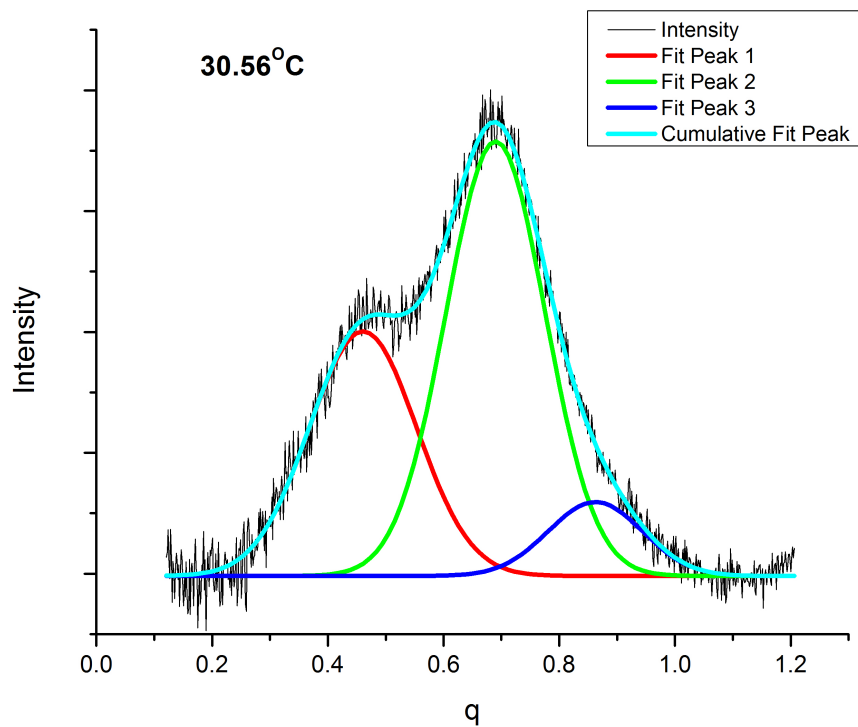


Figure 62: Temperature 30.56°C ±0.056°C; smectic phase.

At the transition, seen in Figure 63, we have another slight shrinking of the  $q=0.7\text{\AA}^{-1}$  peak and the high  $q$  peak has grown and shifted left slightly to about  $q=0.8\text{\AA}^{-1}$ , but no dramatic changes. This is surprising given the indications of disorder we found with the MHDA sample, none of which are present in this data.

Figure 64 shows data taken just above the transition temperature (into the nematic phase), where the high  $q$  peak lost intensity and shifted right to about  $q=0.9\text{\AA}^{-1}$ . The low  $q$  peak at  $q=0.45\text{\AA}^{-1}$  (for the smectic layer ordering) has lower intensity as well, while the peak at  $q=0.7\text{\AA}^{-1}$  appears unchanged.

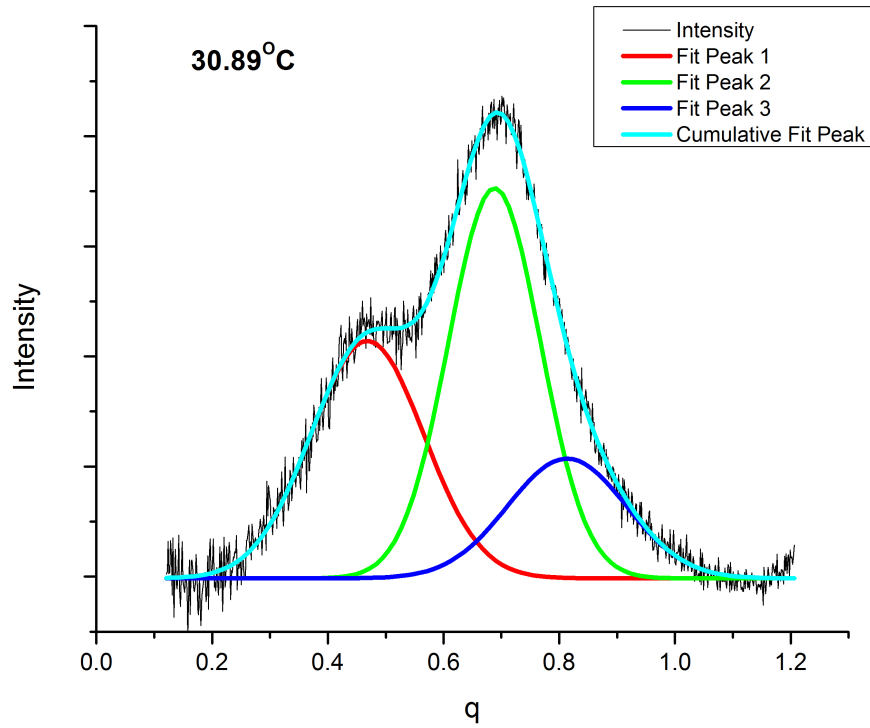


Figure 63: Temperature  $30.89^{\circ}\text{C} \pm 0.056^{\circ}\text{C}$ ; Sm-N transition.

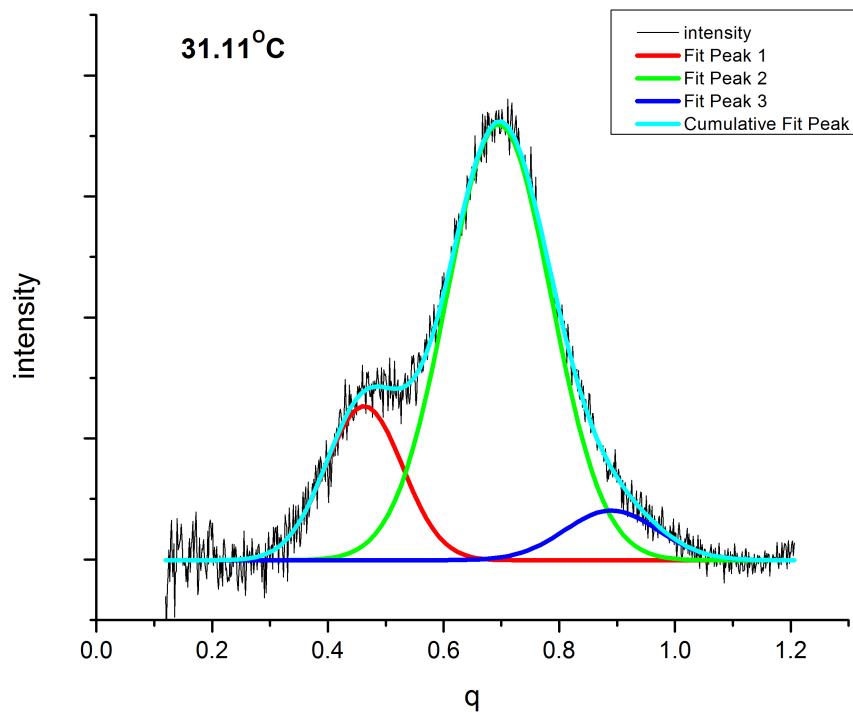


Figure 64: Temperature  $31.11^{\circ}\text{C} \pm 0.056^{\circ}\text{C}$ , nematic phase.

Almost a degree above the transition point into the nematic, this curve (Figure 65) is nearly identical to that seen closer to the transition. Given the dramatic instability seen in the MHDA sample, this kind of consistency is remarkable and gives convincing evidence that nanoparticle termination plays a key role in short-range molecular order. The two experiments were identical in all parameters except for the functionalization compound on the nanoparticles in the mixture. While MHDA molecules attached to a nanoparticle align the 8CB rods normal to the surface of the particle, the PEG molecules are large and flexible, and may be more likely to deform themselves to conform to the surrounding 8CB molecules rather than reorder them.

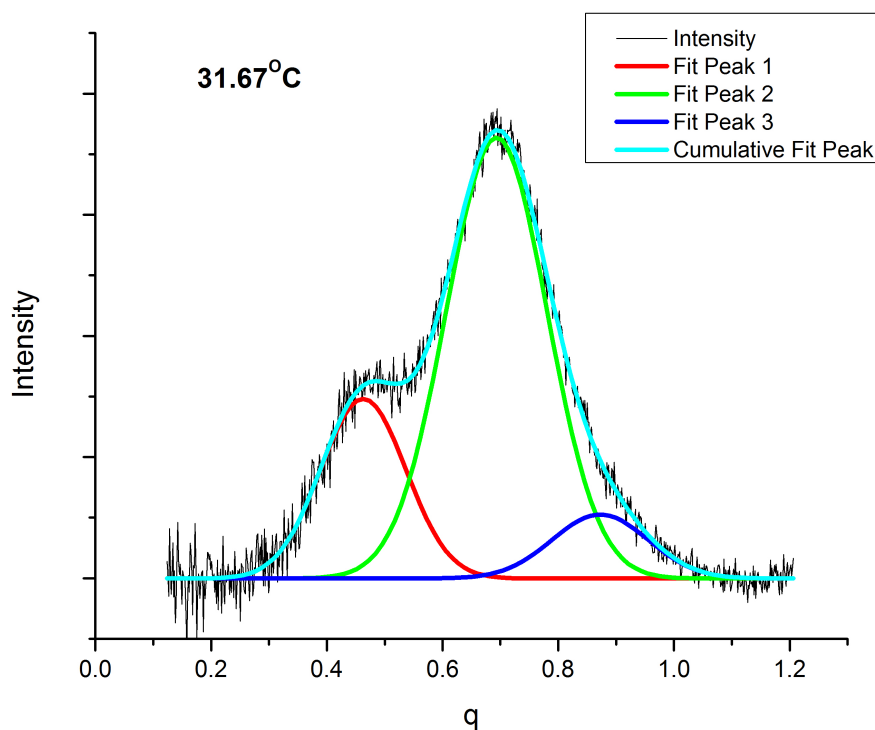


Figure 65: Temperature  $31.67^{\circ}\text{C} \pm 0.056^{\circ}\text{C}$ , nematic phase.

Figure 66 shows a summary of the movement of the low q peak as the temperature is raised throughout the experiment. The first thing to note about the movement of the low q peak (created by smectic layer diffraction, around  $q=0.4\text{\AA}^{-1}$ ), is that there is so little movement that this graph has to use three decimal points to make any significant analysis. What we can see at this scale is the small spike in position that occurs at the transition. The smectic layer spacing goes from an average of  $13.779\text{\AA}$  ( $\pm 0.120\text{\AA}$ ) in the smectic to  $13.368\text{\AA}$  ( $\pm 0.120\text{\AA}$ ) at the transition point, then back to an average of  $13.585$  ( $\pm 0.120\text{\AA}$ ) in the nematic. In terms of molecule tilt angle, the average tilt angle from normal in the smectic phase is  $64.06^\circ$  ( $\pm 0.24^\circ$ ),  $64.89^\circ$  ( $\pm 0.24^\circ$ ) at the transition, and  $64.45^\circ$  ( $\pm 0.24^\circ$ ) in the nematic (all with respect to the substrate). This signal is most likely caused by the molecules aligning with one of the edge facets (110), forming a 45 degree angle with the cubic faces (100). So the tilt angle with respect to the facet goes from  $19.06^\circ$  ( $\pm 0.24^\circ$ ), to  $19.89^\circ$  ( $\pm 0.24^\circ$ ) at the transition, to  $19.45^\circ$  ( $\pm 0.24^\circ$ ) in the nematic. To clarify, when the phrase “in the nematic” is used, it is referring to the state of the bulk.

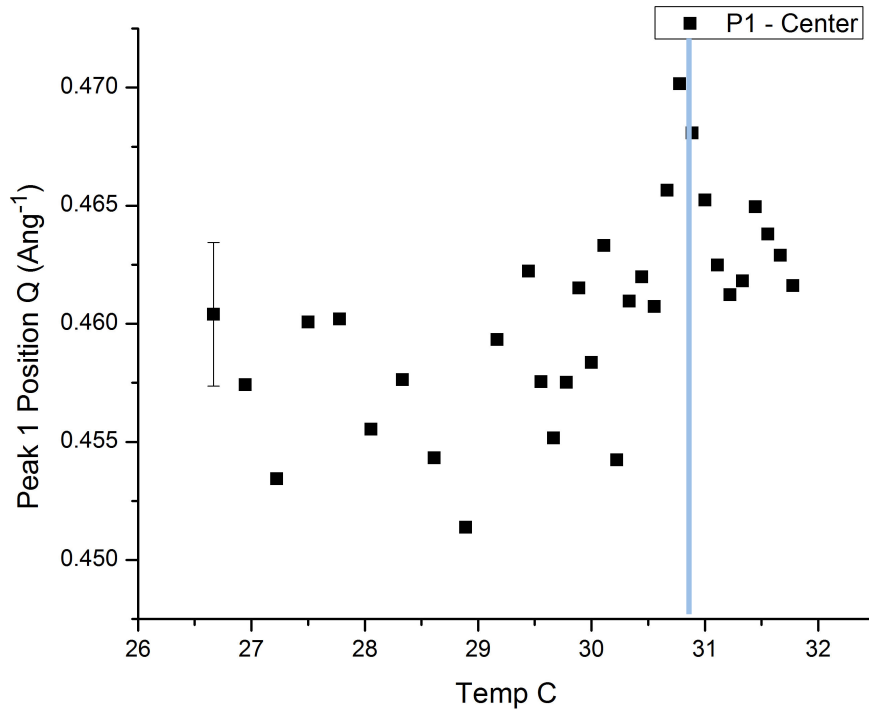


Figure 66a: Position of low q peak; Temperature  $\pm 0.056^{\circ}\text{C}$ ; error shown applies to all data points.

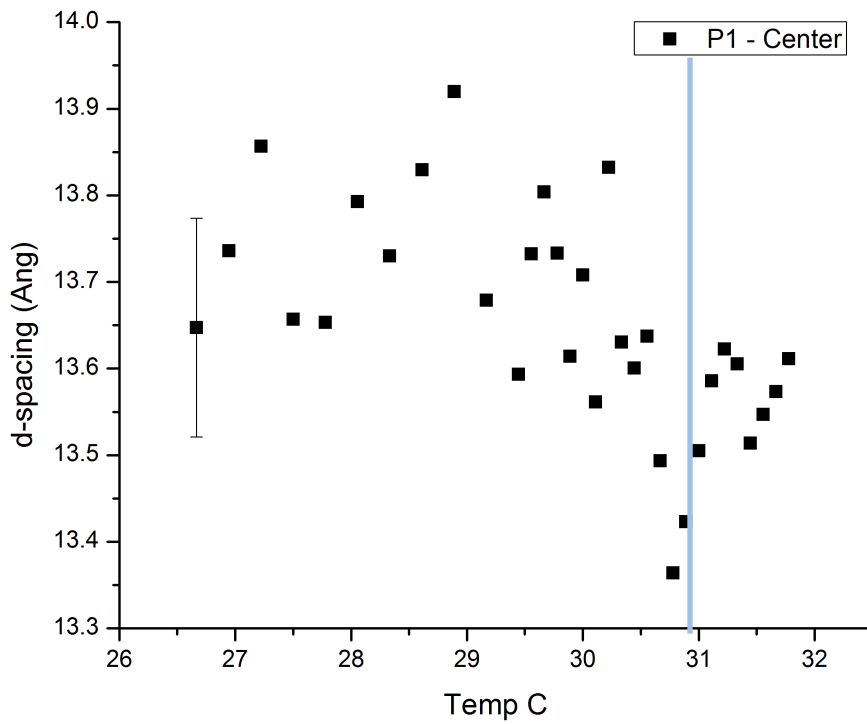


Figure 66b: d-spacing of low q peak vs. Temperature; Temperature  $\pm 0.056^{\circ}\text{C}$ ; error shown applies to all data points.

As with the low  $q$  peak, the peak around  $q=0.69\text{\AA}^{-1}$ , had very little movement as well (Figure 67). By far the most dramatic movement occurred at the transition, where the spacing went from a high of  $9.132\text{\AA}$  ( $\pm 0.032\text{\AA}$ ) to a low of  $9.002\text{\AA}$  ( $\pm 0.032\text{\AA}$ ).

The high  $q$  peak, around  $q=0.9\text{\AA}^{-1}$ , has more movement than the other two, but has a distinct and very brief position shift at the transition temperature (Figure 68). This brings the maximum spacing to  $7.757\text{\AA}$  ( $\pm 0.159\text{\AA}$ ) from an average of  $7.100$  ( $\pm 0.159\text{\AA}$ ).

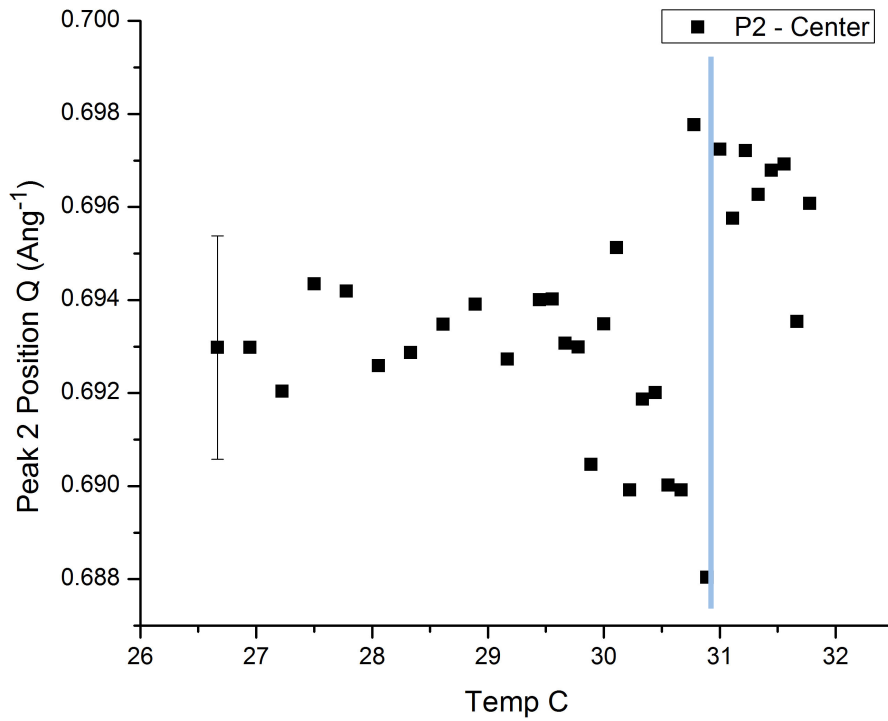


Figure 67a: Position of mid q peak; Temperature  $\pm 0.056^\circ\text{C}$ ; error shown applies to all data points.

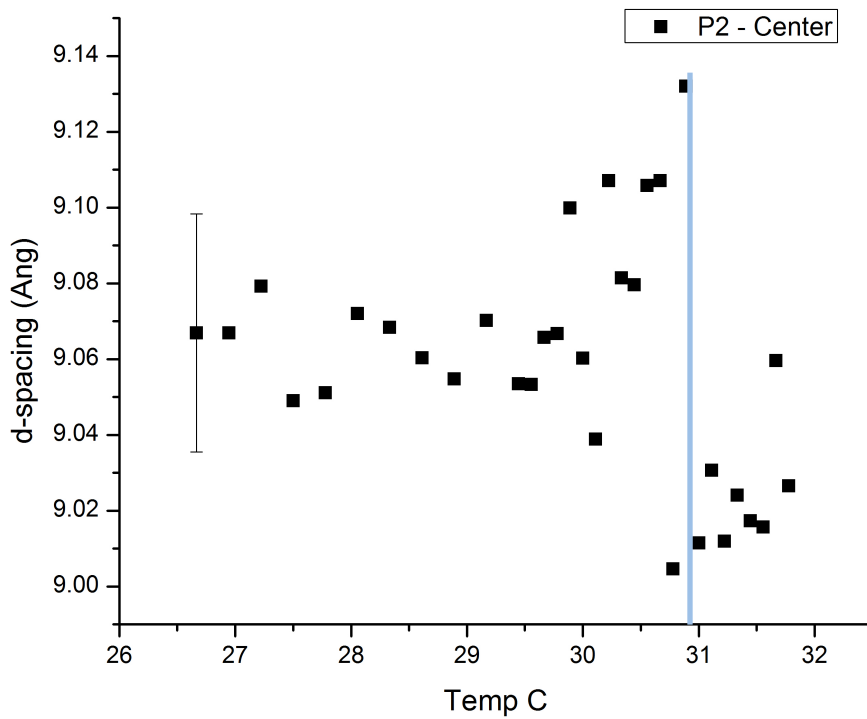


Figure 67b: d-spacing of mid q peak vs. Temperature; Temperature  $\pm 0.056^\circ\text{C}$ ; error shown applies to all data points.

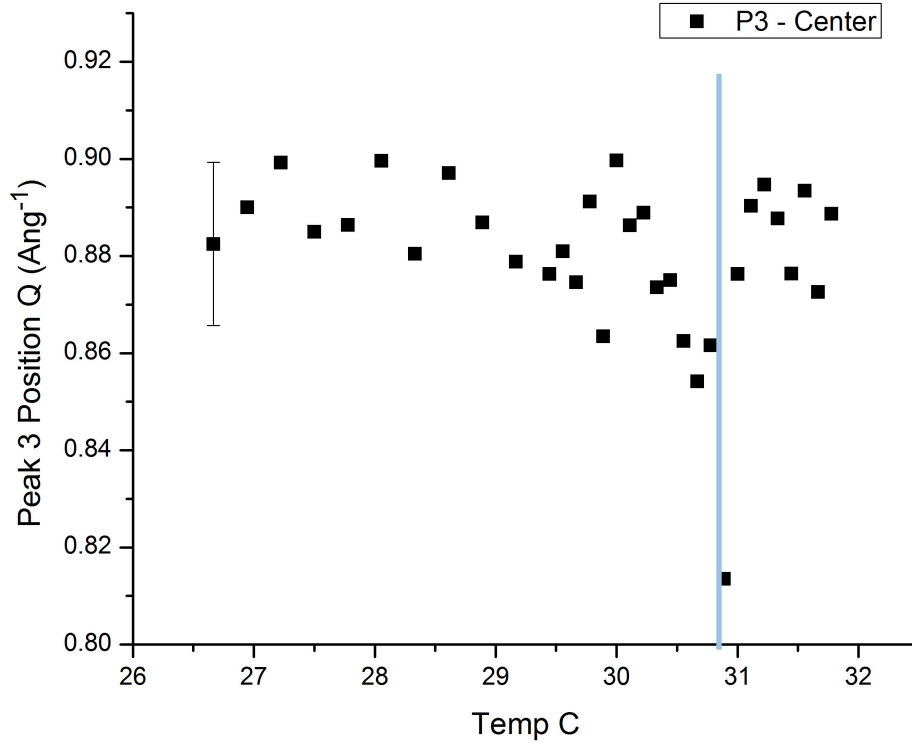


Figure 68a: Position of high q peak; Temperature  $\pm 0.056^{\circ}\text{C}$ ; error shown applies to all data points.

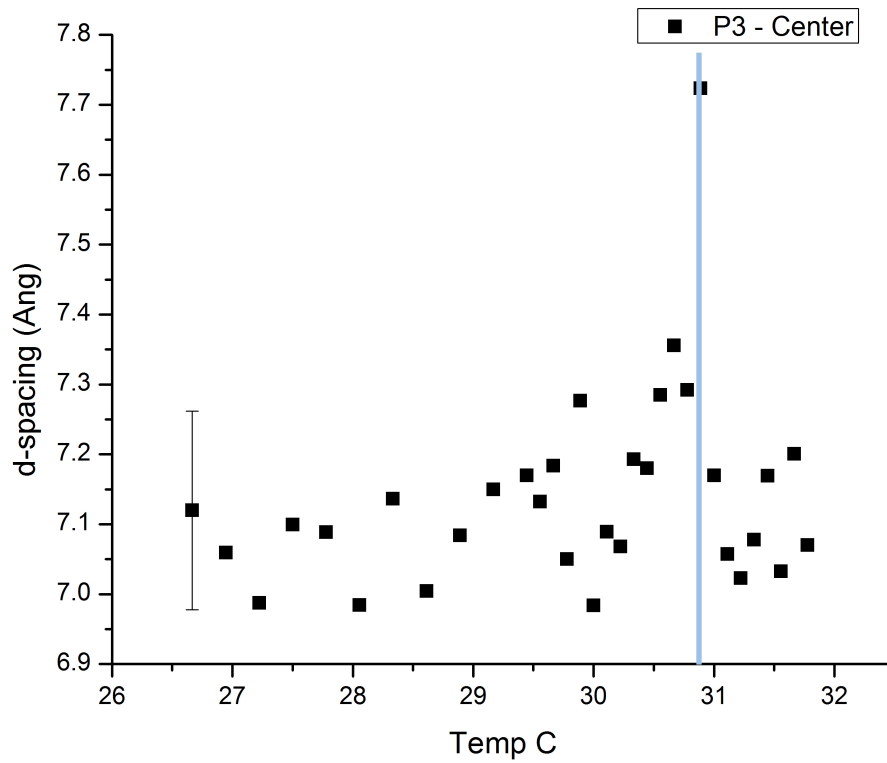


Figure 68b: d-spacing of high q peak vs. Temperature; Temperature  $\pm 0.056^{\circ}\text{C}$ ; error shown applies to all data points.

Compared to the MHDA peak movement summary, the PEG samples had remarkably little movement throughout the experiment (Figure 69). The transition point is easily identified by a small deviation. Interestingly, the scattered signal was stronger and less noisy than that of the MHDA experiment.

The correlation length of the low  $q$  peak (around  $q=0.4\text{\AA}^{-1}$  seen in Figure 70) has a much more distinct change at the transition temperature than did the peak position, increasing from about  $27\text{\AA}$  to  $40\text{\AA}$ . As was mentioned earlier, the 8CB “rod” length of  $31.5\text{\AA}$  means that this is little more than the length of the molecule. It may seem like this distance would have to be a multiple of the length of the rods, but we found from the peak position that the  $d$ -spacing here  $13.6\text{-}13.8\text{\AA}$  because the rods are at an angle. The correlation length is also an average, as there will be some areas with three layers and others with four, the average comes out to a non-integer in between.

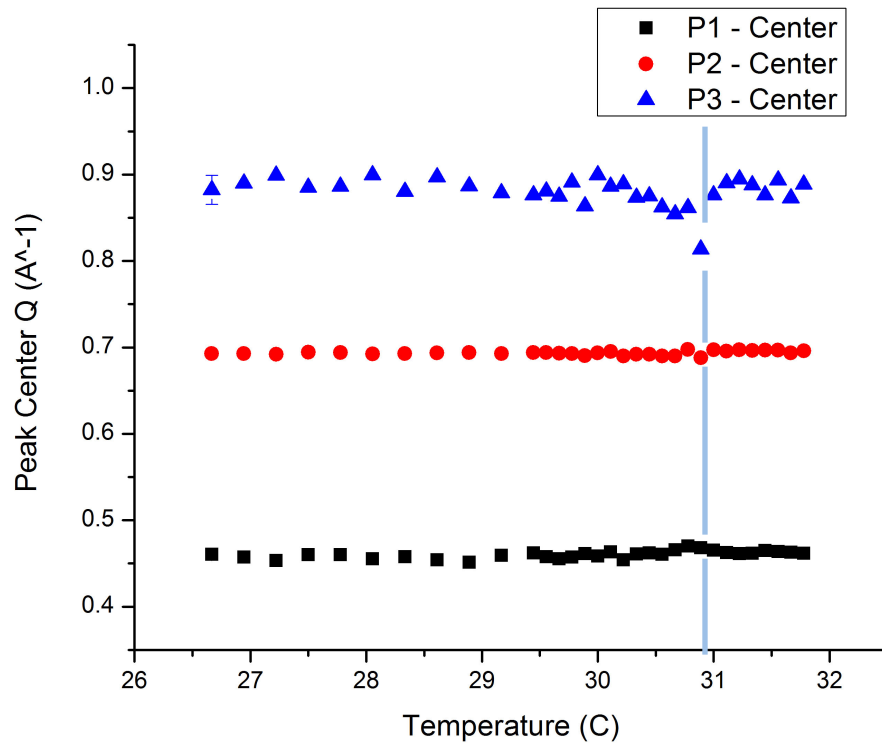


Figure 69a: Summary of peak positions; Temperature  $\pm 0.056^\circ\text{C}$ ; error shown applies to all data points.

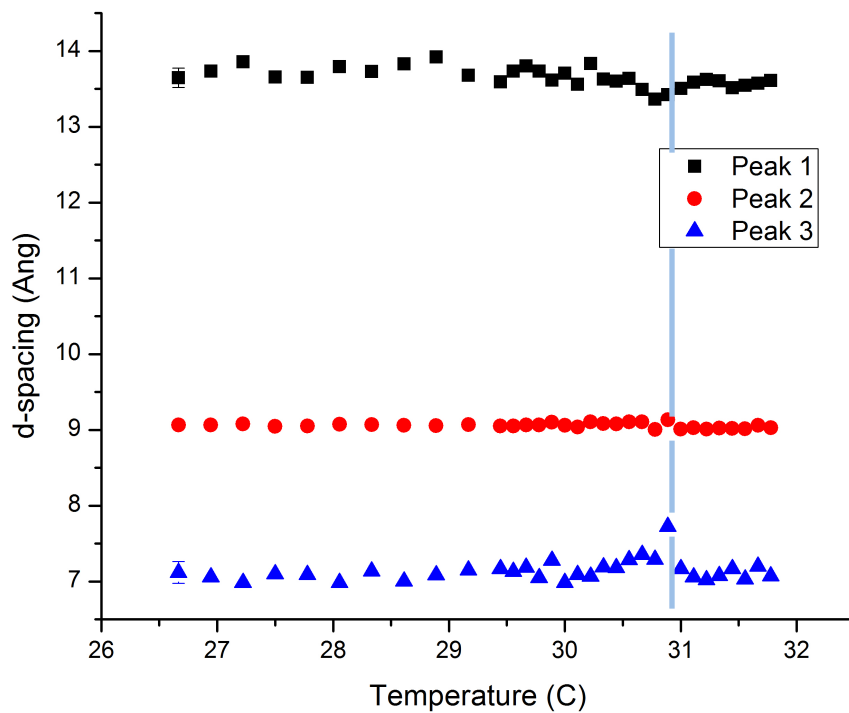


Figure 69b: Summary of PEG d-spacings; Temperature  $\pm 0.056^\circ\text{C}$ ; error shown applies to all data points.

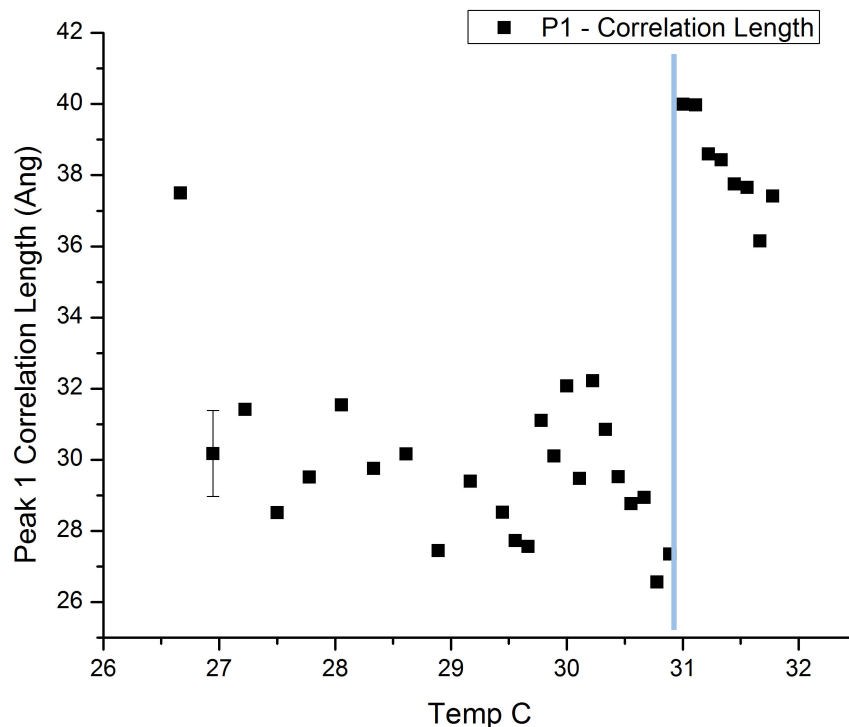


Figure 70: Correlation length of low q peak; Temperature  $\pm 0.056^\circ\text{C}$ ; error shown applies to all data points.

The correlation distance of the central peak (around  $q=0.69 \text{ \AA}^{-1}$  seen in Figure 71) only fluctuates a few angstroms throughout the experiment, with a small spike at the transition temperature. With an average d-spacing of  $9.065 \text{ \AA}$ , we can deduce that the molecular order is correlated for three or four molecular “rods”.

The high q peak (around  $q=0.9 \text{ \AA}^{-1}$  seen in Figure 72) varies in correlation length more than the central peak, with a sizeable drop between room temperature and the transition point. We only have eight data points in the nematic phase to use for reference, but it appears that the correlation length is generally the same on the nematic side of the transition as it is on the smectic side. This holds true for the central and high q peaks, but the low q peak had significantly higher correlation lengths in the nematic phase.

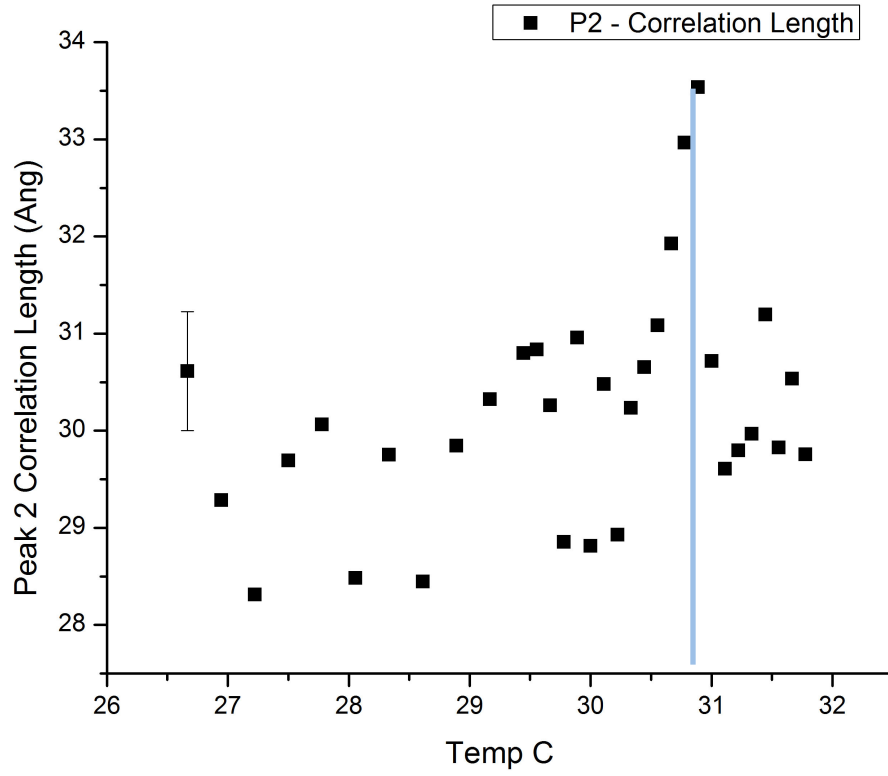


Figure 71: Correlation length of mid q peak; Temperature  $\pm 0.056^\circ\text{C}$ ; error shown applies to all data points.

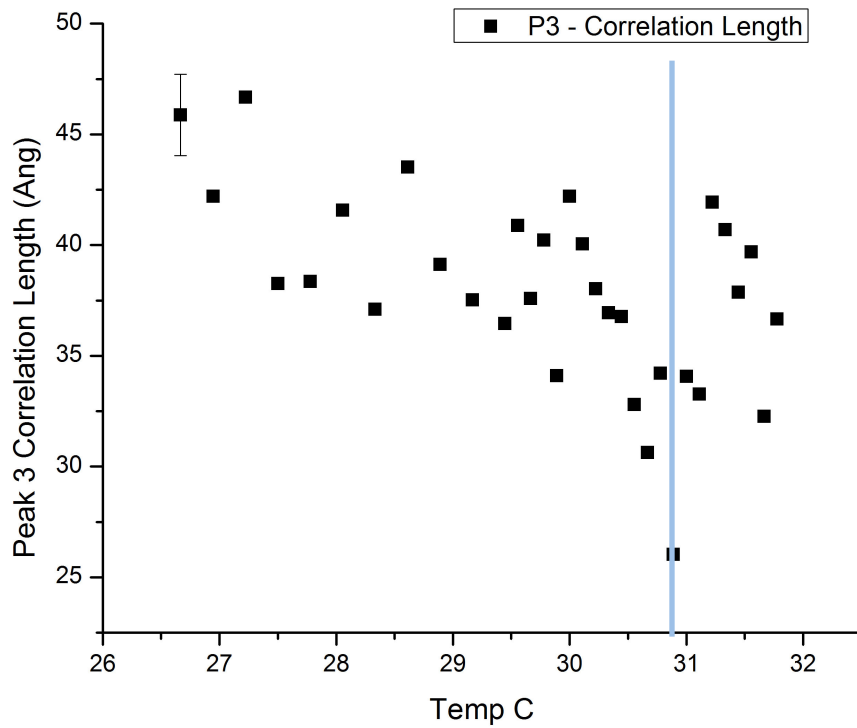


Figure 72: Correlation length of high q peak; Temperature  $\pm 0.056^\circ\text{C}$ ; error shown applies to all data points.

The transition point is clearly visible in this summary data in Figure 73, although each of the three peaks behaves differently at the transition. The correlation length of the low q peak is discontinuous at the transition with a sudden increase of 13Å. The central q peak is continuous with a small increase at the transition. The high q peak is continuous with a large, gradual decrease to its minimum at the transition.

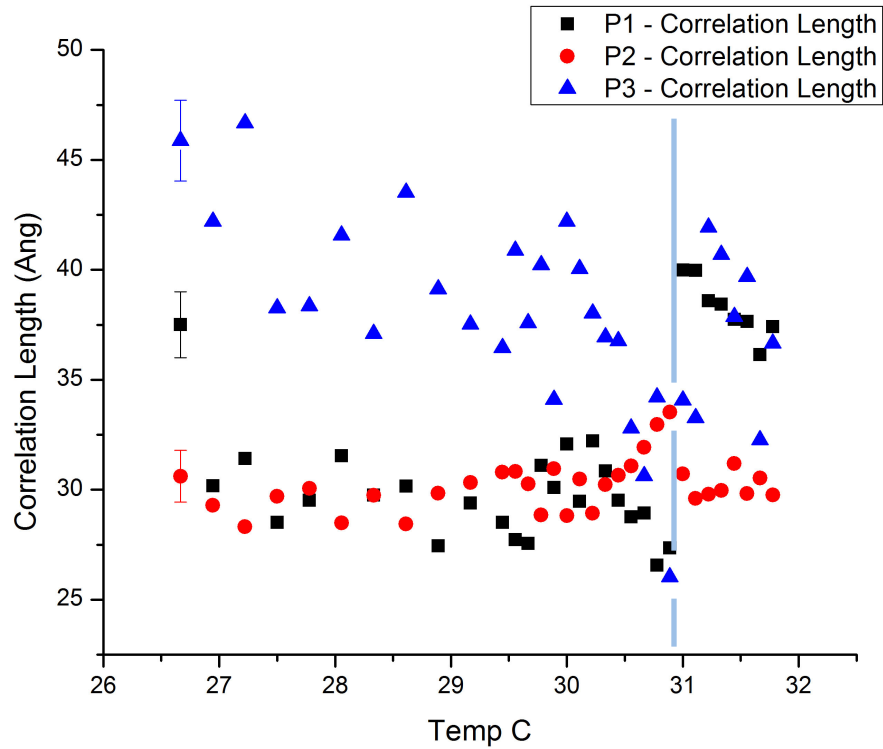


Figure 73: Summary of correlation lengths; Temperature  $\pm 0.056^{\circ}\text{C}$ ; error shown applies to all data points.

### Comparing the MHDA and PEG data

Figure 74 demonstrates how stable the smectic layer spacing around the PEG-coated particles is compared to MHDA-coated particles. Included in the graph are both the single peak present at lower temperatures and the second peak that appeared in the MHDA experiments, as both are credited with describing the smectic layer spacing. The MHDA sample has larger smectic layer spacing than the PEG for almost the entire experiment, meaning that the molecular “rods” are standing nearly normal to the nanoparticle surface in the MHDA sample, while nearly lying down in the PEG sample.

It is very easy to see in Figure 75 how much the MHDA peak moved around compared to the PEG peak. The liquid crystal molecule-to-molecule spacing is much more stable with a PEG-coated nanoparticle than an MHDA-coated one. The d-spacing in the MHDA sample was considerably larger than that of the PEG sample for the majority of the experiment.

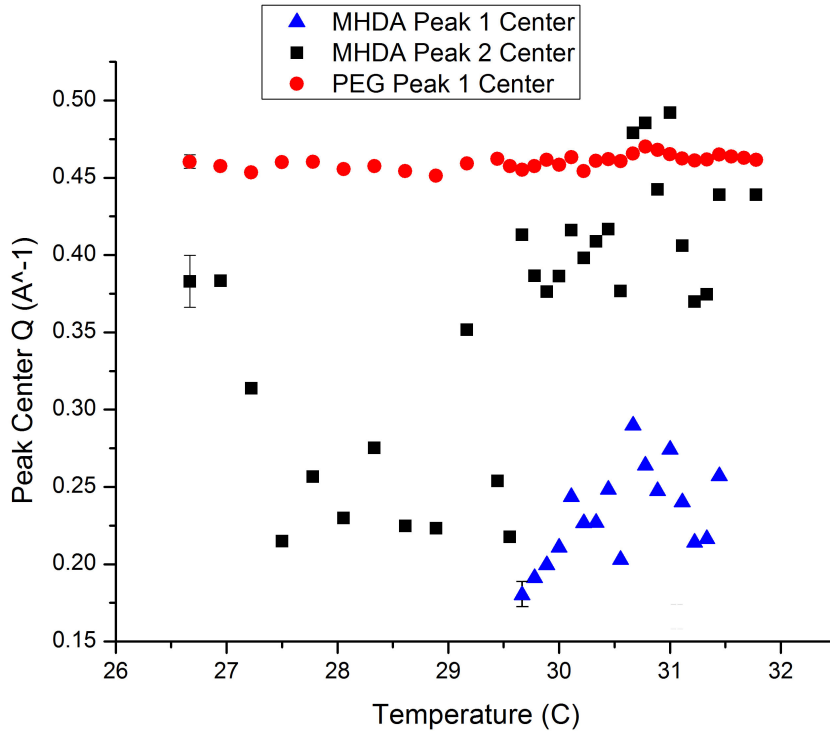


Figure 74a: Low q peak position comparison; Temperature  $\pm 0.056^\circ\text{C}$ ; error shown applies to all data points.

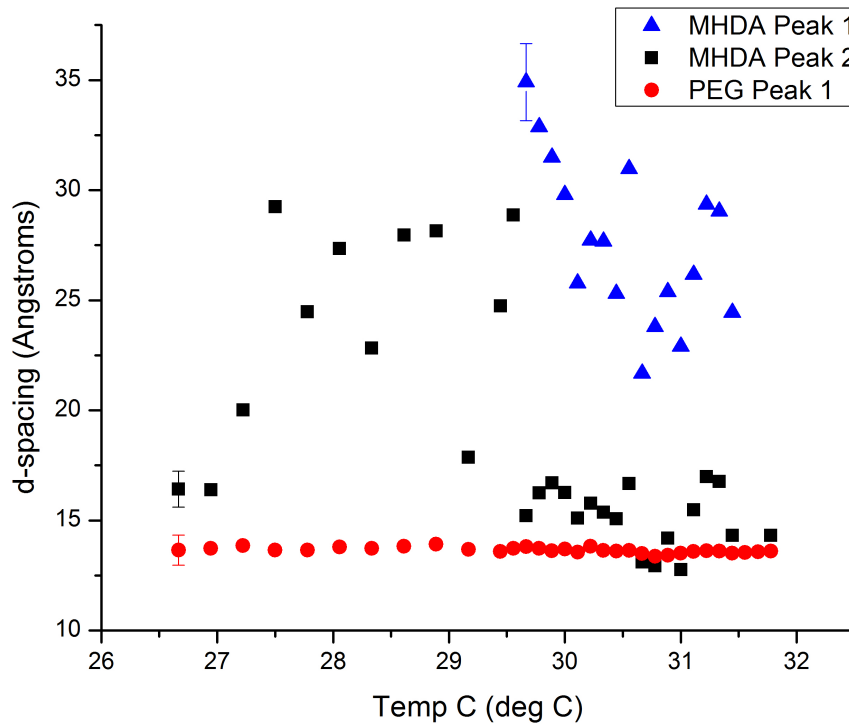


Figure 74b: d-spacing comparison of low q peaks; Temperature  $\pm 0.056^\circ\text{C}$ ; error shown applies to all data points.

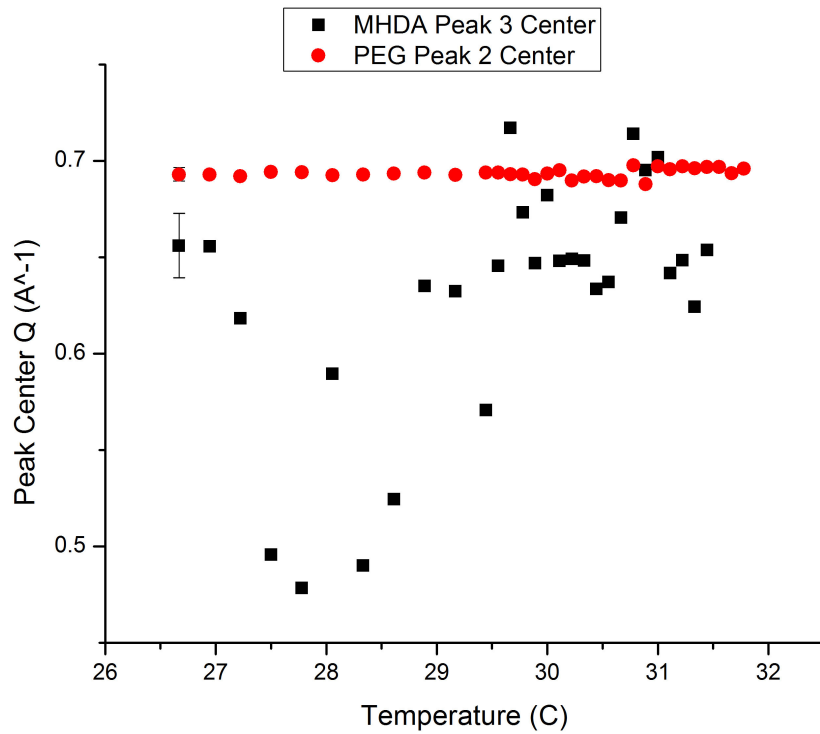


Figure 75a: Mid q peak position comparison; Temperature  $\pm 0.056^{\circ}\text{C}$ ; error shown applies to all data points.

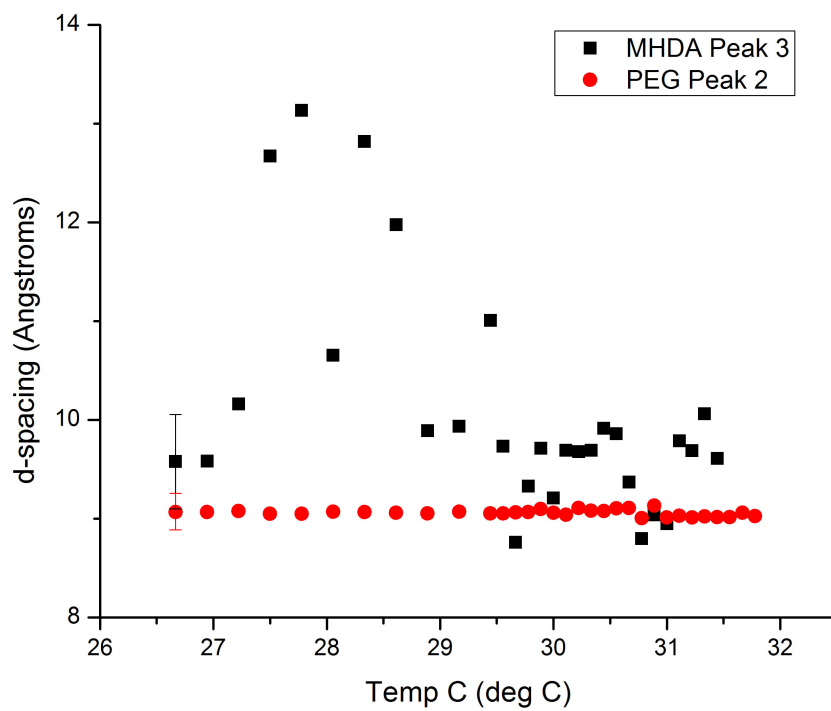


Figure 75b: d-spacing comparison of mid q peak; Temperature  $\pm 0.056^{\circ}\text{C}$ ; error shown applies to all data points.

The high q peak of the PEG experiments, shown in Figure 76, moved much more than the other two peaks, but it still was quite consistent compared to the MHDA sample. On average they are close in q-value, and by extension, close in d-spacing as well.

We can see in Figure 77 that while the correlation length of the PEG sample's smectic layer spacing is more consistent than the MHDA sample, their average values are similar.

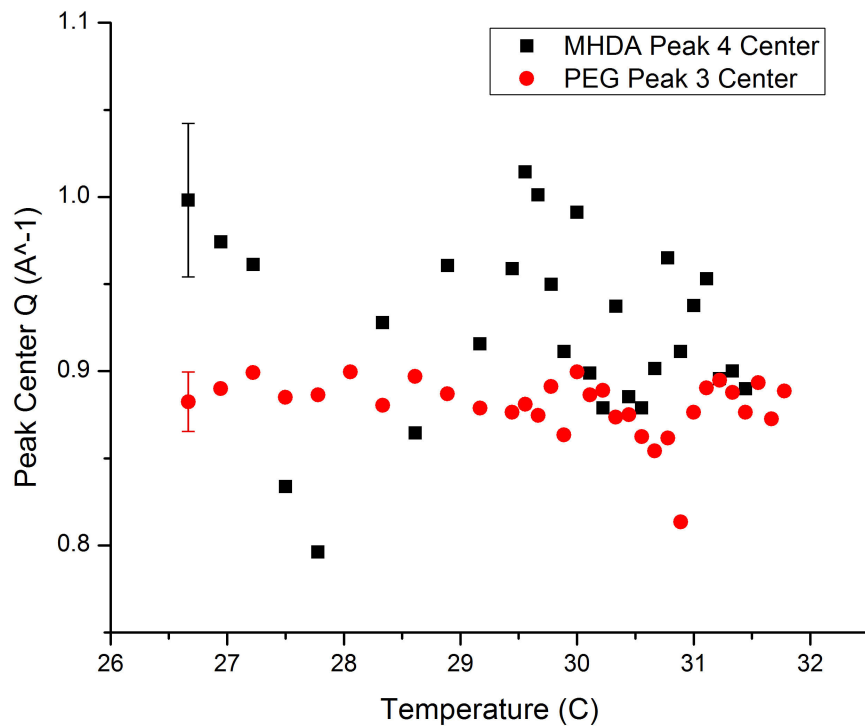


Figure 76a: High q peak position comparison; Temperature  $\pm 0.056^{\circ}\text{C}$ ; error shown applies to all data points.

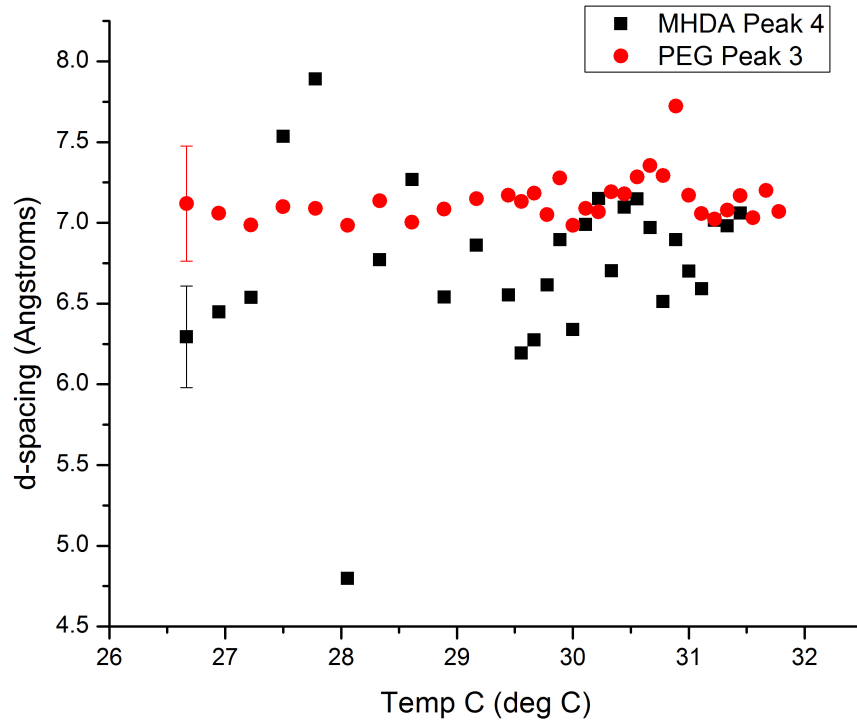


Figure 76b: d-spacing comparison of high q peak; Temperature  $\pm 0.056^\circ\text{C}$ ; error shown applies to all data points.

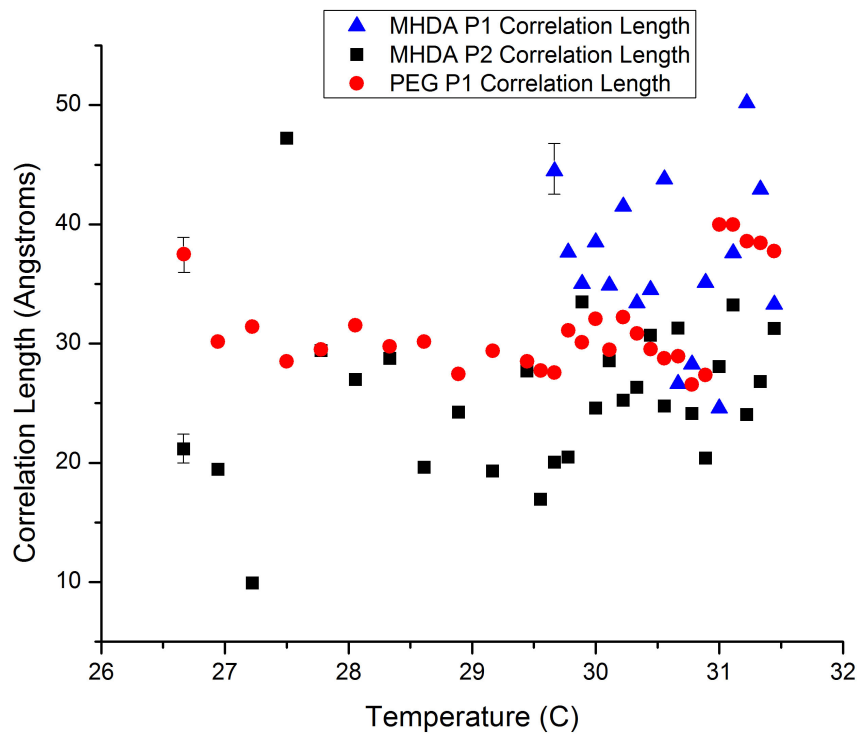


Figure 77: Low q peak correlation length comparison; Temperature  $\pm 0.056^\circ\text{C}$ ; error shown applies to all data points.

In Figure 78, the PEG sample had much higher correlation lengths for the molecule-to-molecule lateral spacing than the MHDA sample. This is most likely related to the size and shape of the interface involved in these interactions. MHDA is a very small molecule compared to PEG-3000. The outer diameter of the PEG coating on a 2nm nanoparticle will be greater than that of the MHDA coating on a 2nm nanoparticle. The curvature of the PEG-coated particle will cause less distortion in the smectic layers, in the form of bend and splay. This explains why the rods are closer together in the PEG sample, as was determined in the “movement of peak 2 comparison plot”. It is reasonable to assume that more tightly packed molecules have more influence on each other, in other words, greater correlation. This data supports that assumption.

In Figure 79, the PEG sample had substantially higher correlation lengths. With the bend and splay induced by the tight curvature on the surface of an MDHA-coated nanoparticle, the smectic layers around that particle will form disclinations (liquid crystal dislocations) and experience frustration in close proximity to well ordered smectic layers that do not match in director and plane alignment. These frequent disclinations will prevent long correlation lengths from being possible. The larger radius of the PEG-coated nanoparticles causes less bend, twist, and splay in the smectic layers, thus allowing longer correlation lengths before disclinations become necessary.

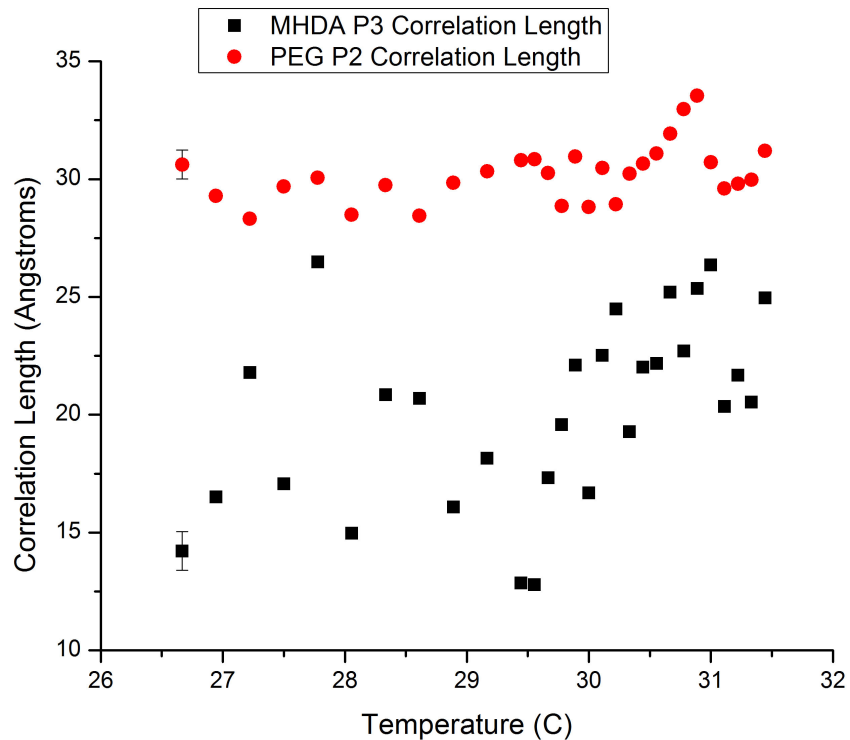


Figure 78: Mid q peak correlation length comparison; Temperature  $\pm 0.056^\circ\text{C}$ ; error shown applies to all data points.

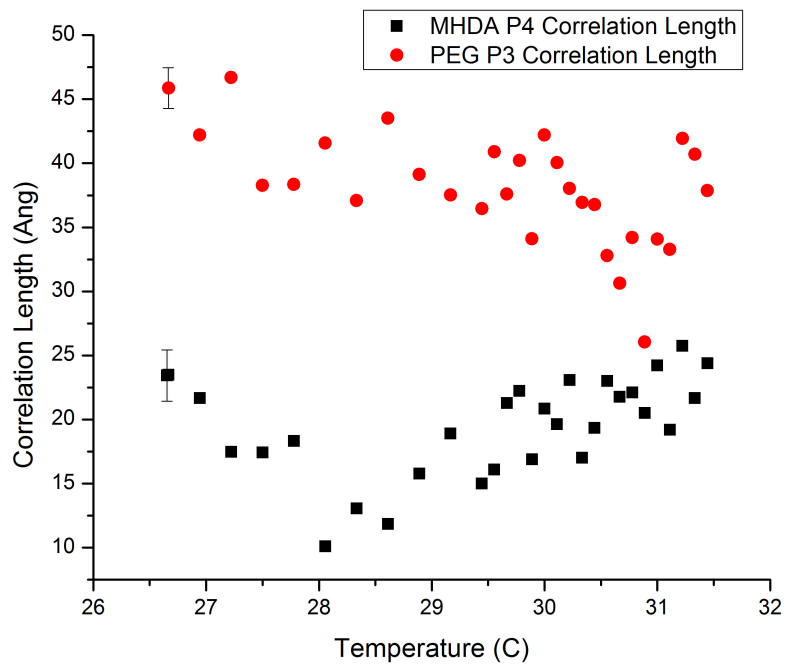


Figure 79: High q peak correlation length comparison; Temperature  $\pm 0.056^\circ\text{C}$ ; error shown applies to all data points.

## Chapter 5: Halo Phenomenon

### Observations

We observed that PEG coated particles exhibited a phenomenon where the liquid crystal formed a smectic layer in the vicinity of the particle, roughly circular in shape, surrounded by bare substrate (Figure 80) in the course of conducting our AFM experiments.

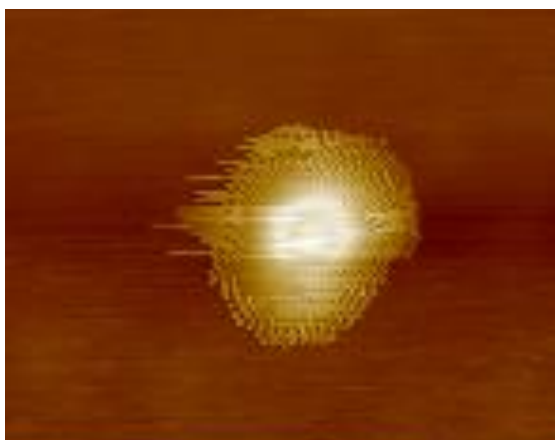


Figure 80: PEG-coated nanoparticle displaying halo. 8CB covering the PEG halo causes the wavy noise seen here.

We dubbed this the “halo phenomenon”, and found it was quite prevalent in areas where the concentration was thin enough to show the bare substrate. There have been many works that discuss the way the liquid crystal, the nanoparticle, and the functionalization interact,[30] involving a structure that looks as the “halo”. Most of these works involve the nematic phase and particles in the micron range.

We performed AFM scans on a dilute deposition of PEG coated particles to see if the PEG itself was visible as a halo. If not, the 8CB would for some reason be forming these unique structures with these particles that we did not see with any other functionalization compounds. Figure 81 shows a PEG coated particle on bare glass with no liquid crystal.

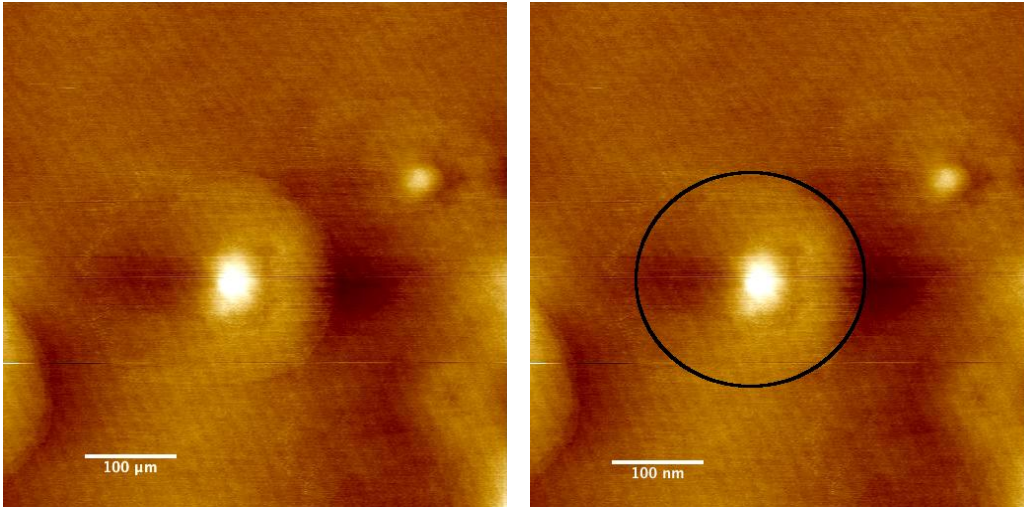


Figure 81: AFM micrograph of PEG-coated nanoparticles on glass. Right image outlines boundary of a “halo” with radius of 110-135 nanometers.

The halo is still quite visible despite the absence of the 8CB, stretching a distance of 85-110 nm from the particle. So rather than the liquid crystal causing this phenomenon, the 8CB interacts with the PEG halo by preferring to assemble its smectic layers on the hydrophilic PEG rather than on the glass substrate.

The PEG spread out into a disc in contact with the substrate for AFM scanning, but in solution or mixed in with liquid crystal, it would surround the nanoparticle in three dimensions. Whereas the 8CB could form a single continuous smectic layer across the halo in AFM images, with its molecules oriented normal to the surface (Figure 82-a), in three dimensions, the PEG molecules would spread out in all directions, allowing 8CB rods to fit between them. The length of the PEG molecules, about 26.8nm, is much longer than the correlation length found in the X-ray experiments, at most 4.5nm. This means that the PEG enables a few smectic layers to form (Figure 82-b), and beyond that distance, the molecules reach up through the smectic layers of the bulk (along the director). This interaction with the bulk stabilizes the molecules and prohibits 8CB tilt.

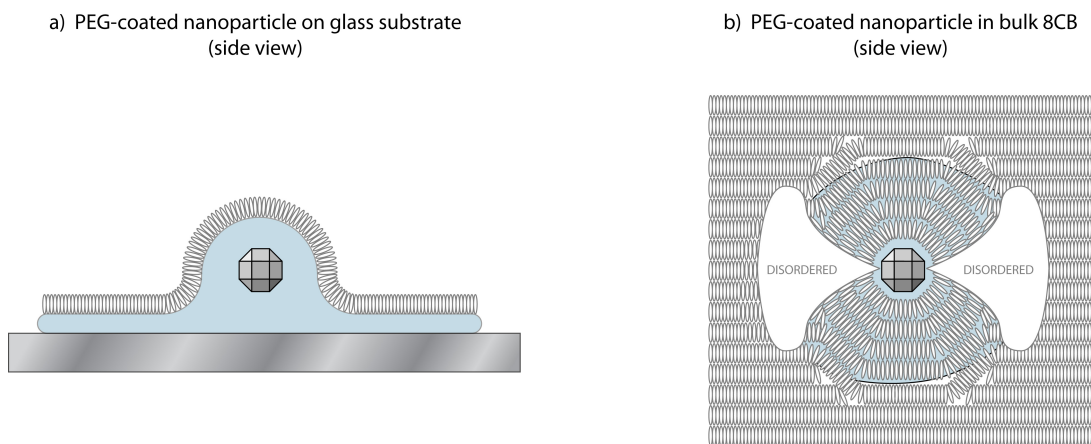


Figure 82: a) (Left) Side view of PEG-coated nanoparticle on glass substrate with 8CB monolayer covering PEG. b) (Right) Side view of PEG-coated nanoparticle in bulk 8CB. 8CB molecules form smectic layers near particle, but form disordered zones where the 8CB molecules would meet the bulk at 90 degree angles.

Additionally, a dislocated area develops in the vicinity of the PEG-coated particle. Where we normally measure a low  $q$  peak in our X-ray scattering experiments (see Figure 83) from those smectic planes perpendicular to the substrate, the long PEG molecules allow a disordered region to form (shaped something like a torus around the particle). The  $90^\circ$  angle at which these 8CB rods would meet the bulk would require high energy bend and twist distortions, so simply disordering requires less energy. The 8CB rods influenced by the PEG molecules can still form smectic layers because they meet the bulk at smaller angles, requiring only low energy splay distortions.

This phenomenon is most visible with the PEG-coated particles because PEG-3000 is a very large molecule relative to MHDA and APTS, and its solubility causes it to extend a significant distance from the particle in an aqueous solution. While MHDA extends out into the aqueous medium as well, its short length makes it undetectable with the current capabilities of our AFM. APTS does not extend out into the medium,

however all three functionalization compounds would cause the smectic layers shown in Figures 82 and 83 to form.

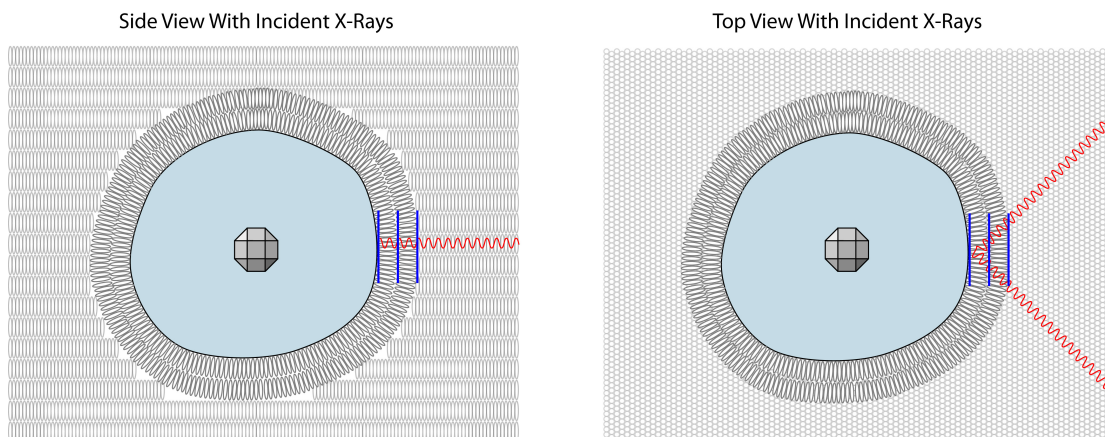


Figure 83: (Left) Side view of a nanoparticle in 8CB with an incident X-ray (red) whose trajectory is in-plane with the smectic layers of the bulk. (Right) Top view of nanoparticles with X-ray beam diffracting off smectic layers (blue).

Introduction of functionalized nanoparticles to a liquid crystal material changes its transition temperatures as we have discussed previously (refer to Table II and Cordoyiannis[8]). The transition can be thought of as an exchange of thermal and entropic energy. In gaining thermal energy, its molecules transition from an ordered state to a less ordered state. Samples of pure 8CB in the smectic state have lower entropy than a mixture of 8CB and coated nanoparticles at the same temperature. This is due to the polycrystalline structure surrounding each nanoparticle, which is more disordered than the continuous smectic planes in pure 8CB. The interfacial energy in each disclination (liquid crystal defect) lowers the amount of energy needed to overcome the entropy of the system and transition to the nematic phase.

The AFM images we obtained of the “halo phenomenon” give us some important clues of the interaction between 8CB and PEG. First, these images confirm a strong affinity between 8CB and PEG. Figure 80 clearly shows a flattened PEG halo

spread out across the substrate surrounded by bare glass, but the halo and nanoparticle are covered in 8CB. There are no visible islands of 8CB smectic layers on the bare glass substrate in the vicinity of the halo, or even within several micrometers. The 8CB accumulated only on the PEG halo.

Second, the 8CB appears to have formed a monolayer of liquid crystal molecules on the PEG halo. There are no visible step edges that would be easily discernable at the scale of these micrographs. This suggests that 8CB has a greater affinity with PEG than it has with itself.

Third, the PEG stretches a great distance from the surface of the nanoparticle compared to the MHDA molecules. The PEG can reach a radius of 26.8 nanometers from the nanoparticle, while the MHDA only extends about 10 angstroms. This is likely the source of the greater correlation length and stronger X-ray signal found in our PEG experiments compared to the MHDA experiments. The length of the PEG molecule gives it the ability to influence a greater number of 8CB molecules, although its flexibility keeps its correlation length still in the tens of nanometers.

## Chapter 6: Relating AFM findings to X-ray findings

AFM and X-ray scattering are both well suited to studying liquid crystal systems, but provide different types of information. They are complementary techniques that give us a view of the sample on multiple scales. The data from AFM is very detailed with nanometer resolution, but it is localized data that only describes the area being scanned. In our case, the scans we obtained were at most  $5\mu\text{m} \times 5\mu\text{m}$ , and more commonly only  $1\mu\text{m} \times 1\mu\text{m}$ . X-ray scattering, on the other hand, is more of a bulk measuring technique. Although it has sub  $1.0 \text{ \AA}^{-1}$  resolution, the data is collected from many different planes in the sample. The detector simply counts how many photons it collects at different angles over the 20 second dwell period. The data that we analyze is an average of signals from many small diffracting crystals.

We get a well-rounded view of what is happening at a molecular level by combining the two techniques. With X-ray scattering, we have an averaged measurement of layer spacing, which allows us to calculate the average angle the molecule is oriented from normal, which we can use in calculating the surface energy of the membranes we study using AFM. The surface energy is one of the components of our model describing the interaction between a coated nanoparticle and a liquid crystal membrane.

AFM allows us to observe the interaction of the liquid crystal membrane with nanoparticles and how this intermolecular structure depends on the functionalization of the nanoparticle. X-ray scattering gives us the data we need to describe the interaction. To do this, we start with the energy model mentioned earlier:

$$E = E_{\text{mech}} + E_{\text{magnetic}} + E_{\text{surface interaction}} + E_{\text{relative size}}, \quad (1)$$

$E_{\text{mech}}$  is a combination of the different distortion forces that are present in the location being studied.[12] The bend, twist, and splay induced in the membrane or bulk sample by the presence of a nanoparticle, and presented in Figure 17, all play a role in changing the mechanical energy of the system. In Eq. 1,  $E_{\text{mech}}$  is attempting to pull the membrane apart, whereas the other components are holding it together. When  $E_{\text{mech}}$  becomes larger than the surface energy and the size factor, a hole forms in order to maintain the lowest free energy in the system, or in the case of the bulk study, a disordered region, as shown in Figure 82 and 83. This is more likely to occur with a considerable amount of bend and twist distortions, as they are higher energy distortions than splay.

$E_{\text{magnetic}}$  is not a factor of concern in this model because there is no external magnetic field, as was used in previous research.[12, 40, 55, 87, 88] The magnetic moment of the nanoparticles is very small. Studies on using a magnetic field to induce a phase change have shown that a sample of pure 8CB requires an incredibly strong magnet (approximately 10 Tesla) to reorient the molecules.[55] Therefore we can safely disregard the influence of the nanoparticles' magnetic fields on the liquid crystal.

$E_{\text{surface interaction}}$  is described by the following equation for the surface energy:[12]

$$E_{\text{surface interaction}} = W \sin^2\Theta \quad (4)$$

In this equation (Eq. 4),  $W$  is the energy of the membrane at  $0^\circ$ , which has been found to be  $1.2 \times 10^{-19}$  J.[89]  $\Theta$  is the angle that the liquid crystal molecules form with the surface of the nanoparticle. When  $\Theta$  is 0, the liquid crystal molecule is tangential to the surface of the nanoparticle (perpendicular to the radius), so the surrounding molecules tend to

experience bend and twist distortions. When  $\Theta$  is 90, the molecules are normal to the surface, so the surrounding layers will splay.[12]

It is also necessary to consider the disparity between the size of the nanoparticles in the mixture and the smectic layer separation. When these two parameters are close in size, they will have more impact on each other's ordering than when one is much larger than the other. This parameter can be described by equation 5:[12]

$$E_{relative\ size} = B \exp \left( - \left( \frac{d_{LC} - d_{particle}}{d_{particle}} \right)^2 \right) \quad (5)$$

Here,  $d_{LC}$  is the distance between smectic layers that we measured at different temperatures in our X-ray studies, as described in Chapter 4.  $d_{particle}$  is the diameter of the nanoparticle, which we measured in our AFM studies in Chapter 3.  $B$  is on the same order as the constant  $W$  in equation 4 above. This Gaussian equation tells us that the closer the size of the liquid crystal and the nanoparticle are in value, the greater their interaction. When one is greater than the other, the effect diminishes on a Gaussian curve.[12]

The remarkable stability of the liquid crystal ordering in X-ray experiments on PEG-coated nanoparticle composites may be due to this relative size parameter. The MHDA molecule is much smaller than PEG-3000, so a nanoparticle coated in MHDA has a smaller outer diameter than one coated in long PEG-3000 molecules. The larger PEG-coated nanoparticles will have less influence on the small 8CB molecules, while the MHDA-coated nanoparticles are much closer to the same size as the smectic layer spacing. The MHDA-coated nanoparticles will therefore create many more defects and aid in the disordering of the liquid crystal structure.

## Chapter 7: Summary of Results

### *AFM*

We found evidence of hole formation in thin films of 8CB liquid crystal containing MHDA-coated nanoparticles, as well as APTS-coated nanoparticles. The size range where this takes place differed from the findings of Roiter, et al. in their studies of bare silica nanoparticles in phospholipid membranes. The uncovered size range was also dependent on the functionalization covering the nanoparticles. We were able to find enough instances of covered or uncovered nanoparticles to partially fill in a table describing the size ranges and their interaction with the membrane.

We obtained images of a previously unobserved phenomenon where PEG-coated nanoparticles take on the form of a disc with the nanoparticle at the center, rather than the soft spheroid with a nanoparticle nucleus that we have in solution. We dubbed this flattening the “halo phenomenon”, and we observed that when 8CB liquid crystals are present, the 8CB will prefer to accumulate on the flattened area of PEG but not on the surrounding substrate (refer to Figure 80). The PEG and 8CB seem to have a much greater affinity than 8CB does with glass.

### *Polarized Optical Microscopy*

This technique has proven to be extremely useful in its ability to provide immediate phase identification. The X-ray scattering temperature studies needed to include the transition temperature to ensure we obtain scans of both the smectic-A and nematic phases. In these systems, the functionalized nanoparticles can change this

transition temperature by several degrees C, and X-ray scattering is a time-consuming process, so being able to pinpoint this transition before scanning is crucial.

We have captured videos of the transition as seen through the polarized optical microscope, with the temperature controller set to the transition point (error of  $\pm 0.056^\circ\text{C}$ ), the transition is clearly seen to occur only at this temperature, and is stable in the smectic phase  $0.1^\circ\text{C}$  below and in the nematic at  $0.1^\circ\text{C}$  above. We identified the transition temperature for each sample before beginning the X-ray scattering experiments, and we were able to observe the transition as we had hoped.

### *X-ray Scattering*

We were able to collect two complete data sets from X-ray scattering experiments; one a composite containing 8CB and MHDA-coated nanoparticles, the other 8CB and PEG-coated nanoparticles. We are able to make a number of conclusions from the data we gathered, as reflected in the results of the correlation length and the intensity of the peaks.

The sample that contained PEG-coated particles showed remarkably little variation as the temperature was raised from the smectic to the nematic phase. In some cases, the deviations in the data that signaled the phase change were nearly too small to detect with our equipment. This inherent stability could be due to some affinity between 8CB molecules and PEG. It could also be that the malleable nature of the PEG coating enabled the 8CB molecules to reorder into preferred configurations of lowest free energy and less frustration. Another possible explanation is simply that the larger radius of the PEG coating induced less bend and splay into the 8CB smectic structure, thereby

allowing the 8CB to reach a more stable state. We found evidence to support each of these possibilities, and the truth may be a combination of the above.

The sample containing MHDA-coated nanoparticles behaved somewhat erratically, especially compared to the PEG sample. The molecular order seemed to change rapidly and continuously with small variations in temperature. This made identification of the transition point difficult in some of the data plots. More oddly, the peak position data all shifts to lower  $q$  values as the sample is heated from room temperature, but then shifts back when approaching the transition temperature. This means the d-spacing gets wider as you heat the sample, then contracts again when you continue to heat it. This could be evidence of some pre-transition change, but requires further work to confirm. We have found that the liquid crystals align according to the nanoparticle's faceting.

### Conclusion

Our research produced three results. We identified differing behavior in thin film samples of liquid crystal and coated nanoparticles dependent upon particle functionalization using AFM. Using X-ray scattering we measured the alignment and smectic layer formation in the presence of coated nanoparticles, even above the smectic-A to nematic transition temperature. We found evidence of a "halo" that forms around coated nanoparticles, particularly with longer coating molecules.

Our AFM experiments found evidence of liquid crystal membranes responding differently to nanoparticles coated in various compounds, and differently than the results found by other researchers using uncoated nanoparticles. Improved methods of particle dispersion would facilitate data collection in future experiments.[90]

Our X-ray experiments confirmed our theory that smectic order continues to exist above the Sm-A to nematic transition in the vicinity of the nanoparticles. Our results also confirmed the faceted nature of our nanoparticles and revealed that the smectic ordering in the vicinity of faceted nanoparticles orient according to the positioning of these nanoparticle facets.

We discovered the halo structure surrounding our nanoparticles when we began the AFM experiments, and the formation is so prevalent that it clearly plays a role in how nanoparticles coated in large molecules interact with their surroundings. We saw a significant stabilization of the PEG nanocomposite throughout the transition from Sm-A to nematic in our X-ray experiments, whereas the MHDA nanocomposite exhibited large fluctuations throughout. The presence of this large, flexible halo of PEG (which has an affinity for 8CB) may be the source of this stability.

### *Future Work*

Future research can be done with additional functionalization compounds to compare to the MHDA and PEG data sets. APTS and 7 (NHS) are of interest to this research group and are slated for investigation as soon as time and equipment permit. APTS is of interest because its molecules lay flat against the surface of the nanoparticle, as depicted in Figure 14, causing nearby 8CB molecules to orient tangential to the surface of the nanoparticle. This orientation should result in areas of correlated smectic layers forming with their directors tangential to the nanoparticle surface, rather than normal to it.

Experiments should be designed to investigate whether the halo phenomenon and its stabilizing effects occur with other long, flexible molecules similar to PEG 3000, in order to answer the following questions: What role does molecule length play in these effects? How does this phenomenon affect the electrical, optical, and magnetic properties of the composite?

Further work should be done by varying the concentration of nanoparticles in the composites to determine what impact these mechanisms have at lower concentrations, if any. There could be a critical concentration where their effect becomes significant. If these nanostructures are found to be biologically hazardous, this information could help identify safe exposure limits.

More time should be spent clarifying the size ranges at which holes form in membranes in the presence of the different functionalizations. This proved to be a challenging and time-consuming task, but it is important for building a mathematical model to predict hole-forming behavior. Improved techniques for deposition of nanoparticles and locating nanoparticles would speed this process, as would the use of equipment permitting location-repeatable scanning.

Future work should investigate the pre-transition change seen at 27.4°C in the MHDA sample, as indicated by the drastic change in correlation length of peak 2. Additional data is needed to identify these features as either anomalies, or whether they indicate some unknown behavior that could be of importance. Repetition of the experiment should be sufficient to obtain this data.

It may be possible to design a confocal or fluorescence microscopy experiment of PEG-coated nanoparticles in bulk 8CB that will allow the interface between the 8CB and the PEG coating to be imaged. One method may involve attaching fluorescent

markers to the ends of the PEG molecules that can be detected with specialized equipment. This may shed further light on the interaction between two soft materials, 8CB and PEG.

## Bibliography

1. Roiter, Y., et al., *Interaction of Lipid Membrane with Nanostructured Surfaces*. Langmuir, 2009. **25**(11): p. 6287-6299.
2. Collings, P.J., *Introduction to Liquid Crystals: Chemistry and Physics*. 1997, Philadelphia, PA: Taylor & Francis Ltd.
3. Bushby, R.J. and O.R. Lozman, *Photoconducting liquid crystals*. Current Opinion in Solid State and Materials Science, 2002. **6**(6): p. 569-578.
4. Nehring, J., et al., *High-pretilt polyphenylene layers for liquid-crystal displays*. Applied Physics Letters, 1987. **51**(16): p. 1283.
5. Qi, H. and T. Hegmann, *Impact of nanoscale particles and carbon nanotubes on current and future generations of liquid crystal displays*. Journal of Materials Chemistry, 2008. **18**(28): p. 3288.
6. Wang, C., et al., *Defect-Free Bistable CI Surface Stabilized Ferroelectric Liquid Crystal Display*. Japanese Journal of Applied Physics, 2004. **43**(6A): p. 3479-3483.
7. Eremin, A., et al., *Microscopic structures of the B7 phase: AFM and electron microscopy studies*. Liquid Crystals, 2006. **33**(7): p. 789-794.
8. Cordoyiannis, G., et al., *Effects of magnetic nanoparticles with different surface coating on the phase transitions of octylcyanobiphenyl liquid crystal*. Physical Review E, 2009. **79**(1): p. 011702.
9. Sharma, D., J.C. MacDonald, and G.S. Iannacchione, *Thermodynamics of Activated Phase Transitions of 8CB: A DSC and MC Calorimetry*. The Journal of Physical Chemistry B, 2006. **110**(33): p. 16679-16684.
10. Manohar, R., et al., *Dielectric and electro-optical study of ZnO nano rods doped ferroelectric liquid crystals*. Journal of Materials Science, 2011. **46**(18): p. 5969-5976.
11. Martínez-Miranda, L.J., et al., *Effect of Magnetic Nanoparticles and Their Functionalization on Liquid Crystal Order*. Molecular Crystals and Liquid Crystals, 2005. **435**(1): p. 87/[747]-93/[753].
12. Martinez-Miranda, L.J. and L.K. Kurihara, *Interaction and response of a smectic-A liquid crystal to a nanometer particle: Phase transition due to the combined effect of the functionalization compound and particle size*. Journal of Applied Physics, 2009. **105**(8): p. 084305-7.
13. Neeraj, P. Kumar, and K.K. Raina, *Changes in the electro-optical behaviour of ferroelectric liquid crystal mixture via silica nanoparticles doping*. Optical Materials, 2012. **34**(11): p. 1878-1884.
14. Neeraj, P. Kumar, and K.K. Raina, *Analysis of Dielectric and Electro-optic Responses of Nanomaterials Doped Ferroelectric Liquid Crystal Mixture*. Journal of Materials Science & Technology, 2011. **27**(12): p. 1094-1098.
15. Kim, Y.-T., et al., *Pixel-encapsulated flexible displays with a multifunctional elastomer substrate for self-aligning liquid crystals*. Applied Physics Letters, 2006. **88**(26): p. 263501.

16. Berreman, D., *Solid Surface Shape and the Alignment of an Adjacent Nematic Liquid Crystal*. Physical Review Letters, 1972. **28**(26): p. 1683-1686.
17. Stohr, J. and M.G. Samant, *Liquid crystal alignment by rubbed polymer surfaces: a microscopic bond orientation model*. Journal of Electron Spectroscopy and Related Phenomena, 1999. **98–99**(0): p. 189-207.
18. Huang, C.-Y., et al., *Multidirectional rubbed liquid-crystal cells*. Journal of Applied Physics, 2002. **92**(12): p. 7231.
19. Janning, J.L., *Thin film surface orientation for liquid crystals*. Applied Physics Letters, 1972. **21**(4): p. 173.
20. Lim, Y.-W., C.-H. Kwak, and S.-D. Lee, *Anisotropic Nano-Imprinting Technique for Fabricating a Patterned Optical Film of a Liquid Crystalline Polymer*. Journal of Nanoscience and Nanotechnology, 2008. **8**(9): p. 4775-4778.
21. Jeong, H.S., et al., *Self assembled plate-like structures of single-walled carbon nanotubes by non-covalent hybridization with smectic liquid crystals*. Carbon, 2010. **48**(3): p. 774-780.
22. Wainwright, S.G., et al., *True liquid crystal templating of SBA-15 with reduced microporosity*. Microporous and Mesoporous Materials, 2013. **172**: p. 112-117.
23. Schmidt-Mende, L., et al., *Self-Organized Discotic Liquid Crystals for High-Efficiency Organic Photovoltaics*. Science, 2001. **293**(5532): p. 1119-1122.
24. Huynh, W.U., J.J. Dittmer, and A.P. Alivisatos, *Hybrid nanorod-polymer solar cells*. Science, 2002. **295**(5564): p. 2425-7.
25. Jeong, S., et al., *Effects of Nematic Liquid Crystal Additives on the Performance of Polymer Solar Cells*. Macromolecular Chemistry and Physics, 2010. **211**(23): p. 2474-2479.
26. O'Neill, M. and S.M. Kelly, *Ordered Materials for Organic Electronics and Photonics*. Advanced Materials, 2011. **23**(5): p. 566-584.
27. Goodby, J.W., *Liquid crystals and life*. Liquid Crystals, 1998. **24**(1): p. 25-38.
28. Pankhurst, Q.A., et al., *Applications of magnetic nanoparticles in biomedicine*. Journal of Physics D: Applied Physics, 2003. **36**: p. R167-181.
29. Balazs, A.C., T. Emrick, and T.P. Russell, *Nanoparticle polymer composites: where two small worlds meet*. Science, 2006. **314**(5802): p. 1107-10.
30. Soulé, E.R., et al., *Phase equilibrium and structure formation in gold nanoparticles—nematic liquid crystal composites: experiments and theory*. Soft Matter, 2012. **8**(10): p. 2860.
31. Qi, H., et al., *Miscibility and alignment effects of mixed monolayer cyanobiphenyl liquid-crystal-capped gold nanoparticles in nematic cyanobiphenyl liquid crystal hosts*. Chemphyschem, 2009. **10**(8): p. 1211-8.
32. Chakraborty, S. and R. Garcia, *Optical-ellipsometric study of the nematic-to-smectic transition in 8CB films adsorbed on silicon*. Physical Review E, 2010. **81**(3).
33. Ramazanoglu, M., et al., *High-resolution x-ray scattering study of the effect of quenched random disorder on the nematic–smectic-A transition*. Physical Review E, 2007. **75**(6).

34. Sigdel, K.P. and G.S. Iannacchione, *Calorimetric study of the nematic to smectic-A phase transition in octylcyanobiphenyl-hexane binary mixtures*. Physical Review E, 2010. **82**(5).
35. Belyaev, B.A., et al., *Dielectric properties of liquid crystals in polycapillary matrices*. Physics of the Solid State, 2010. **52**(6): p. 1315-1322.
36. Roiter, Y., et al., *Interaction of Nanoparticles with Lipid Membrane*. Nano Letters, 2008. **8**(3): p. 941-944.
37. Amiri, S. and H. Shokrollahi, *The role of cobalt ferrite magnetic nanoparticles in medical science*. Materials Science and Engineering: C, 2013. **33**(1): p. 1-8.
38. Grabinski, C., et al., *Effect of Gold Nanorod Surface Chemistry on Cellular Response*. ACS Nano, 2011. **5**(4): p. 2870-2879.
39. Khlebtsov, N.G. and L.A. Dykman, *Optical properties and biomedical applications of plasmonic nanoparticles*. Journal of Quantitative Spectroscopy and Radiative Transfer, 2010. **111**(1): p. 1-35.
40. Martinez-Miranda, L.J., et al., *Effect of the surface coating on the magnetic nanoparticle smectic-A liquid crystal interaction*. Applied Physics Letters, 2006. **89**(16): p. 161917-3.
41. Takei, S., et al., *Nanoparticle free polymer blends for light scattering films in liquid crystal displays*. Applied Physics Letters, 2012. **100**(26): p. 263108.
42. Poland, C.A., et al., *Carbon nanotubes introduced into the abdominal cavity of mice show asbestos-like pathogenicity in a pilot study*. Nat Nano, 2008. **3**(7): p. 423-428.
43. Ryman-Rasmussen, J.P., et al., *Inhaled carbon nanotubes reach the subpleural tissue in mice*. Nat Nano, 2009. **4**(11): p. 747-751.
44. Jing, B. and Y. Zhu, *Disruption of Supported Lipid Bilayers by Semihydrophobic Nanoparticles*. Journal of the American Chemical Society, 2011. **133**(28): p. 10983-10989.
45. Nel, A.E., et al., *Understanding biophysicochemical interactions at the nano-bio interface*. Nat Mater, 2009. **8**(7): p. 543-557.
46. Wan, J., et al., *Liquid crystal pretilt control by inhomogeneous surfaces*. Physical Review E, 2005. **72**(2).
47. Even, C., M. Imperor-Clerc, and P. Pieranski, *Exploring the facets of "soft crystals" using an Atomic Force Microscope*. Eur Phys J E Soft Matter, 2006. **20**(1): p. 89-98.
48. Hirofumi Yamada, K.N., *Imaging of Organic Molecules by Atomic Force Microscopy*. Japanese Journal of Applied Physics, 1993. **32**: p. 2958-2961.
49. Stephen Prilliman, V.C. *TappingMode - Atomic Force Microscope Manual*. 1997; Available from: <http://nanonet.rice.edu/manuals/afm.html>.
50. Taylor, J.W., L.K. Kurihara, and L.J. Martinez-Miranda, *Interaction of a bi-molecular liquid crystal film with functionalized nanoparticles*. Applied Physics Letters, 2012. **100**(17): p. 173115-3.
51. Ravnik, M. and S. Žumer, *Nematic braids: 2D entangled nematic liquid crystal colloids*. Soft Matter, 2009. **5**(22): p. 4520.

52. Bagheri, M. and S. Shateri, *Synthesis and characterization of novel liquid crystalline cholesteryl-modified hydroxypropyl cellulose derivatives*. Journal of Polymer Research, 2012. **19**(3).
53. Als-Nielsen, J. and D. McMorrow, *Elements of modern X-ray physics*. 2001, New York: Wiley.
54. Martínez-Miranda, L.J., et al., *Liquid crystal-ZnO nanoparticle photovoltaics: Role of nanoparticles in ordering the liquid crystal*. Applied Physics Letters, 2010. **97**(22): p. 223301-3.
55. Martínez-Miranda, L.J., O.C. Wilson, and A.R. Douglas, *Self-Alignment of Inorganic Biomimetic Liquid Crystals: Magnetic Field Effects*. Molecular Crystals and Liquid Crystals, 2004. **409**(1): p. 91-97.
56. Thoen, J., H. Marynissen, and W. Van Dael, *Temperature dependence of the enthalpy and the heat capacity of the liquid-crystal octylcyanobiphenyl (8CB)*. Physical Review A, 1982. **26**(5): p. 2886-2905.
57. Ruhaak, L.R., et al., *Glycan labeling strategies and their use in identification and quantification*. Analytical and Bioanalytical Chemistry, 2010. **397**(8): p. 3457-3481.
58. Ge, M.Y., et al., *Nanostructured ZnO: From monodisperse nanoparticles to nanorods*. Journal of Crystal Growth, 2007. **305**(1): p. 162-166.
59. Zamanpour, M., et al., *Large-scale synthesis of high moment FeCo nanoparticles using modified polyol synthesis*. Journal of Applied Physics, 2012. **111**(7): p. 07B528-3.
60. Gold, S.H., et al., *System for continuous production of nanophase materials using a microwave-driven polyol process*. Review of Scientific Instruments, 2007. **78**(2): p. 023901.
61. Popova, A.N., *Synthesis and Characterization of Iron-Cobalt Nanoparticles*. Journal of Physics: Conference Series, 2012. **345**: p. 012030.
62. Li, H., et al., *Aminosilane Micropatterns on Hydroxyl-Terminated Substrates: Fabrication and Applications*. Langmuir, 2009. **26**(8): p. 5603-5609.
63. Garcia, R., E. Subashi, and M. Fukuto, *Thin-Thick Coexistence Behavior of 8CB Liquid Crystalline Films on Silicon*. Physical Review Letters, 2008. **100**(19).
64. Seu, K.J., et al., *Effect of Surface Treatment on Diffusion and Domain Formation in Supported Lipid Bilayers*. Biophysical journal, 2007. **92**(7): p. 2445-2450.
65. Ewiss, M.A.Z., et al., *Wetting behaviour of 5CB and 8CB and their binary mixtures above the isotropic transition*. Liquid Crystals, 2004. **31**(4): p. 557-566.
66. Cluzeau, P., et al., *Formation of two-dimensional crystal-like structures from inclusions in smectic C films*. Journal of Experimental and Theoretical Physics Letters, 2002. **76**(6): p. 351-354.
67. Frank, F.C., *I. Liquid crystals. On the theory of liquid crystals*. Discussions of the Faraday Society, 1958. **25**: p. 19.
68. Michel, J.-P., et al., *Structure of Smectic Defect Cores: X-Ray Study of 8CB Liquid Crystal Ultrathin Films*. Physical Review Letters, 2006. **96**(2).

69. Hung, F.R., et al., *Anisotropic nanoparticles immersed in a nematic liquid crystal: Defect structures and potentials of mean force*. Physical Review E, 2006. **74**(1).
70. Muševič, I., et al., *Two-Dimensional Nematic Colloidal Crystals Self-Assembled by Topological Defects*. Science, 2006. **313**(5789): p. 954-958.
71. Jampani, V.S.R., et al., *Colloidal entanglement in highly twisted chiral nematic colloids: Twisted loops, Hopf links, and trefoil knots*. Physical Review E, 2011. **84**(3): p. 031703.
72. Nayek, P., et al., *Bias dependent dielectric relaxation dynamics of electrically tuned large-scale aligned zinc oxide nanorods in nematic liquid crystal host*. Applied Physics Letters, 2008. **93**(11): p. 112905-3.
73. Koevar, K. and I. Muevi, *AFM study of forces in and structures of nematic liquid crystal interfaces on silanated glass*. Liquid Crystals, 2001. **28**(4): p. 599-606.
74. Gunther, L., Y. Imry, and J. Lajzerowicz, *X-ray scattering in smectic-A liquid crystals*. Physical Review A, 1980. **22**(4): p. 1733-1740.
75. Deutsch, M., *Orientational order determination in liquid crystals by x-ray diffraction*. Physical Review A, 1991. **44**(12): p. 8264-8270.
76. Warren, *X-ray Diffraction*. 1992: Dover.
77. Drevensek Olenik, I., et al., *Structure and polarity of 8CB films evaporated onto solid substrates*. Eur Phys J E Soft Matter, 2003. **11**(2): p. 169-75.
78. Kumpf, C., *Structure determination of very small (1–5 nm) nano-particles*. Applied Physics A: Materials Science & Processing, 2006. **85**(4): p. 337-343.
79. Kurihara, L.K., G.M. Chow, and P.E. Schoen, *Nanocrystalline metallic powders and films produced by the polyol method*. Nanostructured Materials, 1995. **5**(6): p. 607-613.
80. Kurihara, L.K., G.M. Chow, and P.E. Schoen, *Nanostructured Metallic Powders and Films Via an Alcoholic Solvent Process*, U.S.P. Office, Editor 1998, The United States of America as represented by the Secretary of the Navy: United States.
81. Jones, N.J., et al., *Observations of oxidation mechanisms and kinetics in faceted FeCo magnetic nanoparticles*. Journal of Applied Physics, 2010. **107**(9): p. 09A304.
82. Alagiri, M., C. Muthamizhchelvan, and S. Ponnusamy, *Structural and magnetic properties of iron, cobalt and nickel nanoparticles*. Synthetic Metals, 2011. **161**(15-16): p. 1776-1780.
83. Collier, K.N., et al., *Controlled oxidation of FeCo magnetic nanoparticles to produce faceted FeCo/ferrite nanocomposites for rf heating applications*. Journal of Applied Physics, 2009. **105**(7): p. 07A328.
84. Carta, D., A. Corrias, and G. Navarra, *An X-ray absorption spectroscopy study of FeCo alloy nanoparticles embedded in ordered cubic mesoporous silica (SBA-16)*. Journal of Non-Crystalline Solids, 2011. **357**(14): p. 2611-2614.
85. Stamatoff, J., et al., *X-Ray Diffraction Intensities of a Smectic-A Liquid Crystal*. Physical Review Letters, 1980. **44**(23): p. 1509-1512.

86. Chahine, G., et al., *Collective molecular reorientation of a calamitic liquid crystal (12CB) confined in alumina nanochannels*. Physical Review E, 2010. **82**(1).
87. Azároff, L.V., *X-ray scattering by cybotactic nematic mesophases*. Proceedings of the National Academy of Sciences, 1980. **77**(3): p. 1252-1254.
88. Zadorozhnyi, V.I., et al., *Nematic director response in ferronematic cells*. EPL (Europhysics Letters), 2006. **73**(3): p. 408.
89. Efremov, A., J.C. Mauro, and S. Raghavan, *Macroscopic Model of Phospholipid Vesicle Spreading and Rupture*. Langmuir, 2004. **20**(14): p. 5724-5731.
90. Mackay, M.E., et al., *General strategies for nanoparticle dispersion*. Science, 2006. **311**(5768): p. 1740-3.